NOVEL APPROACHES TO PHOTOASSISTED DEPOSITION OF SEMICONDUCTORS AND NANOCOMPOSITE MATERIALS

by

SASHIKALA SOMASUNDARAM

Presented to the Faculty of the Graduate School of
The University of Texas at Arlington in Partial Fulfillment
of the Requirements
for the Degree of

DOCTOR OF PHILOSOPHY

THE UNIVERSITY OF TEXAS AT ARLINGTON

August 2006

ACKNOWLEDGEMENTS

It is with great pleasure that I express my sincere thanks to my research advisor Professor Krishnan Rajeshwar for his extraordinary guidance and encouragement throughout my research period.

I wish to extend my warm and sincere thanks to my committee members Professors Zoltan A. Schelly, Richard B. Timmons, Rasika Dias, Richard (Xiyun) Guan, and former committee member Professor Gary R. Kinsel for their helpful comments and advice.

I wish to give special thanks to Professor Norma Tacconi and Dr. C. R. Chenthamarakshan for their priceless help and discussions. Thanks also go to all members of our research group for their help and support.

I make use of this opportunity to convey my gratitude and appreciation to my dear husband Don Priyantha for his understanding and constant support throughout the course of this dissertation study.

Finally, financial support from the TPEG scholarship and Department of Chemistry, UT Arlington, facilitated this study and is gratefully acknowledged.

July 28, 2006

ABSTRACT

NOVEL APPROACHES TO PHOTOASSISTED DEPOSITION OF SEMICONDUCTORS AND NANOCOMPOSITE MATERIALS

Publication No. ______

Sashikala Somasundaram, Ph.D.

The University of Texas at Arlington, 2006

Supervising Professor: Krishnan Rajeshwar

This dissertation research begins with the use of TiO_2-based photocatalysis for the reduction of metal ions with very negative reduction potentials. The indirect photocatalytic reduction of four metal ions: Cd^{2+}, Zn^{2+}, Mn^{2+}, and Tl^{+} using formate radical anions generated in UV-irradiated aqueous TiO_2 suspensions, is described. Using Tl^{+} as a model metal ion, a simple kinetics scheme was developed for the indirect reduction route, and the predictions from this model were shown to be in excellent agreement with experimental data. Titania-based photocatalysis was then used for the preparation of MSe/TiO_2 "coupled" semiconductors. Heterogeneous photocatalysis using photoexcited TiO_2 substrates was shown to be a versatile method for preparing Se- or metal selenide (MSe)- modified TiO_2 surfaces. The mechanistic aspects underlying this novel preparative route were addressed using chronopotentiometry and linear sweep photovoltammetry. Ex situ characterization of the prepared composite semiconductor samples was also carried out.

The cathodic electrosynthesis of WO_3-TiO_2 nanocomposites or layered films is then described. This part of the dissertation describes the preparation of WO_3-TiO_2 nanocomposite films by occlusion electrosynthesis and pulsed electrodeposition. These methods are shown to afford semiconductor composites with better photoresponse than its individual members.

The final part of the dissertation describes visible light-driven hydrogen production from water using electrodeposited p-type Cu_2O films. This study resolves the controversy which existed on the ability of p-Cu_2O to sustain the photoassisted splitting of water into H_2 and O_2. While p-Cu_2O is shown to be incapable of splitting water, the present study shows that H_2 can be generated by substituting water with an organic compound (e.g., hydroquinone) as a sacrificial electron donor. The implications of this study for constructing practical systems for solar-assisted production of H_2 from water are finally discussed.

TABLE OF CONTENTS

ACKNOWLEDGEMENTS ii

ABSTRACT iii

LIST OF FIGURESS vii

LIST OF TABLES xii

Chapter

1. INTRODUCTION AND BACKGROUND 1

  1.1 Photoassisted Deposition 1

  1.2 PAD of Metal Ions with Very Negative Standard Reduction Potentials 4

  1.3 Solid-State physics Aspects of Semiconductors 6

  1.4 The Basic Principles of Semiconductor-Based Heterogeneous Photocatalysis 16

  1.5 Oxide Semiconductors Considered in this Dissertation Work 19

  1.6 Nanocomposite or Layered Oxide Semiconductor Films 27

  1.7 Photoelectrochemical Hydrogen Production 30

2. EXPERIMENTAL 39

  2.1 Chemicals and Materials 39

  2.2 Instrumentation 40

  2.3 Procedures 41

3. RESULTS AND DISCUSSION 54

3.1 PAD of Metal Ions with Very Negative Standard Reduction Potentials 54

3.2 PAD of Calcoginide Semiconductors on TiO_2 68

3.3 Occlusion Electrosynthesis of WO_3-TiO_2 Composite Films 86

3.4 Pulsed Electrodeposition of WO_3-TiO_2 Composite Films....................... 102

3.5 Visible Light-Driven Hydrogen Production Using p-Cu_2O Photocathode 110

4. SUMMARY AND CONCLUDING REMARKS 121

REFERENCES 124

BIOGRAPHICAL INFORMATION 136

LIST OF FIGURES

Figure Page

1.1 Relative disposition of the energy levels in TiO_2 and solution species. A pH of 7 was assumed for this interfacial situation 3

1.2 Schematic diagram of the energy levels of an intrinsic semiconductor 7

1.3 Schematic diagram of the energy levels of (a) n-type semiconductor (b) p-type semiconductor 8

1.4 Band-bending for (a) n-type and (b) p-type semiconductor in equilibrium with an electrolyte 10

1.5 Effect of varying the applied potential (E) on the band edges in the interior of an n-type semiconductor. (a) E more (+) ve than V_{fb} (b) E = V_{fb} (c) E more (-) ve than V_{fb} 12

1.6 Effect of varying the applied potential (E) on the band edges in the interior of a p-type semiconductor. (a) E more (+) ve than V_{fb} (b) E = V_{fb} (c) E more (-) ve than V_{fb} 12

1.7 Ideal behavior for an n-type semiconductor (a) in the dark and (b) under irradiation 14

1.8 Schematic diagram of the heterogeneous photocatalytic process occurring on an illuminated semiconductor particle 17

1.9 Crystal structure of TiO_2 : (a) anatase (b) rutile and (c) brookite 21

1.10 Unit cell of WO_3 22

1.11 Unit cell of Cu_2O 23

1.12 Schematic diagram of standard single-compartment three-electrode electrochemical cell used for electrodeposition in this study 26

1.13 Schematic diagram showing vectorial charge transfer between TiO_2 and WO_3 components in the composite......28

1.14 Schematic diagrams of various configurations of semiconductor based photocatalytic H_2 generation...... 32

1.15 Schematic diagrams of various configurations of PEC cells for H_2 generation...... 32

1.16 (a) Relative positions of the energy levels of valance and conduction bands of selected semiconductors with respect to H^+/H_2 and OH^-/O_2 levels at pH 0 (b) Solar spectrum 34

1.17 Energy bands in a metal and a semiconductor...... 37

1.18 Work functions of Pt and Ni and positions of the valance and conduction bands of Cu_2O with respect to standard hydrogen electrode (SHE) 37

2.1 Schematic diagram of the UV photoreactor 42

2.2 Pulsed deposition potential waveform for the formation of WO_3-TiO_2 composite films (a) WO_3-TiO_2(A) and (b) WO_3-TiO_2(B). Pulse potentials are -0.45 and -0.95 V...... 48

2.3 Schematic diagram of the cell set-up used to measure the photocurrent...... 51

2.4 Instrumentation set-up used to monitor the formation of $MV^{\cdot+}$. A diode-array spectrometer is shown for the spectroelectrochemical measurements 52

2.5 Instrumentation set-up used to measure transient photocurrents in the p-Cu_2O-based photoelectrochemical cell for H_2 generation......53

3.1 Dependence of the initial rate of metal ion photoreduction in the formate additive concentration in UV-irradiated TiO_2 suspensions......55

3.2 Test of the model prediction for three initial concentration of Thallium (I) where the formate concentration was varied 63

3.3 As in Figure 3.2, but for the set of experiments where Thallium (I) concentration was varied while holding the formate concentration at three values shown 64

3.4 Relative disposition of the conduction and valence band-edges in TiO_2 and the redox energy levels for relevant species of interest to this study in an aqueous medium. Note the discontinuity in the potential scale at ~1.6 V (vs. SHE) 69

3.5 (a) Photocatalytic reduction of 200 μM Pb(II) in N_2-purged TiO_2 suspensions (2 g/L TiO_2 dose) under UV irradiation. (b) As in frame (a) but for the photocatalytic reduction of 200 μM Cd(II) species 71

3.6 Chronopotentiometric (CP) profiles for a UV-irradiated TiO_2 film electrode in contact with 0.05 M Na_2SO_4 supporting electrolyte with and without added Se(IV) (at 200 μM level) species 74

3.7 CP profiles for experiments involving Cd(II) species 76

3.8 As in Figure 3.7 but for Pb(II) species. The supporting electrolyte was 0.05 M NaCl instead of 0.05 M Na_2SO_4 78

3.9 Linear sweep photovoltammograms in 0.5 M Na_2SO_4 for (a) Se-modified TiO_2 film and (b) CdSe- and Se- modified TiO_2 film 80

3.10 Photovoltammogram for an electrodeposited Se^0 film in 0.5 M H_2SO_4. The Se film was grown on a gold surface by polarizing for 15 min at -0.7 V (vs. Ag|AgCl) in a solution containing 10 mM SeO_2 in 0.1 M Na_2SO_4 81

3.11 Representative EPMA elemental map for a sample as in Figures 3.9b and 3.10 (Courtesy : Prof. R. Shiratsuchi, Kyushu Institute of Technology Japan 84

3.12 Survey XPS scan for a sample as in Figure 3.9b 85

3.13 Effect of TiO_2 particle dose in the deposition bath on the current–time profiles 87

3.14 3-D plot of the WO_3 deposition charge as a function of time for TiO_2 particle doses varying between 0.32 and 3.2 mg/mL 88

3.15 (A) Raman spectra of P 25 TiO_2 particles after being subjected to pre-calcination at 450 ^{0}C (a), 600 ^{0}C (b), 650 ^{0}C (c), 700 ^{0}C (d), and 800 ^{0}C (e). (B) Temperature dependence of the % composition (anatase and rutile) (Courtesy: Prof. Norma R. de Tacconi, University of Texas at Arlington 90

3.16 Effect of the occluded TiO_2 particles on the photoelectrochemical behavior of a WO_3 film, (a) without, and (b) with 11% of P 25 TiO_2 (pre-calcined at 450 °C)..92

3.17 Photoaction spectra of WO_3-TiO_2 composite films containing particles pre-calcined at 450 °C and 800 °C. Electrolyte: 0.5 M Na_2SO_4 + 0.1 M HCOONa. The photoaction spectrum for a WO_3 matrix without TiO_2 particles is also included for comparison..93

3.18 Photovoltammograms for WO_3-TiO_2 composite films with the TiO_2 particles pre-calcined at 450 °C ((a) and (b)) and at 800 °C ((c) and (d)) in 0.5 M Na_2SO_4 ((a) and (c)) and in 0.5 M Na_2SO_4 + 0.1 M HCOONa ((b) and (d))..94

3.19 Photocurrent 3-D plots as a function of film preparation variables: WO_3 electrodeposition charge and TiO_2 particle dose. 99

3.20 Scanning electron micrograph of (a) WO_3-TiO_2 (A) and (b) WO_3-TiO_2 (B) composite film samples. The small grains are TiO_2 decorating the much larger WO_3 grains.. 103

3.21 Side perspectives of (a) WO_3-TiO_2 (A) and (b) WO_3-TiO_2 (B) composite film samples obtained from tilting the SEM sample stage by 20^0 104

3.22 Survey XPS scan for a sample of (a) WO_3-TiO_2 (A) (b) WO_3-TiO_2 (B) 106

3.23 Photocurrent-potential profiles with chopped irradiation in (a) 0.5 M Na_2SO_4 and (b) 0.5 M Na_2SO_4 + 0.1 M HCOONa for (A) electrodeposited WO_3, (B) composite WO_3-TiO_2 (A) and (C) composite WO_3-TiO_2 (B) films respectively. 107

3.24 (a) Histogram plots of photocurrent densities of WO_3 and WO_3-TiO_2 composite films taken from the photovoltammograms in Figure 4 at a fixed potential of 0.8 V. (b) Comparison of photoaction spectra of WO_3 and WO_3-TiO_2 composite films in 0.5 M Na_2SO_4. Spectra acquired at a bias potential of 0.8 V 108

3.25 Cyclic voltammograms of various electron donor candidates........................111

3.26 UV-Visible spectrum of TCO/Cu_2O electrode, and 0.01 M $NiSO_4$ solution..113

3.27 Survey XPS scan for a sample of (a) TCO/p-Cu_2O (b) TCO/p-Cu_2O/Ni.....114

3.28 Comparison of short circuit photocurrent of PEC cell containing (a) various sacrificial electron donors in the anode compartment with bare p-Cu_2O photoelectrode and p-Cu_2O photoelectrode surface modified with Ni/NiO (b) with and without MV^{2+} in the cathode compartment.....116

3.29 (a) Evolution of $MV^{\cdot +}$ (λ_{max}= 605 nm) by irradiation of p-Cu_2O film in 0.5 M Na_2SO_4 containing 40 mM MV^{2+} (b) Variation of absorbance at 605 nm vs. irradiation time.....117

3.31 Transient photocurrent of p-Cu_2O photoelectrochemical cell for a 0.5 M Na_2SO_4 solution containing 40 mM MV^{2+} at applied potential of -0.30 V.....118

3.32 Phocurrent dependence on stirring rate.....119

3.33 Comparison of short circuit photocurrent of PEC cell with and without occluded Cu_2O nanopartcles.....120

LIST OF TABLES

Table Page

1.1 Comparison of the properties of different polymorphs of titanium dioxide.. 20

1.2 Crystallographic properties of cuprous oxide (Cu_2O) 24

3.1 Rate constants[a] for the homogeneous and heterogeneous reactions between metal ions and formate radicals 57

3.2 Amount of metal ion adsorbed on the TiO_2 surface with and without formate ions present..58

3.3 Values of k'k" (equation 3.10) from the slopes of the plots in Figures 3.2 and 3.3..65

3.4 Comparison of IPCE values and photocurrent enhancement factors (F) for various samples 97

3.5 Oxidation potentials of various electron donors determined by cyclic voltammetry 112

CHAPTER 1

INTRODUCTION AND BACKGROUND

1.1 Photoassisted Deposition

Photoassisted deposition (PAD) involves the optical excitation of a semiconductor substrate. The photogenerated carriers (electrons or holes) then serve to reductively (or oxidatively) deposit a targeted film on the substrate surface. In an early implementation of this interesting concept, optical excitation of aqueous TiO_2 slurries was used to modify the oxide surface with noble metal (e.g., Pt) catalyst islands.[1] In this instance, the photogenerated electrons in TiO_2 served to reduce the dissolved noble metal complexes to their elemental state on the oxide surface.

Polymeric films have been deposited on semiconductor surfaces using PAD.[2-6] Thus photopolymerization of both styrene and methylmethacrylate monomer was noted on TiO_2 when light was focused on the oxide semiconductor.[2] Polypyrrole was deposited on ZnO by PAD[3] and on aqueous dispersions of TiO_2 powder.[4,5] Light-localized deposition of polypyrrole and polythiophene was reported on n-Si wafers.[6] These modified photocatalysts were deployed for hydrogen generation.[5] In most of these cases, a reducing agent (e.g., acetate) was used in the aqueous medium contacting the oxide surface, to scavenge the photogenerated holes. Such processes can also be exploited for the photoassisted deposition of targeted chalcogenide semiconductors on the oxide surface as will be demonstrated in this dissertation work.

There is however, another potential route to securing the PAD of such metals by the use of organic free-radicals that are initially photogenerated on the TiO_2 surface.[7-10] Such radicals, especially those derived from carboxylate anions such as formate or acetate, have sufficient reducing power even for metal ions with rather negative standard reduction potentials such as Zn^{2+} or Mn^{2+} (Figure 1.1).[10] The mechanistic details of this indirect PAD route will be discussed as a part of this dissertation work.

1.1.1 *PAD of Chalcogenide Semiconductors on TiO_2*

Our group has pioneered the PAD of MSe semiconductors on TiO_2 by first depositing a Se chemical template on the oxide surface.[11] Subsequent irradiation of the Se-modified TiO_2 surface in a M^{n+} ion containing medium results in underpotential deposition of the metal to form MSe in situ on the oxide surface. This finding opens a new route to the preparation of MSe/TiO_2 "coupled" semiconductor configurations.[12] The interesting aspect is that the PAD of metal ions such as Cd^{2+} (or Zn^{2+}) would not have otherwise occurred on the TiO_2 surface, in the absence of the Se template.[11] This is because of the unfavorable location of the redox potentials, corresponding to the $M^{n+} \rightarrow M^0$ reaction for such metal ions, relative to the TiO_2 conduction band edge (Figure 1.1).

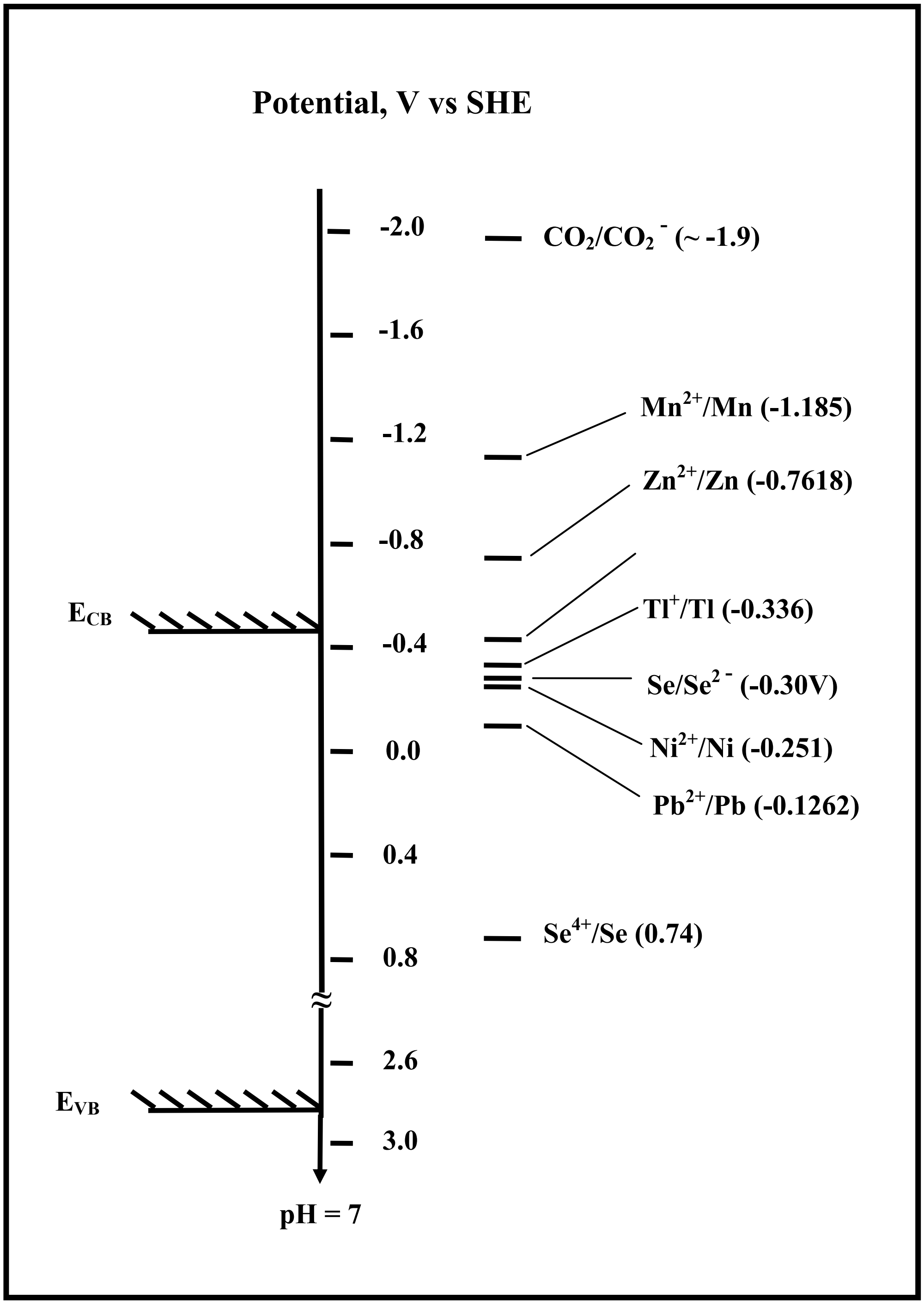

Figure 1.1: Relative disposition of the energy levels in TiO_2 and solution species A solution pH of 7 was assumed for this interfacial situation.

1.2 PAD of Metal Ions with Very Negative Standard Reduction Potentials

Environmental problems faced by the advanced industrialized nations are related to the remediation of hazardous wastes, contaminated groundwater and surface water, and the control of toxic air contaminants. Semiconductor photocatalysis appears to be a promising technology that has a number of applications in the environmental remeriation field such as air purification, water disinfection, hazardous waste remediation and water purification.[13] Photocatalytic processes on the TiO_2 surface have been widely deployed for the mineralization of organic pollutants[14-16] and for the immobilization of toxic metal ions in water.[14,17] TiO_2 is a most useful material for photocatalytic purposes owing to its exceptional optical and electronic properties, chemical stability, non-toxicity and low cost.

Heterogeneous photocatalysis using UV-irradiated titanium dioxide suspensions or films in aqueous media, is now a mature field. [14-16, 18-20] The photocatalytic reduction of metal ions in such media has both fundamental and practical interest. [14-20] While metal ions with rather positive standard reduction potentials [i.e., positive of 0 V versus the standard hydrogen electrode reference (SHE), see Ref. 21] such as Cu^{2+}, Cr^{6+}, Au^{3+}, Ag^{+} etc. have been widely investigated, only few studies exist on metal ions that are much more difficult to be reduced, for example: Cd^{2+}, Zn^{2+}, Mn^{2+}, Tl^{+}.[21] These metal ions can be reduced indirectly by the use of organic free radicals that are initially photogenerated on the TiO_2 surface.[7-10]

Initial photoexcitation of TiO_2 creates electron-hole pairs, some of which escape recombination and diffuse to the oxide/water interface. [15,18] There they encounter electron acceptors (e.g., H^+, O_2) or electron donors (formate ions, OH^-, water molecules). The photooxidation of formate (either directly by the photogenerated holes or via the intermediacy of $OH^\cdot$) generates the formate radical anion, $CO_2^{\bullet -}$. While this species is well known to be strongly and quantitatively reducing toward a variety of organic and inorganic compounds, there is some uncertainty in the value for the standard reduction potential of $CO_2^{\bullet -}$ on the SHE scale.[22] Taking a value of –1.90 V,[23] however, Figure 1.1 shows that $CO_2^{\bullet -}$ is thermodynamically capable of reducing all four metal ions considered in this study, namely Cd^{2+}, Zn^{2+}, Mn^{2+}, and Tl^+. On the other hand, the direct reduction of Mn(II) and Zn(II) by the electrons photogenerated in TiO_2, is thermodynamically prohibited (Figure 1.1). [We assume for this discussion that we are only dealing with thermalized (i.e., not "hot") electrons at the oxide/water interface]. By the same token, the direct photocatalytic reduction of Cd(II) and Tl(I) has only a modest driving force (Figure 1.1).

As mentioned earlier, only few studies exist on the indirect photocatalytic reduction of metal ions using free radicals generated on oxide semiconductor surfaces under UV illumination. Free radicals derived from formate or ethanol were shown to enhance the photoreduction of p-nitrosodimethylaniline in UV-irradiated ZnO aqueous suspensions.[7] Photodeposition of Pt, Ag, and Au was performed on a positively biased TiO_2 electrode in an aqueous solution containing radical intermediates derived from alcohols.[8] Nickel(II) was photoreduced by $CO_2^{\bullet -}$ generated from the initial photooxidation of oxalate ions in UV-irradiated TiO_2 suspensions.[9] In our own laboratory, the free radical-mediated indirect photocatalytic reduction route has been demonstrated for a variety of species: Ni(II),[10a] Pb(II),[10b] As(V),[10c] Zn(II),[8,10d,10e] Cd(II),[8,10d,10e] Mn(II),[8,10f] and Tl(I)[8,10g] in UV-irradiated TiO_2 suspensions.

Since this dissertation work involves various inorganic semiconductors, some basic theoretical aspects of semiconductors are reviewed next.

1.3 Solid-State Physics Aspects of Semiconductors

1.3.1 Energy Bands of Solids[24]

The solid is an array of atoms with each atom having different electronic energy states. When these atoms come closer to form the solid, these energy states overlap resulting in energy *bands*.[24] The electrons previously accommodated in the electronic energy levels are now accommodated in energy bands. The energy band containing bonding (valence) electrons is termed the valence band. The band next higher in energy to the valence band is termed the conduction band. The energy difference (E_g) between the valence band and the conduction band determines whether the solid is a conductor, semiconductor or an insulator. When the conduction and valence bands of a conductor overlap or lie closer, valence electrons can easily get excited into the conduction band. This will give a flow of mobile electrons (under an electric field) resulting in good electrical conductivity. An insulator has large band gap energy. Therefore the electrons in the valence band cannot easily get excited into the conduction band. Having no mobile electrons, an insulator does not exhibit electrical (i.e., electronic) conductivity under normal conditions.

The energy difference between the valence and the conduction bands in a semiconductor is in between those in a conductor and an insulator. Although $E_g > kT$ for most semiconductors at ordinary temperatures, there are still some thermally excited carriers in the conduction band which give conduction, i.e., for semiconductors, if the band gap is not so large, electrons can move into the conduction band. The promotion of electrons leaves a positively charged vacancy in the valence band which is referred to as a hole. These holes can be moved through space by the transfer of an electron to the vacancy, and therefore holes are considered to be mobile and opposite in polarity to electrons. Electrons can be excited to the conduction band either thermally or photochemically. However there is another method for generating charge carriers (i.e., electrons or holes) within a semiconductor, referred to as doping. Doping involves the addition of a different element into the semiconductor. Undoped semiconductors are referred to as intrinsic semiconductors (Figure 1.2).

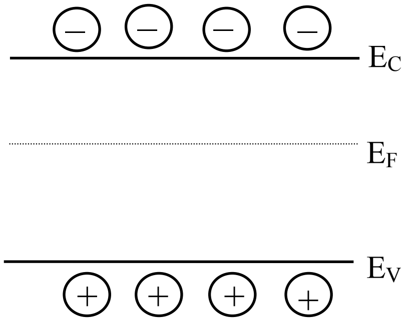

Figure 1.2: Schematic diagram of the energy levels of an intrinsic semiconductor.

Doped semiconductors in which the dominant charge carriers are electrons are referred to as n-type semiconductors, whereas those in which holes are majority charge carriers are referred to as p-type semiconductors (Figure 1.3).

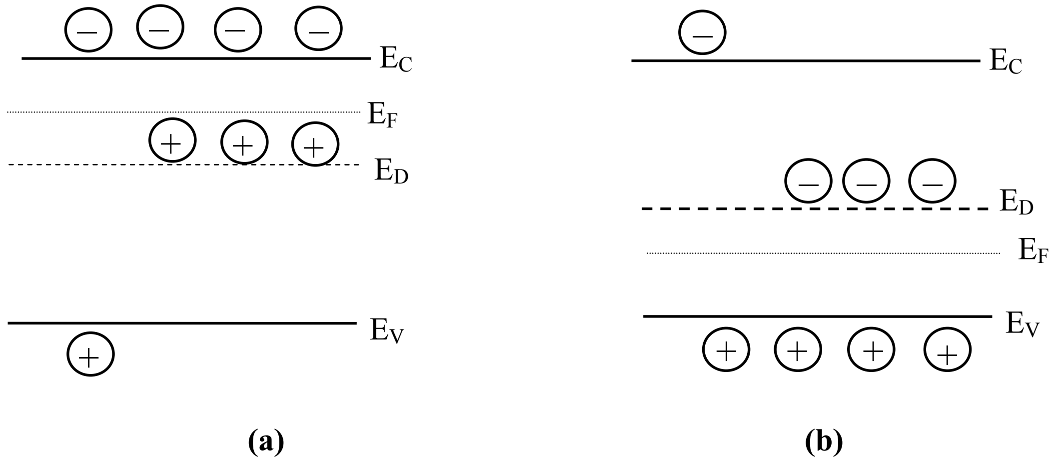

Figure 1.3: Schematic diagram of the energy levels of (a) n-type semiconductor (b) p-type semiconductor. E_F is the so-called Fermi level.

Another important concept in discussion of solid state materials is the Fermi level, E_F. This is defined as the energy level at which the probability of occupation by an electron is 0.5(at 0 K); for example, for an intrisic semiconductor the Fermi level lies approximately at the mid point of the band gap (Figure 1.2). Doping changes the distribution of electrons within the solid, and hence changes the Fermi level. For an n-type semiconductor the Fermi level lies just below the conduction band, whereas for a p-type semiconductor it lies just above the valence band (Figure 1.3). In addition, as with metal electrodes, the Fermi level of a semiconductoelectrode varies with the applied potential; for example a negative bias potential will “raise” the Fermi level.

1.3.2 Semiconductor/Electrolyte Interface[25, 27]

Now let us consider the (idealized) interface between a semiconductor electrode and an electrolyte solution. In order for the two phases to be in equilibrium, their electrochemical potential must be the same. The electrochemical potential of the solution is determined by the redox potential of the electrolyte solution, and the redox potential of the semiconductor is determined by the Fermi level. If the redox potential of the solution and the Fermi level do not lie at the same energy, a transfer of charge between the semiconductor and the solution is required to equilibriate the two phases. The excess charge that is now located on the semiconductor does not lie at the surface as it would for a metallic electrode, but extends into the electrode for a significant distance (100-1000 Å). This region is referred to as the space-charge region, and has an associated electric field. Hence, there are two "double layers" to consider: the interfacial (electrode / electrolyte) double layer, and the space-charge layer within the semiconductor electrode. Note that a metal electrode cannot sustain an appreciable space-charge layer within it because of its high electrical conductivity.

For an n-type semiconductor electrode at open circuit, the Fermi level is typically higher than the redox potential of the electrolyte and hence electrons will be transferred from the electrode into the solution. Therefore there is a positive charge associated with the space-charge region, and this is reflected in an upward bending of the band edges (Figure 1.4(a)). Since the majority charge carriers of the semiconductor have been removed from this region, this region is also referred to as a depletion layer. For a p-type semiconductor, the Fermi level is generally lower than the redox potential, and hence electrons must transfer from the solution to the electrode to attain equilibrium. This generates a negative charge in the space-charge region, which causes a downward bending of the band edges (Figure 1.4(b)). Since the holes in the space-charge region are removed by this process, this region is again a depletion layer.

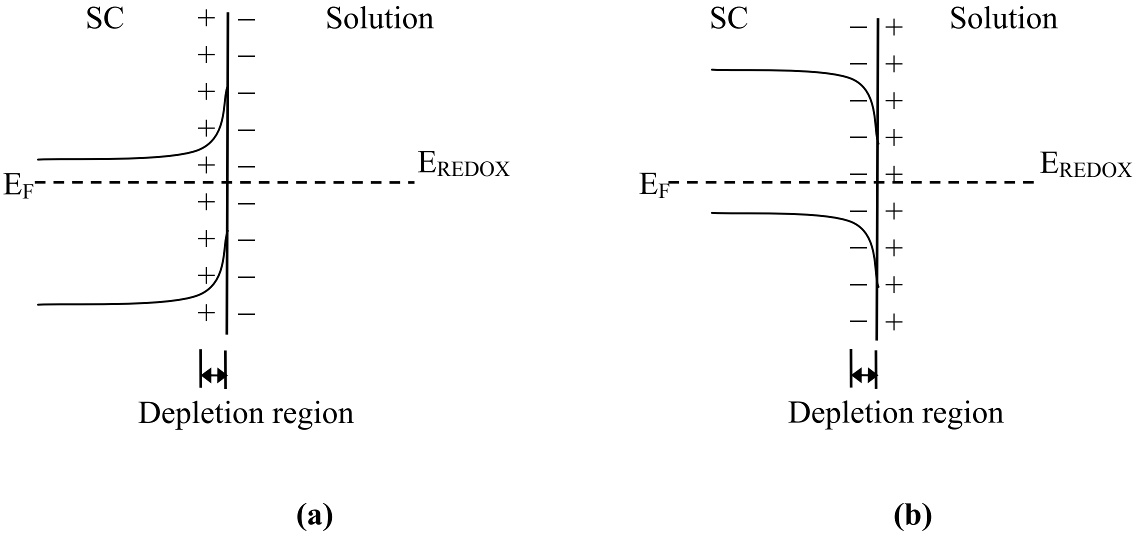

Figure 1.4: Band-bending for (a) n-type and (b) p-type semiconductor in equilibrium with an electrolyte.

As for metallic electrodes, changing the applied (bias) potential to the electrode shifts the Fermi level. The band edges in the interior of the semiconductor (i.e., away from the depletion region) also vary with the applied potential in the same way as the Fermi level. However, the energies of the band edges at the interface are not affected by changes in the applied potential. Therefore, the change in the energies of the band edges on going from the interior of the semiconductor to the interface, and hence the magnitude and direction of band bending, varies with the applied potential. There are three different situations to be considered.

(a) At a certain potential, the Fermi energy lies at the same energy as the solution redox potential (Figures 1.5(b), 1.6(b)). There is no net transfer of charge, and hence there is no band bending. This potential is therefore referred to as the flat-band potential (V_{fb}).

(b) Depletion regions arise at potentials positive of the flat-band potential for an n-type semiconductor and at potentials negative of the flat-band potential for a p-type semiconductor (Figures 1.5(a), 1.6(c)).

(c) At potentials negative of the flat-band potential for an n-type semiconductor, there is now an excess of the majority charge carriers (electrons) in this space charge region, which is referred to as an accumulation region (Figure 1.5(c)). An accumulation region arises in a p-type semiconductor at potentials more positive than the flat band potential (Figure 1.6(a)).

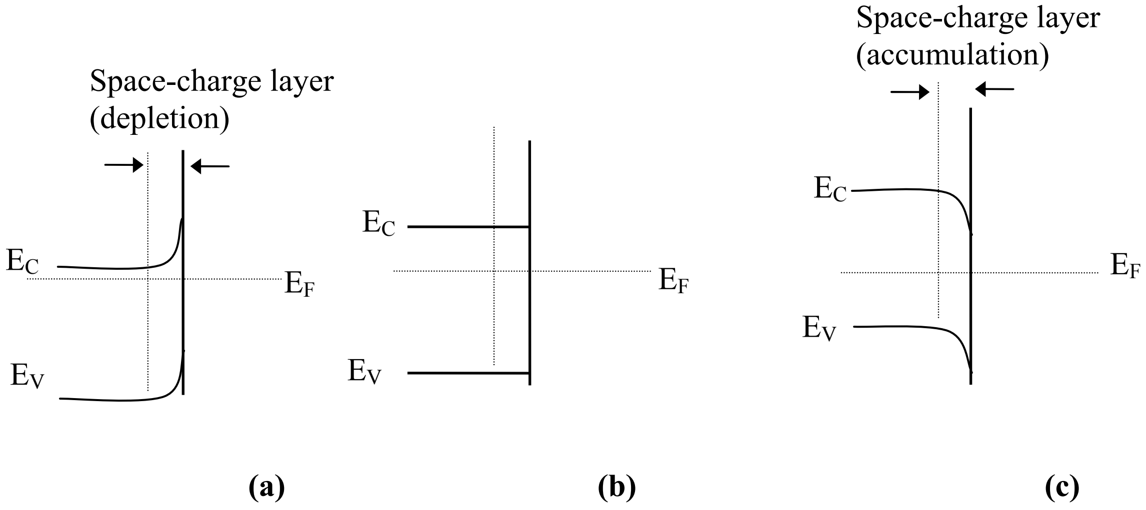

Figure 1.5: Effect of varying the applied bias potential (E) on the band bending at a n-type semiconductor/electrolyte interface: (a) E more (+) ve than V_{fb} (b) E = V_{fb} (c) E more (-) ve than V_{fb}.

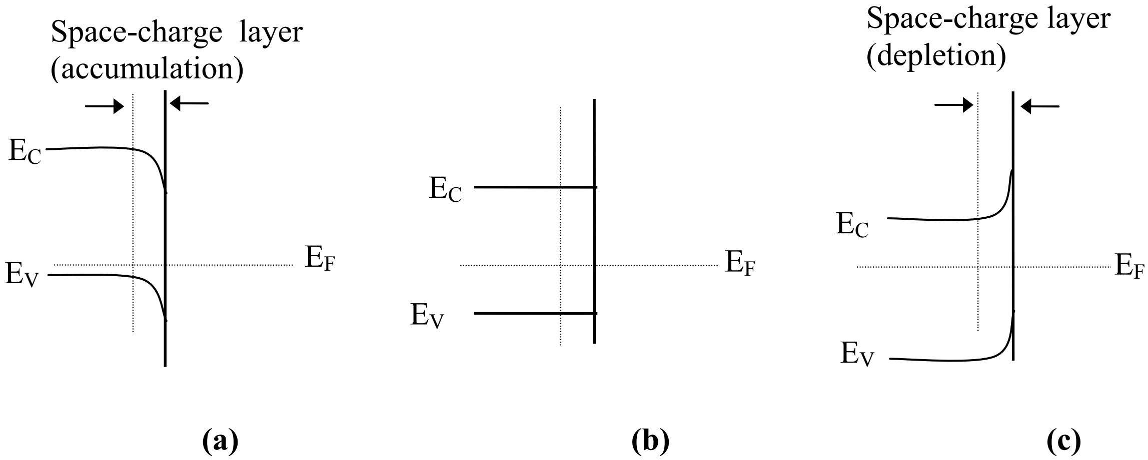

Figure 1.6: Effect of varying the applied potential (E) on the band bending at a p-type semiconductor/electrolyte interface: (a) E more (+) ve than V_{fb} (b) E = V_{fb} (c) E more (-) ve than V_{fb}.

The charge transfer ability of a semiconductor electrode depends on whether there is an accumulation layer or a depletion layer. If there is an accumulation layer the behavior of a semiconductor electrode is akin to that of a metallic electrode, since there is an excess of majority carriers available for charge transfer. In contrast, if there is a depletion layer then there are few charge carriers available for charge transfer and electron transfer reactions do not occur, at least in the "dark".

However, if the semiconductor electrode is exposed to radiation of sufficient energy, electrons can now be promoted to the conduction band. If this process occurs in the interior of the semiconductor, recombination of the promoted electron and the resulting hole typically occurs with the production of heat. However, if it occurs in the space-charge region, the electric field in this region will cause the separation of the photogenerated charge. For example, for an n-type semiconductor at positive potentials, the band edges bend upwards, and hence the hole drifts to the interface and the electron moves to the interior of the semiconductor. The hole is a high energy species that can extract an electron from a solution species; i.e., the n-type semiconductor electrode acts as a photo-anode. Ideal behavior for an n-type semiconductor electrode in the dark and under irradiation is shown in Figure 1.7.

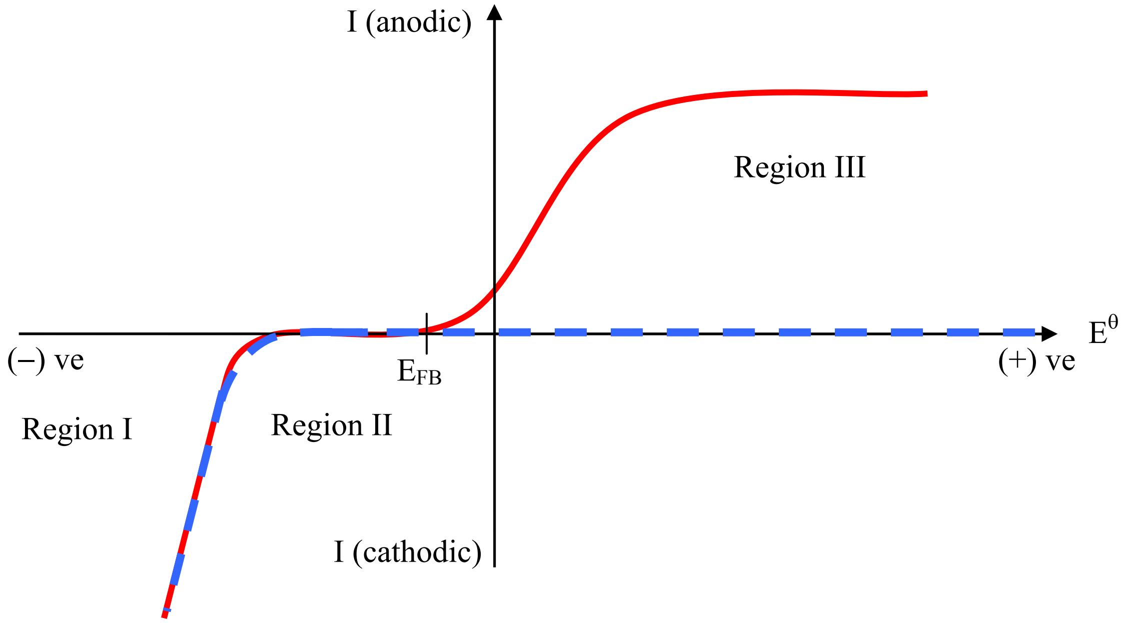

Figure 1.7: Ideal behavior for an n-type semiconductor (a) in the dark [– –] and (b) under irradiation [—].

At the flat-band potential there is no current, either in the dark or upon irradiation (Region II), since there is no electric field to separate any generated charge carriers. At potentials negative of the flat-band potential (Region I), an accumulation layer exists, and the electrode can act as a cathode, both in the dark and upon irradiation. At potentials positive of the flat-band potential (Region III), a depletion layer exists, so there can be no oxidative (anodic) current in the dark. However, upon irradiation a photocurrent can be observed at potentials negative of the redox potential of the analyte (which lies at E^{θ}). Using similar reasoning, it can be shown that p-type semiconductor electrodes are dark anodes and photo cathodes.

1.3.3 Determination of the Position of the Band Edges and the Flat-Band Potential

Now let us consider the techniques used to find the band edges of a semiconductor. This requires measurement of the flat-band potential. There are three techniques commonly used to measure the flat-band potential. These involve the measurement or acquisition of: (1) the open-circuit potential under intense illumination, (2) the onset of photocurrent, (3) Mott-Schottky plots (from capacity measurements).

Once the flat-band potential has been determined, the band position can be calculated using the following relationships:

For p-type

$$E_{VB} = -V_{fb} + kT \ln N_D / N_V \tag{1.1}$$

For n-type

$$E_{CB} = V_{fb} + kT \ln N_D / N_C \tag{1.2}$$

where V_{fb} is the flat-band potential, N_D is the doping level (in cm^{-3}), and N_C and N_V are the effective density of states (again with units of cm^{-3}) for the conduction band and valence band, respectively (taken from solid state measurements). The other band edge position (the conduction band for p-type and the valence band for n-type) may be found by using the value of the band gap energy.

1.3.4 Metal-Semiconductor Contacts[26]

Now let us consider the electrical characteristics of metal-semiconductor contacts. Two different types of contacts can be produced: Schottky contact, and ohmic contact. A Schottky contact is a rectifying contact between a metal and a semiconductor. The rectifying properties of the contact are similar to those of a PN junction diode. An ohmic contact is a non-rectifying contact. The current-voltage characteristics of the contact should obey Ohm's law (V = IR) and the resistance of the contact should be as low as possible. In practice a Schottky contact behaves as an ohmic contact if the impurity concentration (N_D) in the semiconductor is high enough (e.g., $N_D = 10^{20}$ cm^{-3}). This is because when the impurity concentration is increased, the width of the depletion region is decreased.[26] Then electrons can easily tunnel through the thin potential barrier, yielding a low-resistance ohmic contact between the metal and the semiconductor.

1.4 Basic Principles of Semiconductor-Based Heterogeneous Photocatalysis

The processes of heterogeneous photocatalysis that occur on an illuminated semiconductor particle can be summarized shortly as follows (Figure 1.8).[17] As mentioned earlier, a semiconductor is characterized by an electronic band structure in which the highest occupied energy band, called valence band (VB) and the lowest empty band called conduction band (CB) are separated by a band gap. When a photon of energy higher or equal to the band gap energy is absorbed by a semiconductor particle, an electron (e^-) from the VB is promoted to the CB creating a positive hole (h^+)

in the VB. This electron-hole pair formation is a key step in the photocatalytic process. The electron in the conduction band (e^-_{CB}) and the hole in the valance band (h^+_{VB}) can recombine on the surface or in the bulk of the particle by the emission of heat or can be trapped in surface states where they can react with donor (D) or acceptor (A) species adsorbed or close to the surface of the particle. Thus subsequent anodic and cathodic redox reactions can be initiated.

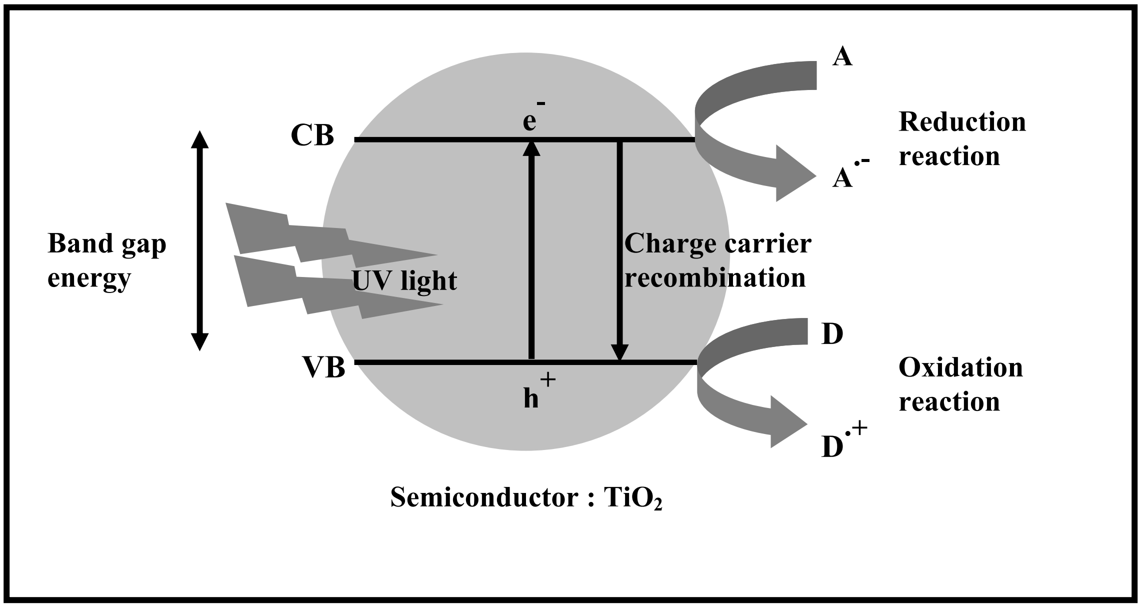

Figure 1.8: Schematic diagram of the heterogeneous photocatalytic process occurring on an illuminated semiconductor particle.

The energy level at the bottom of the CB is actually the reduction potential of photoelectrons and the energy level at the top of the VB determines the oxidizing ability of the photoholes. From the thermodynamic point of view, adsorbed redox species can be reduced photocatalytically by CB electrons if they have redox potentials more positive than the CB level of the semiconductor, and can be oxidized by VB holes if they have redox potentials more negative than the VB edge of the semiconductor.

1.4.1 Mechanism of TiO_2 Based Heterogeneous Photocatalysis[13]

1) Charge carrier generation:

$$TiO_2 + h\nu \longrightarrow h^+_{VB} + e^-_{CB} \qquad (1.3)$$

2) Charge carrier trapping:

$$h^+_{VB} + {>}Ti^{IV}OH \longrightarrow \{{>}Ti^{IV}OH^{\bullet}\}^+ \qquad (1.4)$$

$$e^-_{CB} + {>}Ti^{IV}OH \longrightarrow {>}Ti^{III}OH \qquad (1.5)$$

3) Charge carrier recombination:

$$h^+_{VB} + {>}Ti^{III}OH \longrightarrow {>}Ti^{IV}OH \qquad (1.6)$$

$$e^-_{CB} + \{{>}Ti^{IV}OH^{\bullet}\}^+ \longrightarrow {>}Ti^{IV}OH \qquad (1.7)$$

4) Interfacial charge transfer:

$$\{{>}Ti^{IV}OH^{\bullet}\}^+ + D \longrightarrow {>}Ti^{IV}OH + D^{\bullet +} \qquad (1.8)$$

$$\{{>}Ti^{III}OH\} + A \longrightarrow {>}Ti^{IV}OH + A^{\bullet -} \qquad (1.9)$$

${>}Ti^{IV}OH$ represents the primary hydrated surface functionality of TiO_2, $\{{>}Ti^{IV}OH^{\bullet}\}^+$ is the surface trapped valence band hole (i.e., surface bound hydroxyl radical) and $\{{>}Ti^{III}OH\}$ is the surface trapped conduction band electron.

Further mechanistic aspects of heterogeneous photocatalysis will be discussed later in this dissertation.

1.5 Oxide Semiconductors Considered in this Dissertation Work

1.5.1 Titanium Dioxide (TiO_2)

TiO_2 belongs to a family of transition metal oxides. It occurs in nature in three crystalline forms: anatase, rutile and brookite. Both rutile and anatase crystallize in the tetragonal system and brookite in the rhombic system. Crystallographic information on the three polymorphs of TiO_2 is summarized in Table 1.1 and the crystallographic structures are shown in Figure 1.9.

Anatase and rutile are the commonly occurring forms of TiO_2. At normal pressure, rutile is the thermodynamically stable form of TiO_2 at all temperatures; it is about 1.2 – 2.8 k.cal/mol more stable than anatase.[28] Anatase, the meta-stable polymorph, transforms rapidly to rutile at temperatures above 700 ^{0}C. The phase change from anatase to rutile has been reported to occur in different temperature ranges from 600 – 1000 ^{0}C depending on the crystallite size and impurity contents.[29] Both anatase and rutile are wide band gap semiconductors in which a filled valence band derived from the O 2p orbitals is separated from an empty conduction band derived from the Ti 3d orbitals. The energy band gaps of anatase and rutile are 3.2 eV and 3.0 eV respectively.

Table 1.1: Comparison of the properties of different polymorphs of titanium dioxide. (http://ruby.colorado.edu/~smyth/min/tio2.html)

	Rutile	**Anatase**	**Brookite**
Formula weight	79.890	79.890	79.890
Z	2	4	8
Crystal system	Tetragonal	Tetragonal	Orthorhombic
Point group	4/mmm	4/mmm	Mmm
Space group	P42/mmm	I41/amd	Pbca
Unit cell			
a(Å)	4.5845	3.7842	9.184
b(Å)	-	-	5.447
c(Å)	2.9533	9.5146	5.145
Volume	62.07	136.25	257.38
Molar volume	18.693	20.156	19.377
Density	4.2743	3.895	4.123

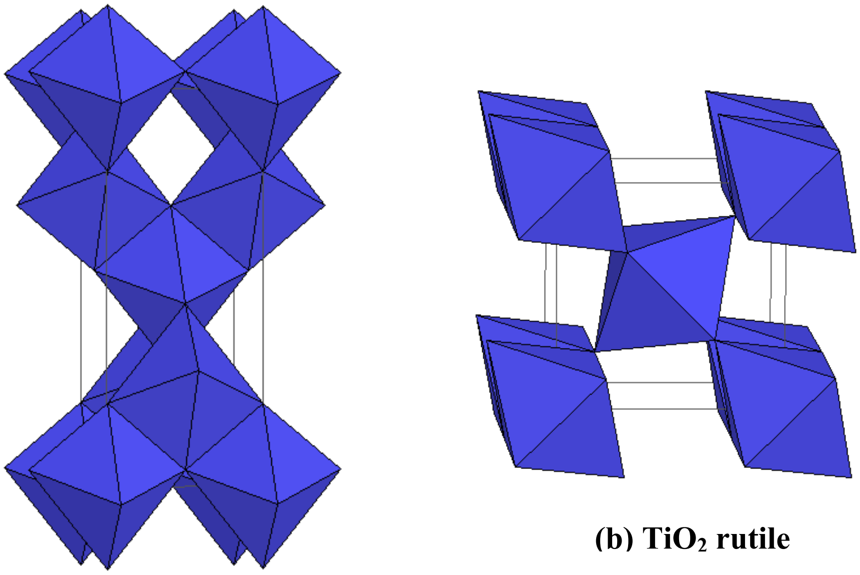

(b) TiO_2 rutile

(a) TiO_2 anatase

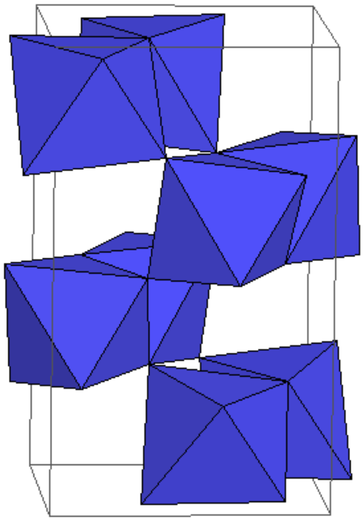

(c) TiO_2 brookite

Figure 1.9: Crystal structure of TiO_2 : (a) anatase (b) rutile and (c) brookite (http://ruby.colorado.edu/~smyth/min/tio2.html)

The anatase phase has a higher photocatalytic activity than the rutile counterpart. The photocatalytic activity is better because the crystal structure, size distribution, porosity, band gap, band edge position, surface defects, surface hydroxyl group and surface area of anatase are different from rutile.[30,31] The energy band structure and surface chemistry are the key factors in photoactivity. The band gap energy of anatase (3.2 eV) corresponds to UV light (388 nm) while the band gap energy of rutile (3.0 eV) corresponds to violet light (413 nm). The difference in band gap comes from the level of conduction band of anatase which is higher than that of rutile by about 0.2 eV. Thus the electrons from the conduction band of anatase have higher reducing power than rutile.[31]

1.5.2 Tungsten Trioxide (WO_3)

WO_3 belongs to a family of transition metal oxides like TiO_2. It is an n-type semiconductor with a band gap energy of 2.8 eV. It has an idealized structure consisting of WO_6 octahedra joined at their corners (Figure 1.10).[32]

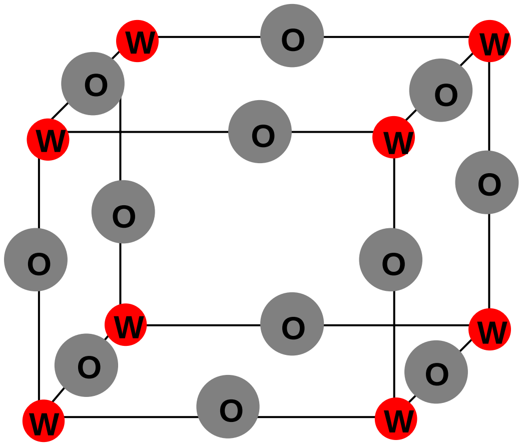

Figure 1.10: Unit cell of WO_3.

1.5.3 Copper (I) Oxide

Cu_2O is a p-type semiconductor with a direct energy band gap of 2.1 eV. It is an eminently suitable material for photoelectrochemical (PEC) applications because its constituent elements (copper and oxygen) are both plentiful and non-toxic. This is an important feature that separates Cu_2O from Group II-VI and III-V compound semiconductors that have been recently considered for the photoelectrochemical splitting of water. While there are reports of overall water splitting driven by visible light irradiation of Cu_2O,[33,34] doubts have since been raised about the viability of this approach.[35]

Cu_2O is a p-type semiconductor due to the presence of Cu vacancies which form an acceptor level 0.4 eV above the valence band.[36] The unit cell of Cu_2O is shown in Figure 1.11, and the properties of Cu_2O are tabulated in Table 1.2.

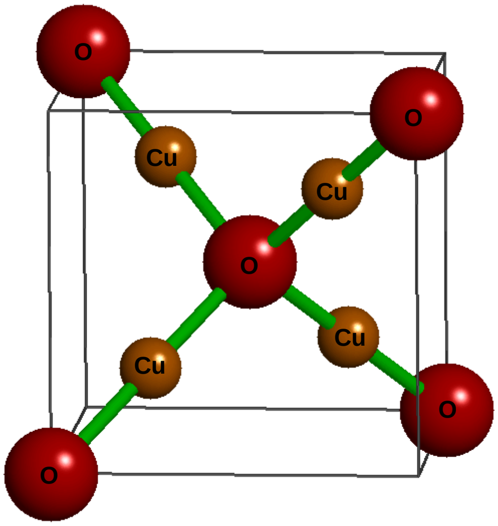

Figure 1.11: Unit cell of Cu_2O.

Table 1.2: Crystallographic properties of cuprous oxide (Cu_2O)
(http://ruby.colorado.edu/~smyth/min/cuprite.html)

Formula	Cu_2O
Formula weight	143.079
Z	2
Crystal system	Cubic
Point group	m3m
Space group	Pn3m
Unit cell	
a (Å)	4.2696
Volume	77.833
Molar volume	23.439
Density	6.104

Cuprous oxide is one of the few p-type semiconductors that can be prepared by electrodeposition, i.e., by reduction of metal ions in a suitable electrolyte solution.[37-39] The electrical properties depends strongly on the preparation conditions.[37a,38-40] As will be discussed next, electrodeposition is an inexpensive and simple method, offering control over the stoichiometry and thickness of the layers. Cu_2O has already been deposited on several substrates including Pt, Au, Cu, ITO and stainless steel.[37a,38-41]

1.5.4 Electrodeposition of Metal Oxide Semiconductors

The cathodic electrosynthesis of metal oxides has a more recent history relative to their chalcogenide counterparts. This topic has been reviewed.[42-44] Two types of cathodic deposition processes can be envisioned from a mechanistic perspective. The first involves a change in the oxidation state, as exemplified by the cathodic electrosynthesis of Cu_2O from Cu(II) precursor species.[37] The second type is not based on a change of the metal oxidation state but on an electrochemical reaction involving oxygen or other additives (e.g., nitrate).[45-47] The net effect is electrochemical generation of OH^- ions and subsequent precipitation of the oxide/hydroxide phase.[42-44] A post thermal anneal then serves to convert the hydroxide phase to the desired oxide material. Thus it has been shown that WO_3 and TiO_2 thin films can be cathodically electrosynthesized from peroxytungstate and titanyl ion precursor solutions, respectively.[48-57] Our group has pioneered the use of pulsed deposition and occlusion electrosynthesis for the controlled growth of WO_3-TiO_2 nanocomposites.[58,59] The basic electrochemical cell setup used for electrodeposition is shown in Figure 1.12.

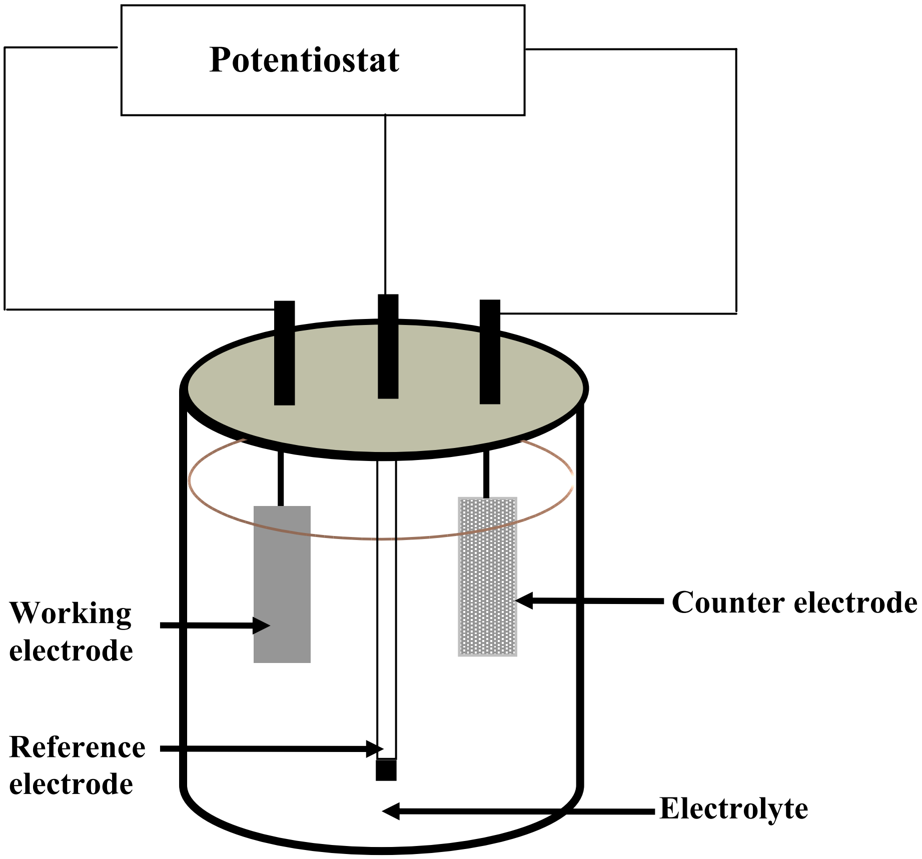

Figure 1.12: Schematic diagram of a standard single-compartment, three-electrode electrochemical cell used for electrodeposition in this study.

1.6 Nanocomposite or Layered Oxide Semiconductor Films

Composite films comprised of particulate semiconductors present interesting frameworks for exploring photoinduced electron transfer phenomena.[60] Such films are also important in practical applications for sensors, photocatalysis, heterogeneous catalysis, and the like. Other than the primary (inorganic) semiconductor component, the second (complementary) component of choice in these composite films can be a metal, another inorganic semiconductor, or an inorganic polymer.[12]

1.6.1 WO_3-TiO_2 Nanocomposite Films

There is much current interest in composite films containing WO_3 and TiO_2. These oxides are both n-type semiconductors with optical band gaps in the 2.8-3.2 eV range. A higher photoresponse was observed for bicomponent WO_3/TiO_2 films relative to single-component films.[58,61] This is because of the lower-lying conduction band of WO_3 relative to TiO_2. Optical excitation of the TiO_2 results in photoinduced electron transfer from TiO_2 into WO_3 and optical excitation of WO_3 results in photoinduced hole transfer from WO_3 into TiO_2 resulting in lowered carrier recombination and improved photoresponse (Figure 1.13).[61-63]

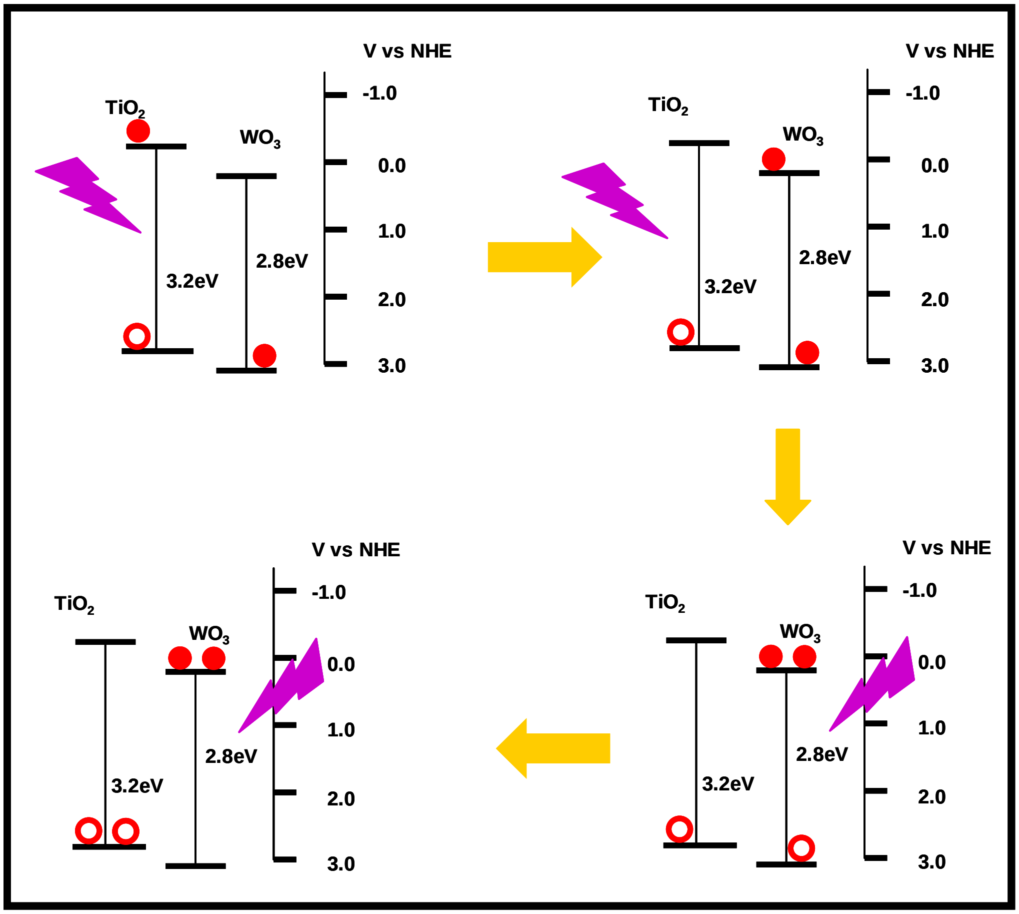

Figure 1.13: Schematic diagram showing vectorial charge transfer between the TiO_2 and WO_3 components in the composite.

The photocatalytic activity of WO_3-TiO_2 films was found to ca. 3 times that of pure TiO_2 films for the gas phase oxidation of 2-propanol.[64] Tungstated titania catalysts are also important in heterogeneous catalytic applications.[65,66] A TiO_2 coating was coupled with a WO_3 'electron pool' in the design of a photoelectrochemical anticorrosion system with built-in energy storage capability.[67] A TiO_2-WO_3 buffer layer between the transparent conducting oxide substrate and the P25 TiO_2 layer was found to be beneficial in the operation of a Ru(II)-dye sensitized solar cell.[68] The two oxides, WO_3 and TiO_2 have complementary electrochromic properties[69,70] and an electrochromic WO_3 layer has been combined with a photoactive dye covered TiO_2 layer in the construction of photoelectrochromic devices.[71,72] A photovoltaically self-charging battery based on a dye-modified TiO_2 film in contact with an inner layer of WO_3 has been described.[73] Also, it has been shown that WO_3-TiO_2 composites behave as a varistor with non-linear electrical behaviour.[74] Another important potential application of WO_3-TiO_2 is in energy storage. Thus the WO_3 component can accept the photogenerated electrons from TiO_2 and store them for subsequent use after the light is turned off. Of course, electron ingress into WO_3 necessitates a concomitant cation flux to maintain charge neutrality. Thus the WO_3 matrix morphology has to be porous enough to facilitate ion fluxes. Electrosynthesis is a superb tool to control deposit morphology. As seen earlier, electrodeposition offers a convenient and versatile route to the preparation of many inorganic oxides[42,43] including WO_3[48-53] and TiO_2.[54-57]

1.7 Photoelectrochemical Hydrogen Production

Conventional energy resources such as coal, petroleum products, etc., which are being used to meet most of the world's energy requirements, have been depleted to a great extent. It is therefore necessary to envision an alternative fuel which should in principle be pollution-free, renewable and economical. Hydrogen satisfies the first condition and to fulfill the second and third requirements, research has been intense during the past few decades.

Attractive features of hydrogen as an energy carrier are: (a) It can be produced virtually in unlimited quantities from vast renewable resources of the earth, e.g., water. (b) On combustion, water is regenerated and there is no danger of resource depletion, as is the case with fossil fuels. (c) It is a clean fuel and combustion causes no pollution of any kind to the environment. (d) Its energy value (the heat of combustion per gram) is much higher than any other fuel.

Heterogeneous photocatalysis is one of the techniques applied for the generation of hydrogen and oxygen in aqueous solution using semiconductor catalysts. This photocatalytic technique is considered to be feasible and attractive for practical purposes since one can use natural sunlight as an irradiation source in the future. Fujishima and Honda first reported in 1972, the generation of hydrogen and oxygen in a photoelectrochemical cell using TiO_2 electrode illuminated with near UV light.[75]

The decomposition of water is an endothermic reaction. It requires an input energy of 237 $kJmol^{-1}$ and the theoretical minimum photovoltage needed for this process at 25 °C is only 1.23 V. Semiconductors in the presence of light energy are capable of decomposing water depending upon the energy levels of their conduction and valence band edges. In an ideal system, the conduction band level should be well above (more negative than) the hydrogen reduction level and valence band edge should be well below (more positive than) the water oxidation level for an efficient production of hydrogen and oxygen from water by photolysis (Figure 1.14a). Thus depending upon the relative positions of the energy levels of valence and conduction bands with respect to H^+/H_2 and OH^-/O_2 levels, semiconductors can used to decompose water using solar energy (Figure 1.14). Figure 1.14b describes the situation where a sacrificial electron donor is introduced to the medium. Figure 1.14c depicts a situation where the photogenerated electrons are used to reduce a sacrificial electron acceptor (e.g., methyl viologen) which in turn reduce the protons to hydrogen (equations 1.10 and 1.11). These two situations (Figures 1.14 (b) and (c)) makes the hydrogen generation somewhat simpler compared to the situation shown in Figure 1.14(a) since the oxidation of water requires four electrons.

$$MV^{2+} + e^- \longrightarrow MV^{\bullet+} \quad (1.10)$$

$$MV^{\bullet+} + H^+ \xrightarrow[\text{(Pt)}]{\text{Catalyst}} H_2 \quad (1.11)$$

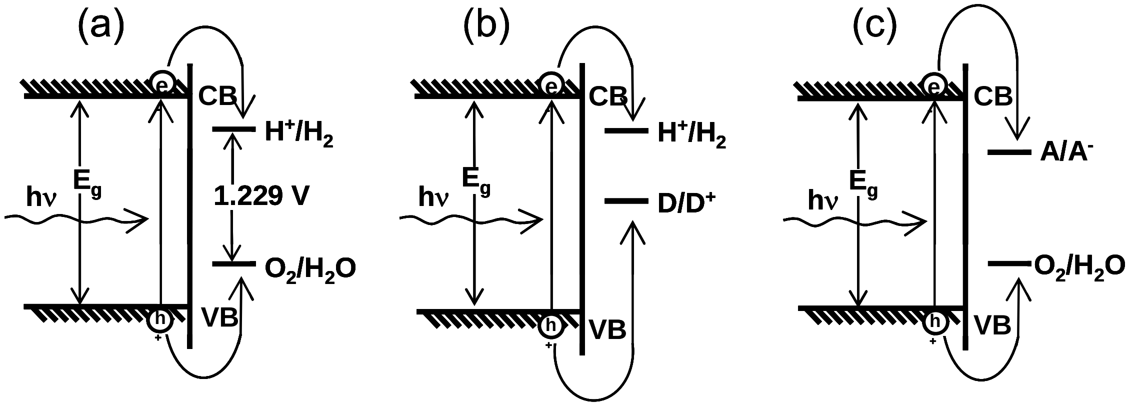

Figure 1.14: Schematic diagrams of various configurations of semiconductor based photocatalytic H_2 generation.

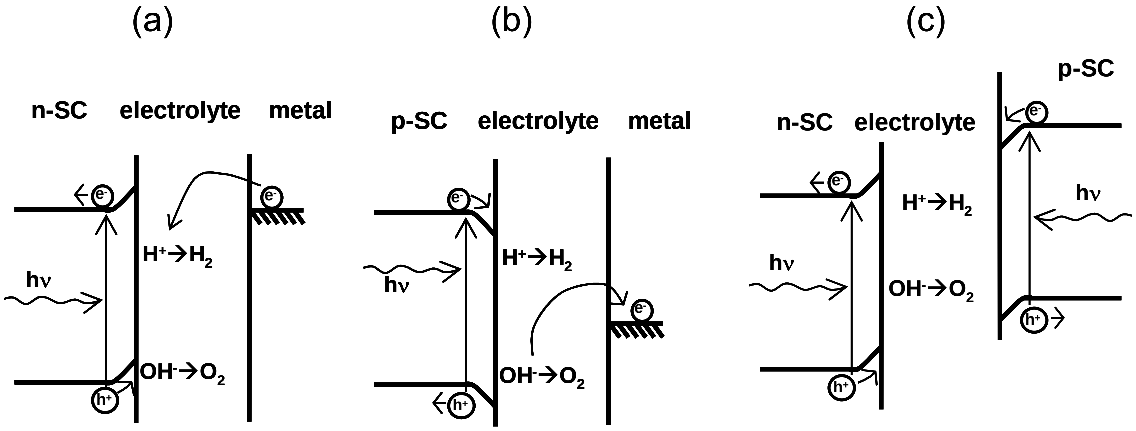

Figure 1.15: Schematic diagrams of various configurations of PEC cells for H_2 generation.

Photoelectrochemical (PEC) cells also can be used to generate hydrogen. Figure 1.15 shows schematic diagrams of various configurations of PEC cells that can be used to generate hydrogen. PEC cells where the two compartments (cathodic and anodic compartments) are isolated from one another are convenient for this purpose, since the produced hydrogen can be separated easily. This also will help to maintain electrolytes with different pH values in the two compartments (low pH is favorable in the cathodic compartment and high pH is favorable in the anodic compartment) – a tactic which was first successfully employed by Fujishima and Honda.[75]

Semiconductors that are suitable for hydrogen generation include CdS, Cu_2O, TiO_2 etc. (Figure 1.16). However most of these materials cannot be practically used due to either too wide a band gap energy to efficiently harness sunlight or their photocorrosive nature.

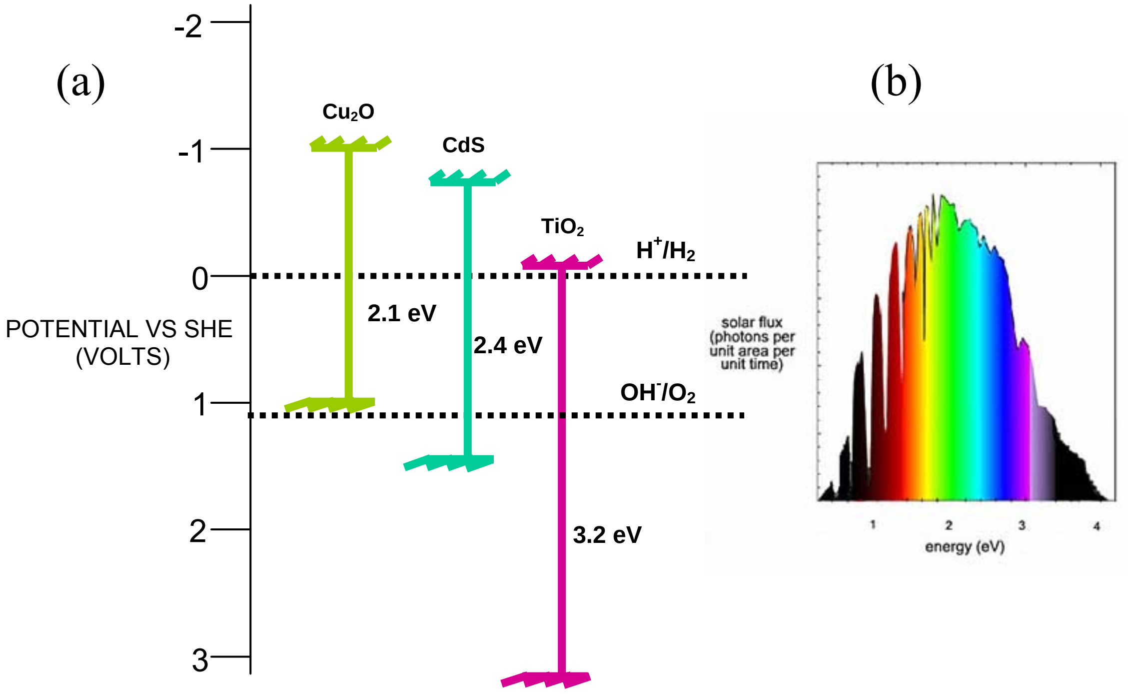

Figure 1.16: (a) Relative positions of the energy levels of valence and conduction bands of selected semiconductors with respect to H^+/H_2 and OH^-/O_2 levels at pH 0.[27, 37a]
(b) Solar spectrum.

As mentioned earlier, TiO_2 is a very stable n-type semiconductor. But the problem with this semiconductor is that its band gap energy is 3.2 eV. The wavelength region that suits this energy is <400 nm (UV region). Considering the solar spectrum, only 4% of the total solar energy could be used (Figure 1.16(b)). Studies have been reported with UV lamps, using pure TiO_2 or TiO_2 based semiconductor powders as photocatalysts.[76-79] The use of a semiconductor that absorbs in the visible region is preferable since the energy-rich portion of the solar spectrum lies in the visible region (Figure 1.16(b)). Cu_2O is a good candidate in this regard since it absorbs in the visible region of the solar spectrum. But the problem with this semiconductor is that it undergoes photocorrosion:

$$h^+_{vb} + Cu_2O + 2OH^- \longrightarrow 2CuO + H_2O \qquad (1.12)$$

$$e^-_{cb} + Cu_2O + H_2O \longrightarrow Cu + 2OH^- \qquad (1.13)$$

This dissertation work describes how modifications can be made to suppress photocorrosion and improve the photoresponse of p-Cu_2O semiconductor.

The light-to-hydrogen conversion efficiency of semiconductor photoelectrodes and of semiconducting particle suspensions depends on the relative rates of the desired photoelectrochemical reaction and the undesired carrier recombination and leakage processes. Near the reversible potential, the rate of hydrogen evolution at a clean or oxidized semiconductor surface is usually negligible. But according to Heller et.al.,[80] hydrogen evolution can be greatly accelerated and the Gibbs free energy efficiency of light-to-hydrogen conversion correspondingly increased, by incorporating a small amount of metal catalyst on the surface of the semiconductor. Metal incorporation on the surface of p-type semiconductor photocathodes to catalyze hydrogen evolution leads to efficient solar to chemical conversion if a set of energetic and kinetic criteria are satisfied:[81] (a) The semiconductor-catalyst junction barrier height must be equal to or greater than that of the semiconductor H^+/H_2 junction; (b) The recombination velocity of photogenerated electrons at the semiconductor-catalyst interface must be low; (c) The overpotential for hydrogen evolution at solar cell current densities (~30 mA/cm^2) must be low.[81]

1.7.1 Work Function of Metals and Semiconductors

Electrons can be extracted from a metal in vacuum when light with a proper wavelength impinges on the metal (photoelectric effect). In order to observe this effect, the wavelength of the incident light must have a higher energy than a critical (threshold) value. In other words, the photons must carry enough energy to extract electrons from the metal and eject them into the vacuum. This energy $E=h\nu$ must be at least equal to the "work function" of the metal, noted as $q\Phi m$ (Figure 1.17). The work function is therefore defined as the energy that must be supplied to an electron with an energy E_{Fm} (the metal Fermi level) in order for the electron to be ejected from the metal phase. Similarly, the work function of the semiconductor is the energy required to extract an electron located at its Fermi level, E_{Fsc}.[26]

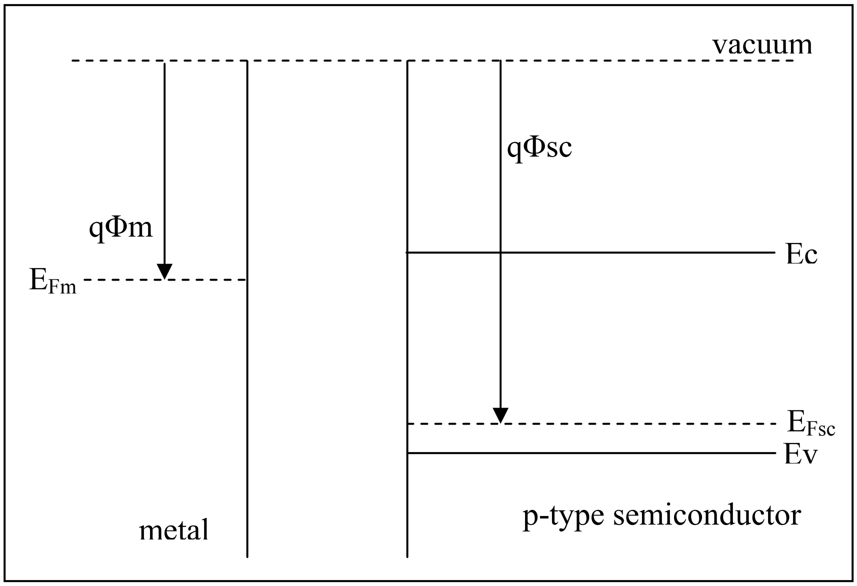

Figure 1.17: Energy bands in a metal and a semiconductor.

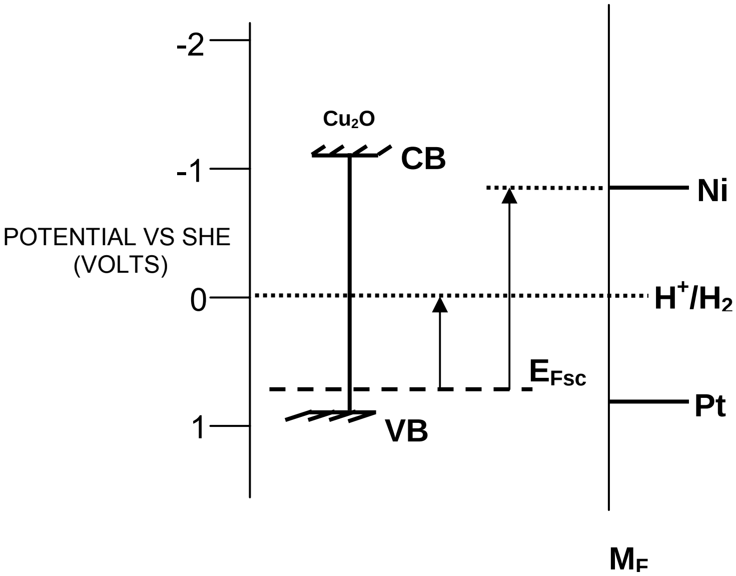

Figure 1.18: Work functions of Pt and Ni and positions of the valance and conduction bands of Cu_2O with respect to the standard hydrogen electrode (SHE).

Figure 1.18 shows that nickel would be a suitable candidate for Cu_2O as a hydrogen evolution catalyst. Also, an ultrathin nickel coating on the surface of the Cu_2O photoelectrode could minimize the contact of the Cu_2O with the aqueous electrolyte and thus reduces the photocorrosion of the oxide semiconductor. Nickel metal is used as a cathode in the water electrolyzers due to its high electrocatalytic activity towards hydrogen evolution reaction.[82-84] Attempts have been made to prepare nickel electrodes of high specific surface areas. These include sintered microporous nickel,[85] nanoporous Raney-Ni[84,86] and nickel-coated reticulated vitreous carbon.[87] Studies have been carried out using nickel in various forms for hydrogen evolution reaction. These include Ni-Ti composites,[88] Ni + RuO_2 co-deposited electrodes,[89] carbon fiber-nickel type material,[90] zinc-nickel deposits,[91] Ni-Fe-C cathodes,[92] and amorphous Ni-S-Co alloy.[93]

CHAPTER 2

EXPERIMENTAL

2.1 Chemicals and Materials

Zinc sulfate (Aldrich, 99%), cadmium sulfate (Aldrich 98%), thallium sulfate (Johnson Matthey, 99.9%), manganese sulfate (Fisher, 99.2%) Selenium(IV) oxide (Johnson Mathey, 99.9%), lead chloride (Aldrich, 99.8%) and Copper (II) sulfate (Alfa Aesar 98.0% - 102.0%)were used without further purification. Sodium sulfate (99%) and sodium formate (99%) were from Alfa Aesar and was used without further purification. All other chemicals used were also from commercial sources and were the highest purity available. They were used without further purification. The TiO_2 (Degussa P-25) used was predominantly anatase and had a specific surface area of ~60 m^2/g. Transparent conducting oxide (TCO) substrates and gold foils were used to prepare the thin films. The TCO substrate consisted of F-doped tin oxide (Nippon Sheet Glass Ltd.) coated on soda-lime glass. They were nominally ca. 400 nm thick and had a sheet resistance of 10.3 Ω/□. Strips (0.65 cm x 2 cm) were cut and cleaned in four 5 min steps of cleansing in ultrasonicated acetone, ethanol, 1:1 H_2O_2/ammonia, and finally ultra pure water. The gold foils were from Alfa Aesar. All solutions or suspensions in this study were prepared from double distilled (Corning Megapure) water (unless otherwise specified).

2.2 Instrumentation

UV-visible spectra were recorded on a Hewlett-Packard Model HP 8452-diode array spectrometer. Flame atomic absorption spectrometry (FAAS) was performed on a Perkin-Elmer 2380 atomic absorption spectrometer. Electron probe microanalysis (EPMA) was done on a JEOL JXA-8900R instrument with a beam voltage of 20 kV. X-ray photoelectron spectroscopy (XPS) used a Perkin Elmer/Physical Electronics Model 5000C instrument with other details given elsewhere.[94] Annealing and calcination of the samples were carried out using a Model 650-14 Isotemp Programmable Muffle Furnace (Fisher Scientific). The thickness of the films was measured using a stylus profilometer. Photovoltammetry and photoaction spectroscopy were performed on a Model CV-27 BAS Voltammograph equipped with a Soltec X-Y recorder Model VP-6414S. Electrodeposition and cyclic voltammetic studies were carried out on a 100A Electrochemical Analyzer [Bioanalytical Systems (BAS), W. Lafayette, IN]. A 75 W xenon arc lamp (Oriel, Stratford, CT) and a 400 W medium pressure Hg arc lamp (Philips) served as the UV light sources and a 100 W tungsten-halogen lamp (Oriel) served as the visible light source. The incident photon flux of these light sources was measured with an Oriel Model 70260 radiant power/energy meter. The monochromator used (Thermo Jarrel Ash Corporation Model 82-415) had a grating blazed at 300 nm. Scanning electron microscopy used is a Zeiss Supra 55 instrument with a nominal electron beam voltage of 5 kV.

2.3 Procedures

2.3.1 PAD of Metal Ions with Very Negative Standard Reduction Potentials

In all the experiments, the TiO_2 suspension dose was 2 g/L; the suspensions were agitated by sparging ultrapure N_2 through them. All measurements pertain to the laboratory ambient temperature (25 ± 3 ºC). The photoreactor used was described elsewhere.[95] Briefly, it consists of a reaction vessel and an ultraviolet lamp (400 W medium pressure Hg arc lamp) (Figure 2.1). The reaction vessel has inner and outer compartments. The UV lamp is place in the inner quartz compartment. The outer compartment is an immersion well vessel with a volume of 500 mL. Nitrogen was supplied through the gas inlet for providing the necessary reaction atmosphere as well as for efficient mixing of the suspensions.

For obtaining the data presented in Figure 3.1, the initial concentrations of the metal ions (Cd^{2+}, Zn^{2+}, Mn^{2+}, and Tl^{+}) in all cases were 200 μM. Prior to UV irradiation, the metal ion and sodium formate additive (ranging in concentrations from 1.0–30 mM) loaded TiO_2 suspensions were equilibrated in the dark for 30 min. Before turning on the UV light, samples were syringed out in order to determine the amount of metal ion adsorbed on the TiO_2 surface. Then the UV light was turned on and aliquots were syringed out periodically. The gas sparge was maintained throughout the experiment. The TiO_2 particles were removed by a 0.45 μM polytetrafluoroethylene (PTFE) syringe filters. The solutions were analyzed for metal ion levels remaining in the water.[10d,10e,10h] Manganese, cadmium, and thallium ion concentrations in solution were determined by flame atomic absorption spectrometry (FAAS) at 279.5 nm,

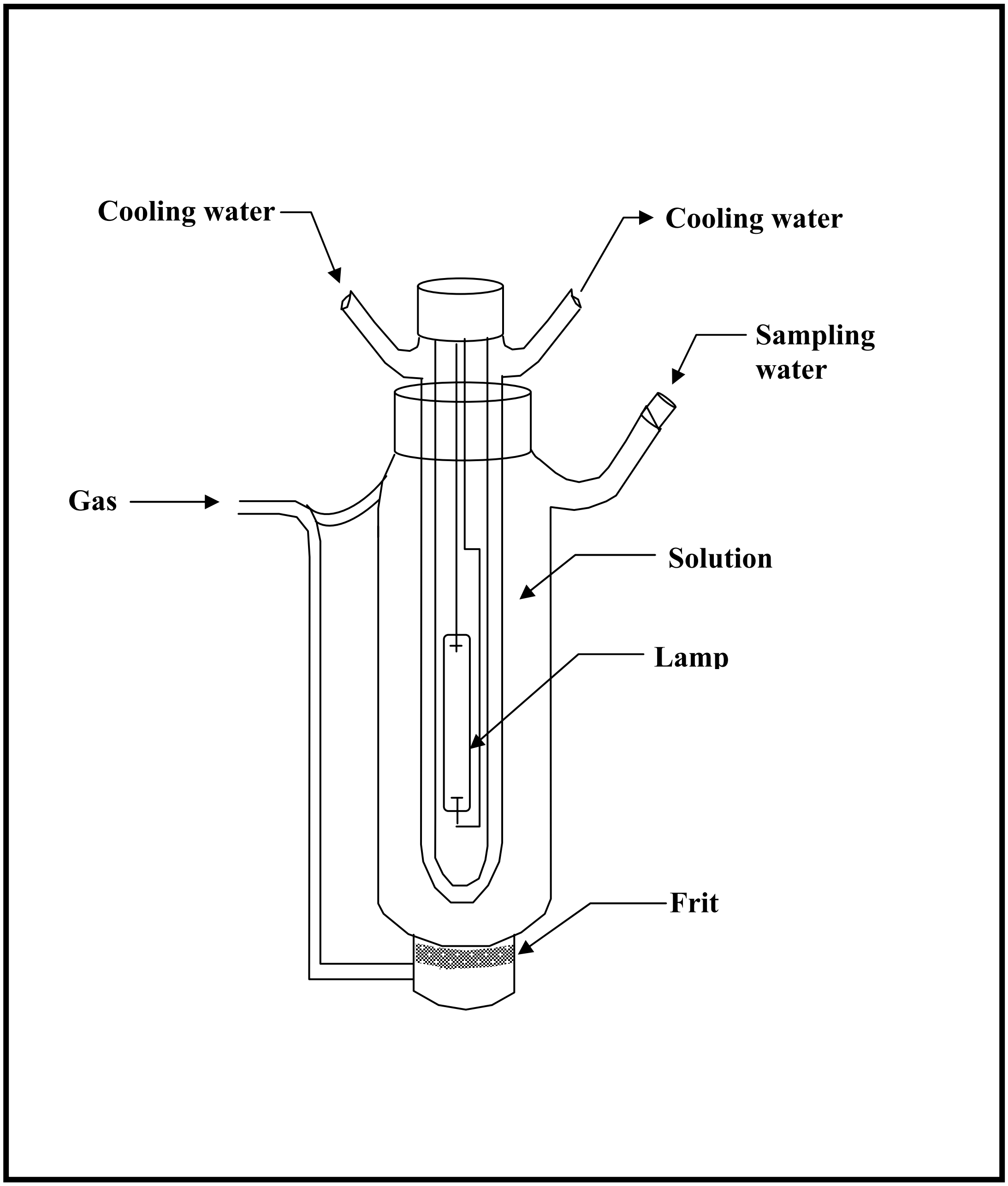

Figure 2.1: Schematic diagram of the UV photoreactor.

and 276.8 nm, respectively. The Zn(II) concentrations in solution were determined by UV-VIS spectrophotometry at 492 nm after derivatizing with 4-(2-pyridylazo)-resorcinol.[10d,10e]

A more detailed set of experiments were performed on the Tl(I) system for testing against the kinetics model. Thus unlike the procedure that led to Figure 3.1 where only a single metal ion concentration (200 μM) was utilized, runs were done at three initial concentrations of Tl(I) (200 μM, 400 μM, and 600 μM) in the TiO_2 suspensions containing variable amounts of formate in the 1–12 mM range (Figure 3.2). Alternatively, the formate concentrations were fixed at 5 mM, 10 mM, and 12 mM respectively and the Tl(I) ion concentration was systematically varied in the 100 – 800 μM range to generate the set of data in Figure 3.3.

2.3.2 PAD of Chalcogenide Semiconductors on TiO_2

The TiO_2 films were made by dip-coating gold foils (~100 mm^2 area and 0.25 mm thickness) in the Degussa P-25 TiO_2 suspensions (isopropanol containing 10 g/L oxide dose) after carefully masking one side with cellophane tape. After the dip, the foil was baked in the furnase for 10 min at ~300 ^oC. The dip-bake sequence was repeated 8 times after which, the final coated foil was baked for 17 h at ~300 ^oC. The TiO_2 film thus built up on the Au surface had a thickness in the 0.5-1 μm range.

The UV light source (75 W xenon arc lamp) served as the light source in the photovoltammetry and chronopotentiometry (CP) experiments. For the linear sweep photovoltammetry experiments, chopped irradiation (chopping frequency = 0.2 Hz) from the visible light source (100 W tungsten-halogen lamp) was used. In the chronopotentiometry and voltammetry experiments, the light source was 15 cm away from the TiO_2/Au working electrode surface, and the incident photon flux (as measured with an Oriel Model 70260 radiant power/energy meter) was in the range, 95 $\mu W/cm^2$ - 2.2 mW/cm^2. For the CP experiments, the potential changes with the light on were monitored on the Soltec Model VP-6414S recorder. The time constant of this recorder was adequate for the slow, minute-scale temporal changes of interest here.

A 100 mL quartz beaker, TiO_2/Au working electrode, and a Ag|AgCl|satd. KCl reference electrode inserted in the beaker, served as the electrochemical cell for the CP experiments. A Pt spiral was additionally employed as the counterelectrode for the photovoltammetry experiments. The supporting electrolytes in all the cases were pre-purged with ultrapure N_2 prior to the experiments. A N_2 blanket was used during the two sets of experiments.

All the experiments described were performed on supporting electrolyte solutions or on aqueous dispersions at their “natural” pH in the 6-7 range. The use of buffers was intentionally avoided to preclude their interference with either the TiO_2 surface (e.g., phosphate species are notoriously interactive with the TiO_2 surface; for example, see Refs. 96-98) or the photochemistry/photoelectrochemistry extant in the aqueous media of interest. All the experiments here pertain to the laboratory ambient temperature ($25 \pm 3\ ^0C$).

2.3.3 Occlusion Electrosynthesis of WO_3-TiO_2 Nanocomposite Films

Our Degussa P 25 TiO_2 samples had a somewhat higher anatase content (94% anatase, 6% rutile, see below) than the nominal 80:20 (anatase:rutile weight%)

composition usually described in the literature, for example, Ref. 99. Aliquots of 1.5 g were subjected to calcination in air using the muffle furnace. A linear heat cycle (at 10 ^{0}C/min) from room temperature to pre-selected final temperatures of 450 ^{0}C, 600 ^{0}C, 650 ^{0}C, 700 ^{0}C, and 800 ^{0}C was followed by a 2 h equilibrium at the final temperature; the samples were then allowed to cool naturally within the furnace back to the ambient condition. The 800 ^{0}C calcination run revealed significant densification of the sample (i.e., the volume had shrunk ca. 1/3 of the original).

A standard single-compartment, three-electrode electrochemical cell was used both for film preparation and for the photoelectrochemical measurements. A Pt coil and a Ag|AgCl| satd. KCl reference electrode (Microelectrode Inc.), along with the TCO substrate as the working electrode, completed the cell set-up. The electrodepositions were performed under constant magnetic stirring in occlusion electrosynthesis method to promote the uptake of TiO_2 particles during the electrodeposition process. UV light source (75 W xenon arc lamp) was used for the photoelectrochemical studies.

The WO_3 film matrix was cathodically electrosynthesized from a peroxytungstate deposition bath[53,58] dosed with the Degussa P 25 TiO_2 particles (either off the shelf or calcined as described above). This occlusion electrosynthesis approach has been described in more detail elsewhere.[60] The particles were kept in suspension via magnetic stirring during electrosynthesis of the composite films. The suspension was also purged with pre-purified N_2 (or argon) to remove dissolved O_2. The WO_3 deposition bath consisted of 25 mM Na_2WO_4 and 0.075% (v/v) H_2O_2 with pH adjusted to 1.4 with nitric acid.[53,58] All films were grown at the ambient laboratory temperature

(25 ± 3 ^{0}C) at -0.45 V (*vs*. Ag|AgCl|satd. KCl reference; all potentials are quoted with respect to this reference); they were then given a post-deposition thermal anneal at 450 ^{0}C for 30 min.

The composite film thickness ranged from 600 nm to 1.00 μM depending on the electrodeposition duration (10 min or 30 min) and the TiO_2 particle dose in the bath. The latter was varied from 0.32 to 3.2 mg/mL. In general, the deposition current slowly increased with time finally attaining a plateau. Figure 3.13 contains examples of the deposition current-time profiles.

2.3.4 Pulsed Electrodeposition of WO_3-TiO_2 Layered Films

Here also a standard single-compartment, three-electrode electrochemical cell was used both for film preparation and for the photoelectrochemical measurements. A Pt coil and a Ag|AgCl| satd. KCl reference electrode (Microelectrode Inc.), along with the TCO substrate as the working electrode, completed the cell set-up. UV light source (75 W xenon arc lamp) was used for the photoelectrochemical studies.

Tungsten trioxide films were cathodically electrosynthesized from a peroxytungstate deposition bath that has been described elsewhere.[53] Briefly, the bath consisted of 25 mM Na_2WO_4 and 0.075% H_2O_2 with the pH adjusted to 1.4 with HNO_3. Films were grown at –0.45 V (*vs*. Ag|AgCl|satd. KCl reference; all potentials are quoted with respect to this reference) for a nominal duration of 10 min.[53] They were then subjected to a post-deposition thermal anneal at 450 ^{o}C for 30 min. The nominal film thickness (as measured by stylus profilometry) was 250 ± 50 nm.

Titanium dioxide films were cathodically electrosynthesized from a titanyl ion precursor bath also containing nitrate ions.[54] The bath preparation has been described by other authors[54] but briefly consists of dissolving Ti powder in a solution containing H_2O_2 and NH_3. The gel initially formed is redissolved in HNO_3. The pH of this solution is then adjusted to 1.7 with dilute NH_3. Film formation occurs in this process by the initial electrogeneration of base and an increase in the local pH at the substrate/solution interface.[42,43] Thus the titanium precursor concentration (15 mM), bath pH (~1.7), and applied potential (-0.95 V) must be precisely controlled to secure good-quality films. Considerable effort was initially expended to optimize the film deposition variables. The precursor bath was used immediately after preparation and nominal film deposition period was 25 min. The deposited titanium oxy-hydroxide films[54] were subjected to a post-deposition thermal anneal at 450 ^{o}C for 30 min in the muffle furnace.

Based on previous experiments, the pulse deposition potential sequence illustrated in Figure 2.2a, was employed for the preparation of WO_3-TiO_2 composite films labeled WO_3-TiO_2 (A).[58,63] Successive deposition from two separate baths A and B using deposition potential sequence shown in Figure 2.2b yielded WO_3-TiO_2 composite films labeled WO_3-TiO_2 (B). Potential pulses at –0.45 V and –0.95 V triggered the deposition of WO_3 and WO_3/TiO_2 respectively in the case of WO_3-TiO_2 (A) composite film and WO_3 and TiO_2 in the case of WO_3-TiO_2 (B) composite film. Thus the pulse sequence started with the deposition of only WO_3 such that the inner portion of the composite film was designed to be rich in WO_3. The pulse duration at

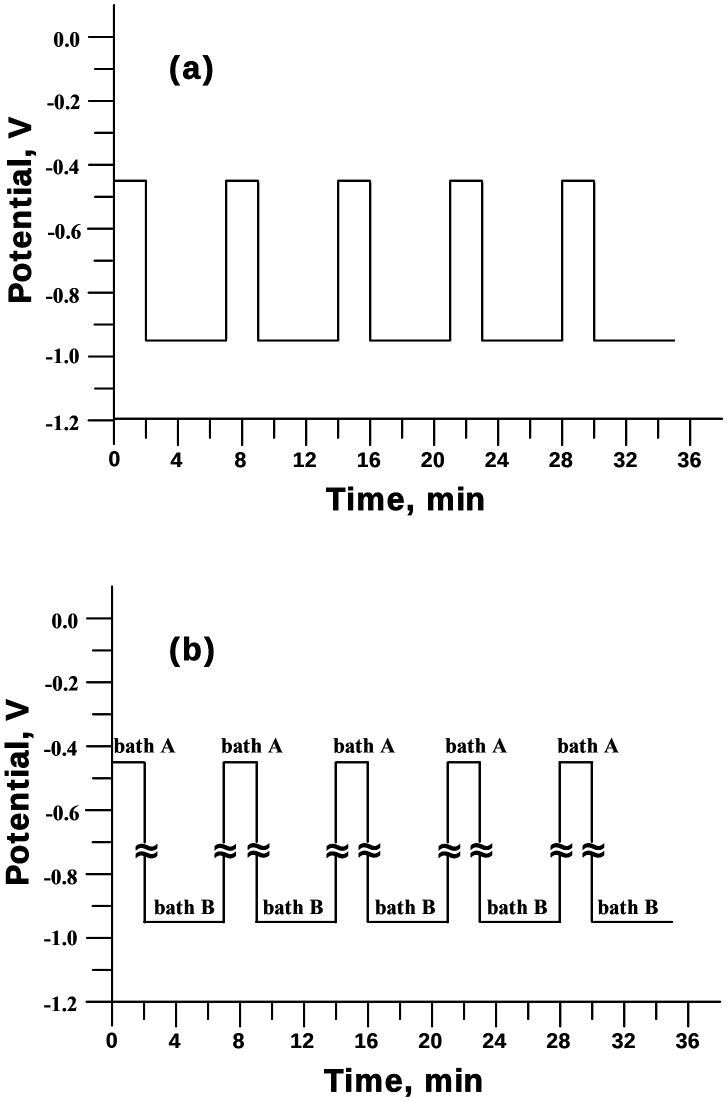

Figure 2.2: Pulsed deposition potential waveform for the formation of WO_3-TiO_2 composite films (a) WO_3-TiO_2 (A) and (b) WO_3-TiO_2 (B). Pulse potentials are -0.45 and -0.95 V.

–0.95 V was twice that at –0.45 V (Figure 2.2) to compensate for the much more sluggish deposition of TiO_2 relative to WO_3.

The composite films, WO_3-TiO_2 (A), were prepared using baths containing metered aliquots of the precursor bath mix for each component (WO_3 and TiO_2) and pre-mixed as described below. The deposition bath contained 18.5 mL of 25 mM peroxytungstate ion precursor and 1.5 mL of 200 mM titanyl ion precursor, the best concentration selected based on film performance from previous studies.[58,63] The composite film WO_3-TiO_2 (B) was deposited from bath A containing 18.5 mL of 25 mM peroxytungstate precursor + 1.5 mL of water and bath B containing 1.5 mL of 200 mM titanyl ion precursor + 18.5 mL of water. The bath pH in these cases was maintained in the 1.6-1.7 range. The pre-mixed solution was used immediately after preparation and the films were grown without stirring of the bath. The WO_3-TiO_2 composite films thus grown were annealed at 450 °C for 30 min prior to use.

2.3.5 Visible Light-Driven H_2 Production Using a p-Cu_2O Photocathode

The p-Cu_2O film was cathodically electrodeposited from 0.4 M cupric sulfate bath containing 3 M sodium lactate.[37] The bath pH was carefully adjusted to 9 by controlled addition of 4 M NaOH. The use of pH buffers was intentionally avoided to preclude interferences from the buffer components (e.g., phosphate) with the interfacial behavior. For example, phosphate species are notorious in influencing oxide/solution double-layer phenomena.[98] Films were grown at -0.40 V (*vs*. Ag|AgCl|satd. KCl reference) for a nominal duration of 30 min.

A standard single-compartment, three-electrode electrochemical cell was used for film preparation. A Cu mesh and a Ag|AgCl| satd. KCl reference electrode (Microelectrode Inc.), along with the TCO substrate as the working electrode, completed the cell set-up. The deposition bath temperature was controlled at 60 ^{0}C. The nominal film thickness (as measured by stylus profilometry) was 1.0 ± 0.05 μm.

The photodeposition of Ni on p-Cu_2O surface was carried out by irradiating the TCO/Cu_2O photoelectrode with visible light, in a solution containing 0.01 M $NiSO_4$ and 5% isopropyl alcohol for 2 hr. Electrolyte solutions in the anodic compartment contained 0.05 M of one of the following sacrificial electron donors: $K_4[Ru(CN)_6]$, formate, $K_4[Fe(CN)_6]$, hydroquinone (pH=6), hydroquinone (pH=10), or triethylamine. Cyclic voltammetry was used for the selection of optimal (sacrificial) electron donor.

Cu_2O colloidal particles (nanocubes) were synthesized using 0.025 M $CuCl_2$, 0.25 M NaOH, and 0.5 M $N_2H_4.H_2O$ as described elsewhere.[100] A two-compartment, two-electrode electrochemical cell (Figure 2.3) was used to measure the photocurrent. A visible light source (150 W tungsten halogen lamp) was used for the photodeposition of Ni and for the photocurrent measurements.

For in situ monitoring of methyl viologen cation radicals ($MV^{+\cdot}$) at the irradiated p-Cu_2O/electrolyte interface, the set-up schematically shown in Figure 2.4 was employed. Similarly, Figure 2.5 contains a schematic diagram of the set-up used for transient photocurrent measurements on this system.

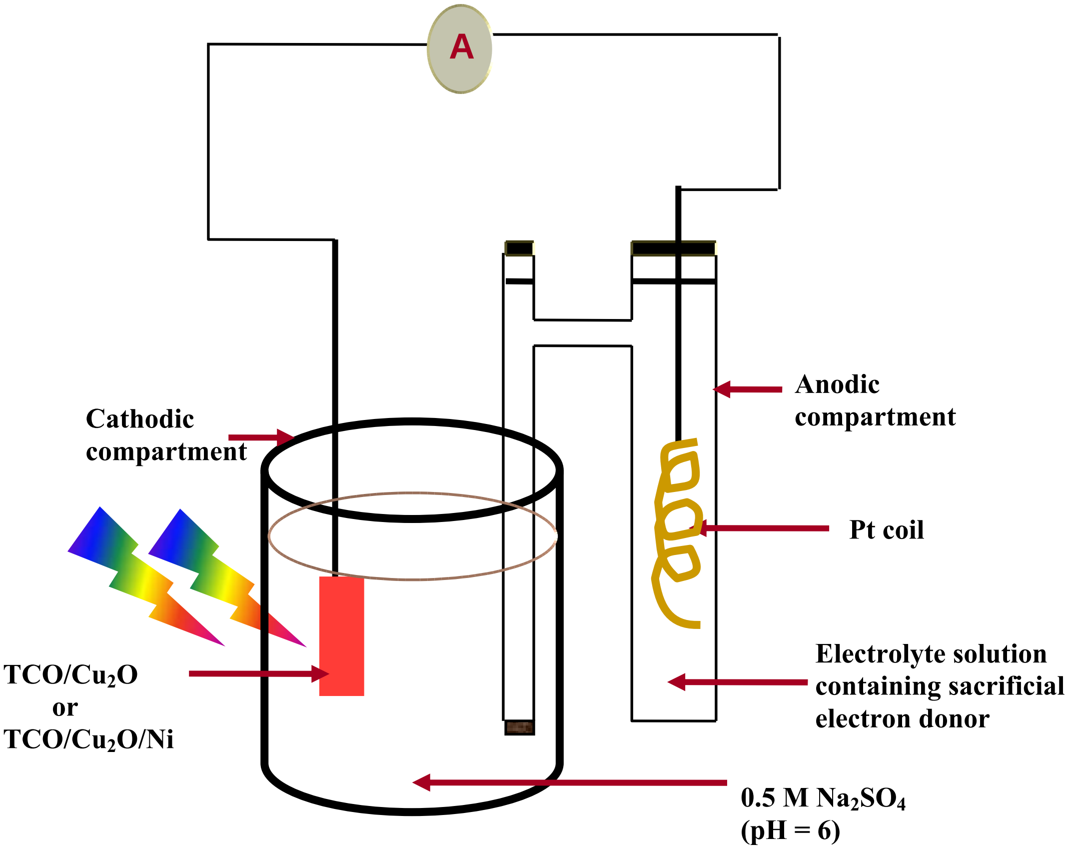

Figure 2.3: Schematic diagram of the cell set-up used to measure the photocurrent.

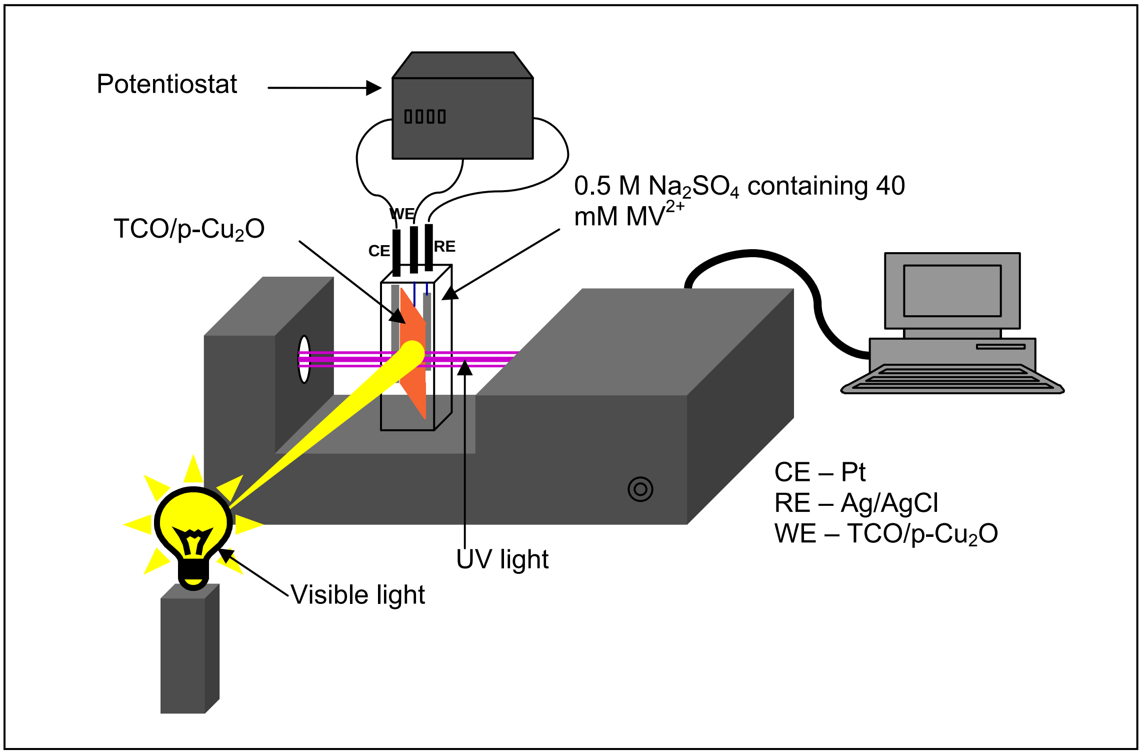

Figure 2.4: Instrumentation set-up used to monitor the formation of $MV^{\cdot+}$. A diode-array spectrometer is shown for the spectroelectrochemical measurements.

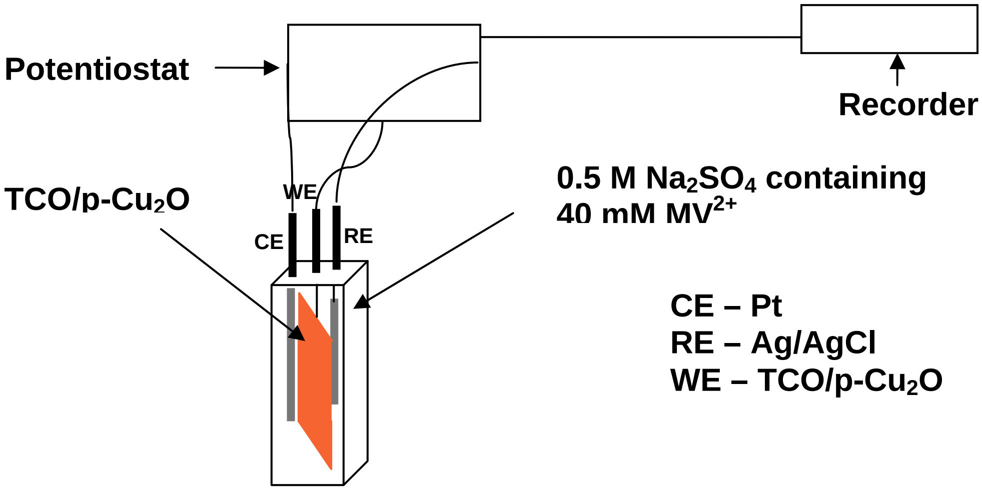

Figure 2.5: Instrumentation set-up used to measure transient photocurrents in the p-Cu_2O-based photoelectrochemical cell for H_2 generation.

CHAPTER 3

RESULTS AND DISCUSSION

3.1 PAD of Metal Ions with Very Negative Standard Reduction Potentials

3.1.1 Trends in Photoreactivity and Dark Adsorption

Figure 3.1 contains plots of the initial reaction rate versus the formate additive concentration ($[D^-]_0$) for the four metal ions considered in this study. The initial rate was determined as usual from the slopes of reactant conversion plots of metal ion concentration versus time. In all the four cases, the initial rate rapidly increases with $[D^-]_0$ in a roughly linear fashion and then attains a plateau. The rates were ordered as follows: $Cd^{2+} >> Tl^+ > Mn^{2+} > Zn^{2+}$. It must be noted that the photocatalytic conversion rates are either zero (Mn^{2+}, Zn^{2+}) or negligible (Cd^{2+}, Tl^+) in the absence of the formate additive[10h] since these metal ions either have more negative standard reduction potentials or lie very close to the TiO_2 conduction band edge (Figure 1.1) such that the direct reduction route involving photogenerated electrons in TiO_2 can be neglected. Thus the data in Figure 3.1 predominantly reflect trends in the radical-mediated indirect conversion route. It is also worth noting that the ratio $[D^-]_0/[M^{n+}]_0$ ($[M^{n+}]_0$ = initial metal ion concentration) far exceeds unity in all the experiments pertinent to Figure 3.1. The plateaus seen in Figure 3.1 in the initial rates at formate concentrations higher than

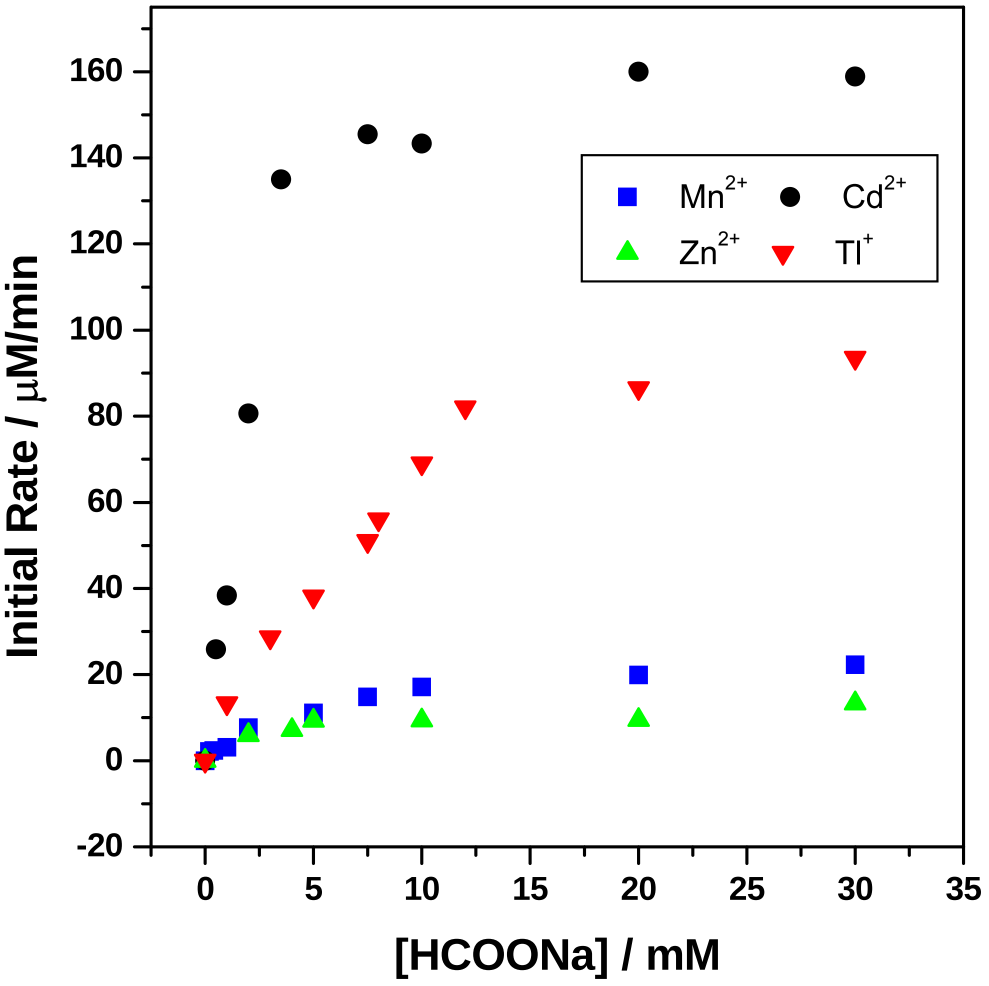

Figure 3.1: Dependence of the initial rate of metal ion photoreduction on the formate additive concentration in UV-irradiated TiO_2 suspensions. The initial concentration of the metal ion (added as the sulfate salt) was 200 µM.

5-10 mM are explained as follows. At formate concentrations lower than 5-10 mM regime, the photocatalytic reduction of 200 μM M^{n+} ions is radical-limited. At higher concentrations of formate, a proportionately higher concentration of free radicals is generated so that the process is no longer radical-limited and the conversion rate saturates.

Since the band-edge positions of TiO_2 in the solution and some solution processes (e.g., acid-base equilibria) are dependent on solution pH, considerable attention was focused on this parameter. All the experiments in this study were performed at the "natural" pH range of the oxide and metal ion/additive laden suspensions, namely ~ 6.5-7.0. The use of pH buffers was avoided because of possible interference of the buffer agent components with the oxide surface and/or the photocatalytic process. The pH values of the solutions were also monitored during the photocatalytic process; they did not change by more than 0.2 units. This is within the experimental error; note also that only the initial reaction rates were relevant for the purposes of this study. Thus the reaction time span did not exceed 5 min in all the cases. The band-edge positions in Figure 1.1 are relevant for a solution pH of ~ 7.0, and it is also worth noting that since the pK_a of $HCOO^{\bullet}$ is ~ 2.3,[101] almost all the radical species will be in the dissociated state.

It is of interest to compare the reactivity trends in Figure 3.1 with the corresponding trends for the homogenous reactions of the metal ions with $CO_2^{\bullet -}$ radicals. Bimolecular rate constants for the homogenous (one-electron transfer) reactions are available in the literature;[102] Table 3.1 lists these values. The rate constants broadly follow the same order: $Cd^{2+} > Tl^{+} > Mn^{2+} > Zn^{2+}$, as observed in the heterogeneous case. The rate constants for the heterogeneous reactions (see below) are also listed in Table 3.1.

Table 3.1: Rate constants[a] for the homogeneous and heterogeneous reactions between metal ions and formate radicals

metal ion	Homogeneous[b]	Heterogeneous[c]
	k (L $mol^{-1}s^{-1}$)	k'k'' (L $mol^{-1}s^{-1}$)
Cd^{2+}	5.1×10^{6}	3.2
Zn^{2+}	$< 2 \times 10^{4}$	0.14
Mn^{2+}	$< 2 \times 10^{5}$	0.15
Tl^{+}	3×10^{6}	0.55

[a] From Ref. 101.

[b] Single electron transfer in all cases; see text.

[c] See text and equation 3.10 for details.

One could argue that initial adsorption of the metal ion (and the formate additive) on the TiO_2 surface could play an important role in a heterogeneous photoreaction environment. Our group has shown earlier[10h] that, in the absence of formate, the proclivity of these metal ions to adsorb on the TiO_2 surface is quite low but varies amongst the four species considered. On the other hand, induced adsorption (on the TiO_2 surface) results when chelating additives such as formate are present.[10d,10e]

Possible mechanistic factors underlying this interesting trend have been discussed both by our group[10d,10e] and by other authors.[103] Table 3.2 contains the dark adsorption data for the four metal ions. In the presence of formate (the situation corresponding to the experiments addressed in Figure 3.1), the adsorption affinity follows the order: $Zn^{2+} \approx Cd^{2+} > Tl^{+} > Mn^{2+}$. Clearly, for Cd^{2+}, Tl^{+}, and Mn^{2+}, this trend parallels that seen earlier in Figure 3.1 and Table 3.1. On the other hand, the situation with Zn^{2+}shows that interfacial adsorption alone is not a determining factor in the efficacy of its photocatalytic conversion in the presence of the formate additive.

Table 3.2: Amount of metal ion adsorbed on the TiO_2 surface with and without formate ions present.[a]

metal ion[b]	amount adsorbed (μM)	
	with formate[c]	without formate[d]
Cd^{2+}	100	11.1
Zn^{2+}	110	32.6
Mn^{2+}	80	5.6
Tl^{+}	50	20

[a] See Experimental Section for details on how adsorption was quantified.

[b] Initial concentration was 200 μM in all the cases.

[c] Formate concentration was 0.05 M except for Mn^{2+} where it was 0.15 M.

[d] From Refs. 10e,10f,104.

The good correspondence of the present data with the reactivity trends for these same four metal ions in homogeneous media (Table 3.1) suggests that the dominant role of TiO_2 is as a source of the free radicals. Indeed, interfacial adsorption does not appear to be an overriding factor, at least under the experimental conditions utilized in this study.

It is also worth noting that the literature kinetics data in Table 3.1 pertain to single-electron transfer processes. On the other hand, the results in Figure 3.1 involve two-electron transfer processes with the exception of the Tl^+ case. Nonetheless, it would appear, from the similarity in trends in the two cases, that the rate-determining step is the same in both the homogeneous and heterogeneous processes. In this regard, it is worth noting that the rate constants in homogeneous media for the transfer of the second electron is orders of magnitude higher than the first step, e.g., 5.1×10^6 L mol^{-1} s^{-1} for $Cd^{2+} \rightarrow Cd^+$ versus 2×10^9 L mol^{-1} s^{-1} for $Cd^+ \rightarrow Cd^0$, Ref. 102). This is entirely consistent with the relative stabilities of the metal ions in the two oxidation states.

3.1.2 The Thallium(I) Model System: Kinetics Scheme and Comparison with Experimental Data

A simple kinetics scheme was developed and experimentally tested for the first time for the free radical-mediated (indirect) reduction route. Thallium(I) was used as the metal ion candidate for reaction with the photogenerated formate radicals for this purpose. In a historical sense, it is interesting to note that the Tl^+_{aq}/Tl^0 redox couple has been previously utilized for estimation of the reduction potentials of $CO_2^{\bullet-}$ and the alcohol radicals.[22,23,105] These prior studies in homogeneous media utilized pulse radiolysis for free radical generation.

Given that the photocatalytic (reductive) conversion of Tl(I) species involves a one-electron transfer situation, a simple reaction scheme can be written for the indirect radical-mediated reaction route

$$\mathrm{TiO_2} \xrightarrow[k_1]{h\nu\,(\mathrm{UV})} \mathrm{e^-} + \mathrm{h^+} \tag{3.1}$$

$$\mathrm{e^-} + \mathrm{h^+} \xrightarrow[k_2]{} \Delta\ (\mathrm{heat}) \tag{3.2}$$

$$\mathrm{D^-} + \mathrm{h^+} \xrightarrow[k_3]{} \mathrm{D^{\bullet -}} + \mathrm{H^+} \tag{3.3}$$

$$\mathrm{A^+} + \mathrm{e^-} \xrightarrow[k_4]{} \mathrm{A} \tag{3.4}$$

$$\mathrm{D^{\bullet -}} + \mathrm{M^+} \xrightarrow[k_5]{} \mathrm{M} + \text{products} \tag{3.5}$$

$$\mathrm{D^{\bullet -}} + \mathrm{X} \xrightarrow[k_6]{} \text{products} \tag{3.6}$$

In the above scheme, the k's are the rate constants, D^- is an electron donor (formate in our case), A^+ is an electron acceptor (e.g., O_2), M^+ is a metal ion (e.g., Tl^+), and X is a $D^{\bullet -}$ scavenger (e.g., $H^\bullet$, $OH^\bullet$ or TiO_2). It is reasonable to assume that $[X] >> [D^{\bullet -}]$. Thus step (3.6) can be treated as a pseudo-first order reaction, with a rate constant, $k_6 = k_6' [X]$.

Invoking the steady-state approximation for the formate radical anion, we obtain its concentration as

$$k_3\,[D^-]\,[h^+] = k_5\,[\overline{D^\bullet}]\;[M^+] + k_6\,[\overline{D^\bullet}] = [\overline{D^\bullet}]\;\{k_5\,[M^+] + k_6\}$$

$$[\overline{D^\bullet}] = \frac{k_3\,[D^-]\,[h^+]}{k_5\,[M^+] + k_6} \tag{3.7}$$

Thus by assuming reaction (3.5) to be the rate-determining step, the rate R for the reduction of the metal ion by the radical anion can be written as

$$R_5 = k_5[\overline{D^\bullet}]\,[M^+] \tag{3.8}$$

which, after substitution of (3.7), yields

$$R_5 = \frac{k_3k_5\,[D^-]\,[h^+]\,[M^+]}{k_5\,[M^+] + k_6} \tag{3.9}$$

Considering the situation when $k_6 >> k_5\,[M^+]$, equation 3.9 simplifies to

$$R_5 = \frac{k_3k_5}{k_6}\,[D^-]\,[h^+]\,[M^+]$$

which can be written as

$$R_5 = k'k''\,[D^-]\,[M^+] \tag{3.10}$$

with $k' = k_3\,[h^+]$ and $k'' = k_5/k_6$.

Equation 3.10 affords a route to testing this simple kinetics model against experimental data. Thus, the initial rate can be plotted against the initial concentration of formate ($[D^-]_0$) with $[M^+]_0$ held constant. Similar plots can be constructed from experiments with $[M^+]_0$ varied while maintaining $[D^-]_0$ constant. The two sets of plots should result in straight lines, and from their slopes, the product k'k" can be computed. An important test for the efficacy of the present model is that the values obtained for k'k" from the two sets of experiments should be the same, within experimental error.

Figure 3.2 displays plots of equation 3.10 generated from experiments where the initial formate ion concentration was varied, while maintaining the initial Tl^+ concentration constant at three different values. It must be noted, with respect to the Tl^+ data in Figure 3.1, that the formate ion concentrations (1-12 mM) were varied within the "linear" rate regime, i.e., not in the saturation region. As the counterpart for these sets of experiments, the Tl^+ ion concentration was varied for Figure 3.3. Most of the data points in Figures 3.2 and 3.3 are averaged values obtained from replicate (2-3) experiments so that the six plots are built from a cumulative total of 60 runs in all. The lines in Figures 3.2 and 3.3 are least-squares fits to the data points. Table 3.3 lists the six values of k'k" thus obtained from the slopes of the corresponding plots in Figures 3.2 and 3.3. These values are clearly in good accord with one another within the data scatter and experimental error.

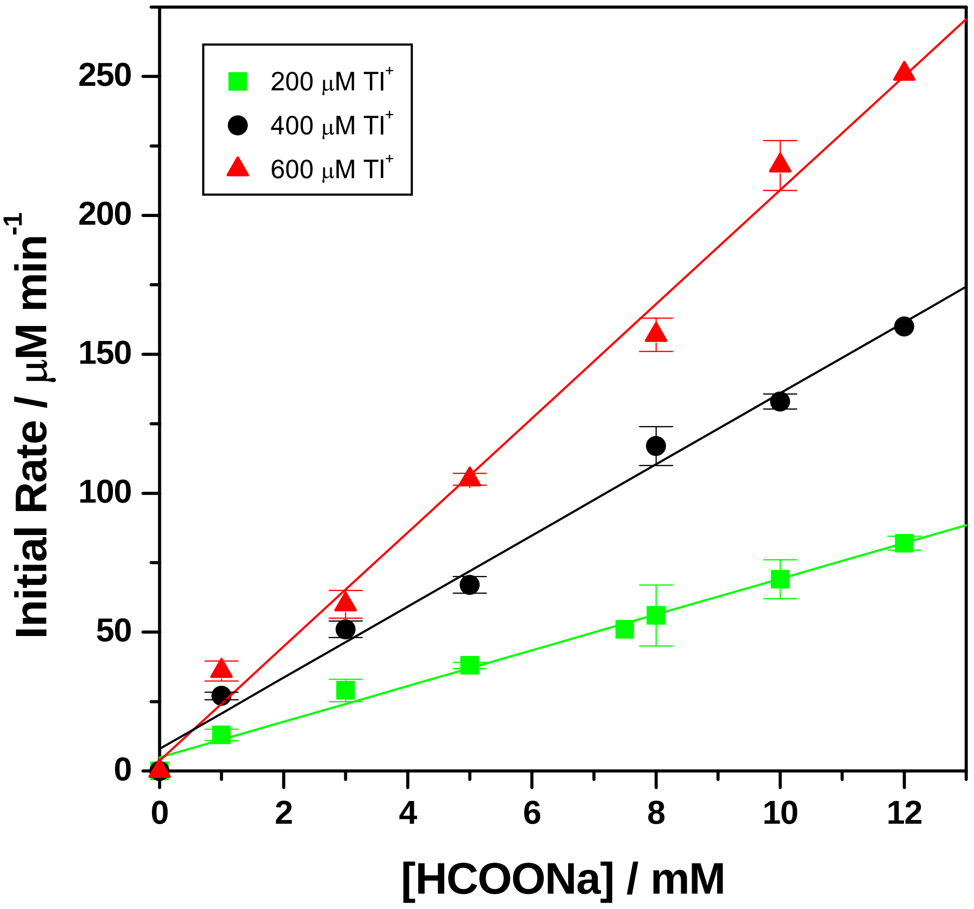

Figure 3.2: Test of the model prediction (represented by equation 3.10) for three initial concentrations of Tl(I). Other conditions are described in the Experimental Section. The lines are least-squares fits and the error bars are shown for cases where replicate experiments were performed.

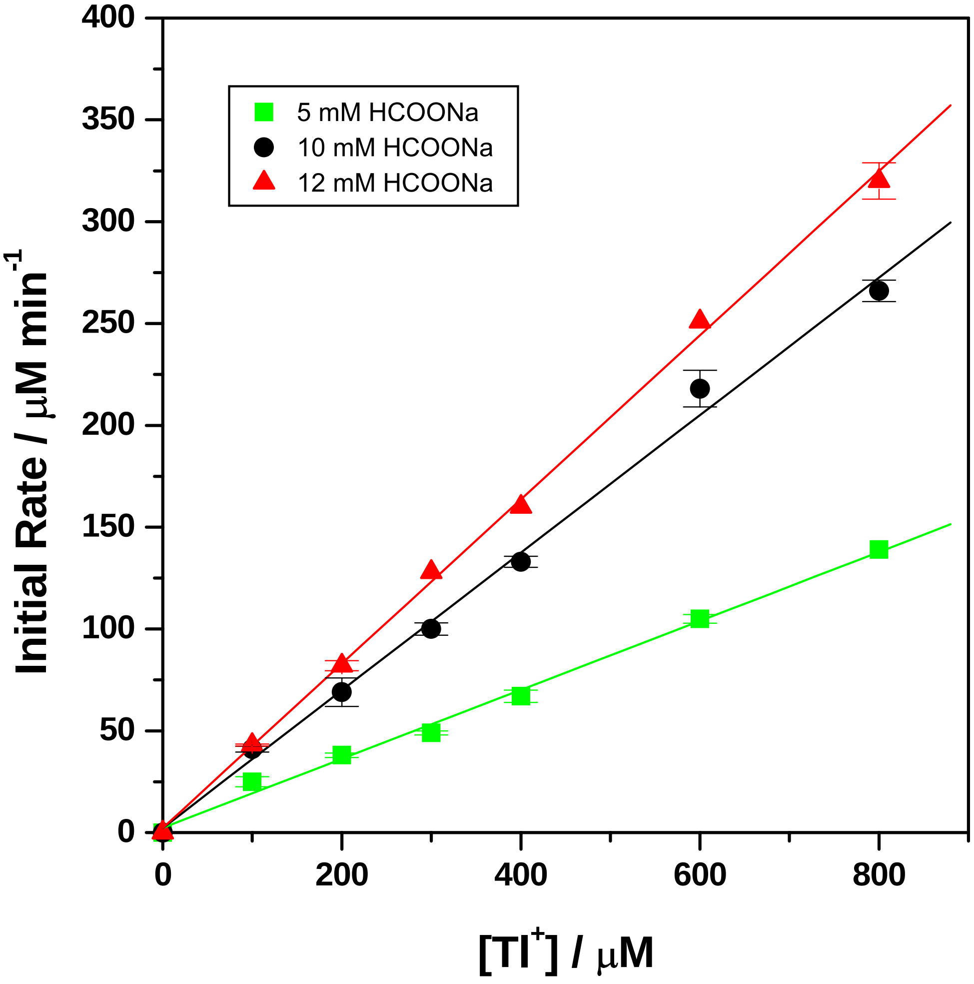

Figure 3.3: As in Figure 3.2 but for the set of experiments where Tl(I) concentration was varied while holding the formate concentration constant at the three values shown.

Table 3.3: Values of k'k" (equation 3.10) from the slopes of the plots in Figures 3.2 and 3.3.

parameter	k'k" ($Lmol^{-1}s^{-1}$)	$r^{2\ a}$
[Tl^+] = 200 μM (Figure 3.2)	0.53	0.993
[Tl^+] = 400 μM (Figure 3.2)	0.53	0.990
[Tl^+] = 600 μM (Figure 3.2)	0.57	0.990
	avg: 0.54 (±0.02)	
[HCOONa] =5 mM (Figure 3.3)	0.565	0.999
[HCOONa]=10 mM (Figure 3.3)	0.563	0.995
[HCOONa]=12 mM (Figure 3.3)	0.562	0.995
	avg: 0.563 (±0.001)	

[a] Correlation coefficient in the least-squares regression.

The excellent agreement between our model predictions and experimental data (Table 3.3, Figures 3.2 and 3.3) suggests that the simple scheme represented by equations 3.1-3.6 accounts for the essential aspects of the indirect metal ion reduction route in UV-irradiated TiO_2 suspensions, and that thallium(I) is a good model for the heterogeneous system as well.

Several points regarding our kinetics scheme deserve further discussion. Thus the role of the electron acceptor in scavenging the photogenerated electrons in TiO_2 (equation 3.4) is not specifically addressed herein. The two possible sinks for electrons are H^+ ions in solution (or at the interface) and the TiO_2 surface itself. Evidence for the participation of H^+ ions was found in our earlier study on the photocatalytic reduction of Mn^{2+} species.[10f] Charging of the TiO_2 surface by the photogenerated electrons and subsequent trapping of the latter (i.e., $Ti(IV)\text{-}OH + e^- \rightarrow Ti(III)\text{-}OH$) can be directly monitored in chronopotentiometric experiments under oxide illumination.[104]

While our first-generation kinetics scheme (equations 3.1-3.10) is undoubtedly simplified, the possible complicating role of other solution processes such as radical dimerization can be discounted. For example, the dimerization of $CO_2^{\bullet -}$ only occurs at pH values higher than ~ 8.1.[106] Other processes consuming the radicals, such as disproportionation, are mechanistically accommodated by equation 3.6 in our scheme.

Under steady-state conditions, the electron and hole fluxes on each (irradiated) TiO_2 particle in the suspension must balance one another.[107] Furthermore, the assumption leading to equation 3.10 from equation 3.9 merits scrutiny. The condition $k_6 >> k_5[M^+]$ is consistent with the typically high rate of radical annihilation steps (such as reaction 3.6) in the overall scheme. Indeed this is consistent with our experimental observation that a large excess of the electron donor (i.e., the free radical source) relative to the initial metal ion concentration is needed to sustain a measurable photocatalytic reduction rate. This condition then maximizes the encounter of a given metal ion with a free radical in its immediate vicinity. In this sense, the rate constant k" (= k_5/k_6) is a “branching ratio” in that it represents the competition between reactions (3.5) and (3.6) for consumption of the photogenerated free radical ions. It is worth noting that the opposite situation where $k_5 [M^+] >> k_6$ (see equation 3.9) would have yielded a final rate expression that does not contain a $[M^+]$ term. This would clearly be in conflict with the experimental data (see Figure 3.3).

The postulate of TiO_2 as a quencher of the $D^{\bullet -}$ species (see above) deserves comment. It is well known that oxide electrodes such as TiO_2 act as hosts for electron injection from (unstable) radicals leading to the so-called current-doubling effect.[108] This effect is likely to play a role in oxide suspensions as well, so that TiO_2 competes with the metal ions for electrons from the photogenerated formate radical anions.

Finally, this study has not specifically addressed the location of the reaction zone involving the metal ions and the photogenerated free radical ions. Nevertheless, initial concentrations and initial rates were used in equation 3.10 for successfully testing the model against the experimental data (Figures 3.2 and 3.3). This suggests that interfacial adsorption (of either Tl^+, formate ion, or both) on the TiO_2 surface exerts only a secondary effect on the overall electron transfer rate. Close examination of the results from analyzing the plots in Figures 3.2 and 3.3 (Table 3.3), however, reveals that the data scatter (and the consequent slope uncertainty) are distinctly higher in the cases where the formate concentrations were systematically varied (Figure 3.2). This is further borne out by the relative magnitudes of the regression correlation coefficients in the two sets of cases (Table 3.3). Recalling that formate ions provide the anchoring links for adsorption of Tl^+ (and other metal) ions on the TiO_2 surface,[10d,10e,10g,107] we attribute this additional data scatter to the perturbation induced by the variable formate levels on the local Tl^+ ion concentrations at the TiO_2/water interface.

Notwithstanding such subtler effects, the overall kinetics scheme and the simple rate expression in equation 3.10 do appear to provide a satisfactory description for the free radical-mediated reduction of metal ions in UV-irradiated TiO_2 suspensions. At this stage of our understanding of this interesting process, it is not yet possible to further separate the contributions of the two terms k' and k'' from the measured slopes.

3.2 PAD of Chalcogenide Semiconductors on TiO_2

3.2.1 Photocatalytic Deposition of Se and MSe on the TiO_2 Surface

Figure 3.4 maps the relative disposition of the conduction and valence band edges in TiO_2 in an aqueous medium of pH ~7. For comparison, the redox potentials of several species relevant to this part of the dissertation study are also shown on the same diagram. Thus there is no thermodynamic driving force for the direct reduction of Cd^{2+} ions by the photogenerated electrons in TiO_2, while that for the photocatalytic reduction of Pb^{2+} species is modest.[11a] On the other hand, there is appreciable driving force for the photoreduction of Se(IV) species (Figure 3.4). As Figure 3.5 and the data presented

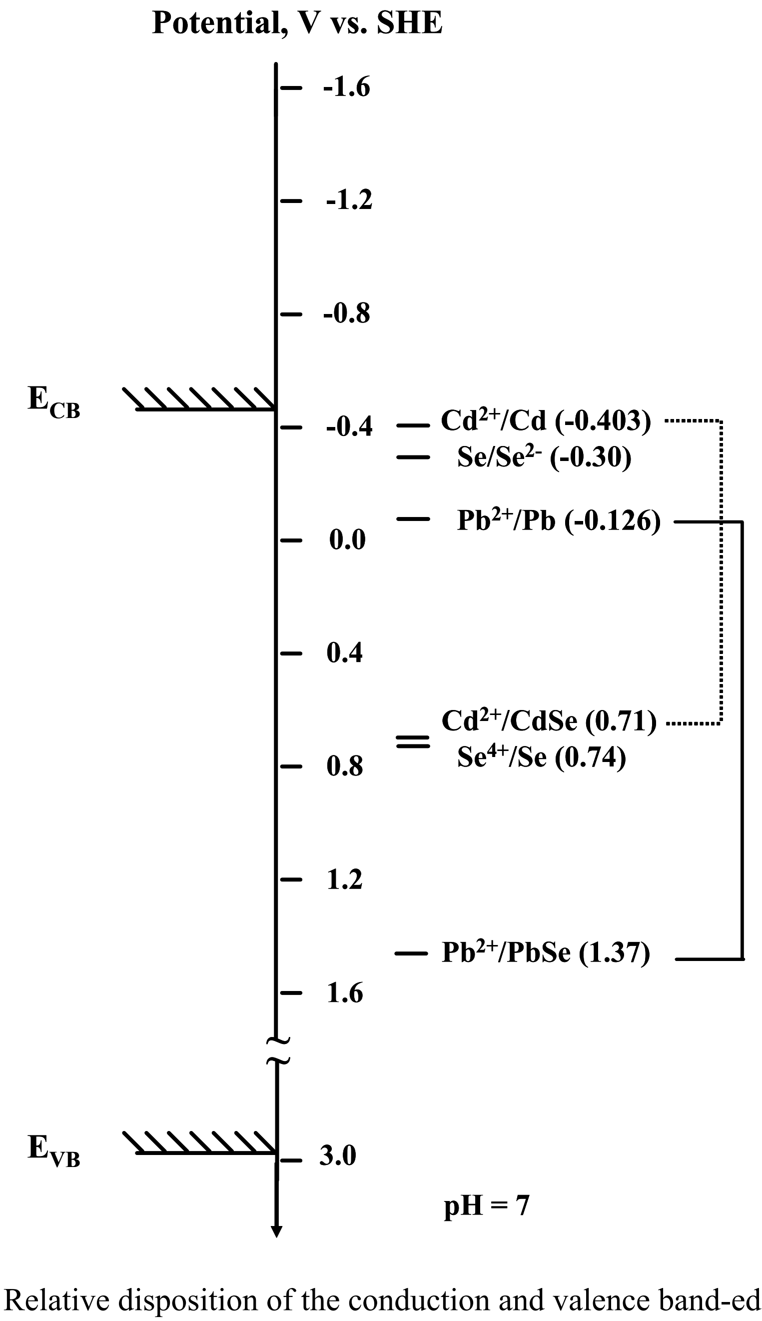

Figure 3.4: Relative disposition of the conduction and valence band-edges in TiO_2 and the redox energy levels for relevant species of interest to this study in an aqueous medium. Note the discontinuity in the potential scale at ~1.6 V (vs. SHE).

earlier on Se(IV) reduction in Ref. 11a illustrate, these predictions are very well borne out by experiment. Thus no reduction of Cd^{2+} is observed in a UV-irradiated TiO_2 aqueous dispersion over a ~6 h period (Figure 3.5a). Lead(II) species are photoreduced very slowly over a 10 h time span via a zero-order kinetics reaction (Figure 3.5b). On the other hand, Se(IV) species have a strong adsorptive affinity for the TiO_2 surface and are photoreduced in a facile manner.[11a]

The crucial aspect with the photoassisted deposition of MSe on the TiO_2 surface is that the free energy of compound formation (ΔG_{MSe}) effectively shifts the redox potentials in the $Cd^{2+/0}$ and $Pb^{2+/0}$ cases in the positive direction (Figure 3.4). This shift is somewhat larger in the PbSe case relative to CdSe because of the more favorable ΔG_{MSe} value, -264.5 kJ/mol for PbSe vs. -136.4 kJ/mol for CdSe, Refs. 109, 110. Thus on a Se-modified TiO_2 surface, the reduction of Cd^{2+} and Pb^{2+} species is driven by compound formation in much the same manner that metal alloys are deposited. Once again, experimental data (Figure 3.4) are in accord with these expectations. The solutions are depleted of Cd^{2+} (Figure 3.5a) and Pb^{2+} (Figure 3.5b) ions within ~120 min and ~60 min respectively when the TiO_2 particle surfaces are modified with the Se "template".

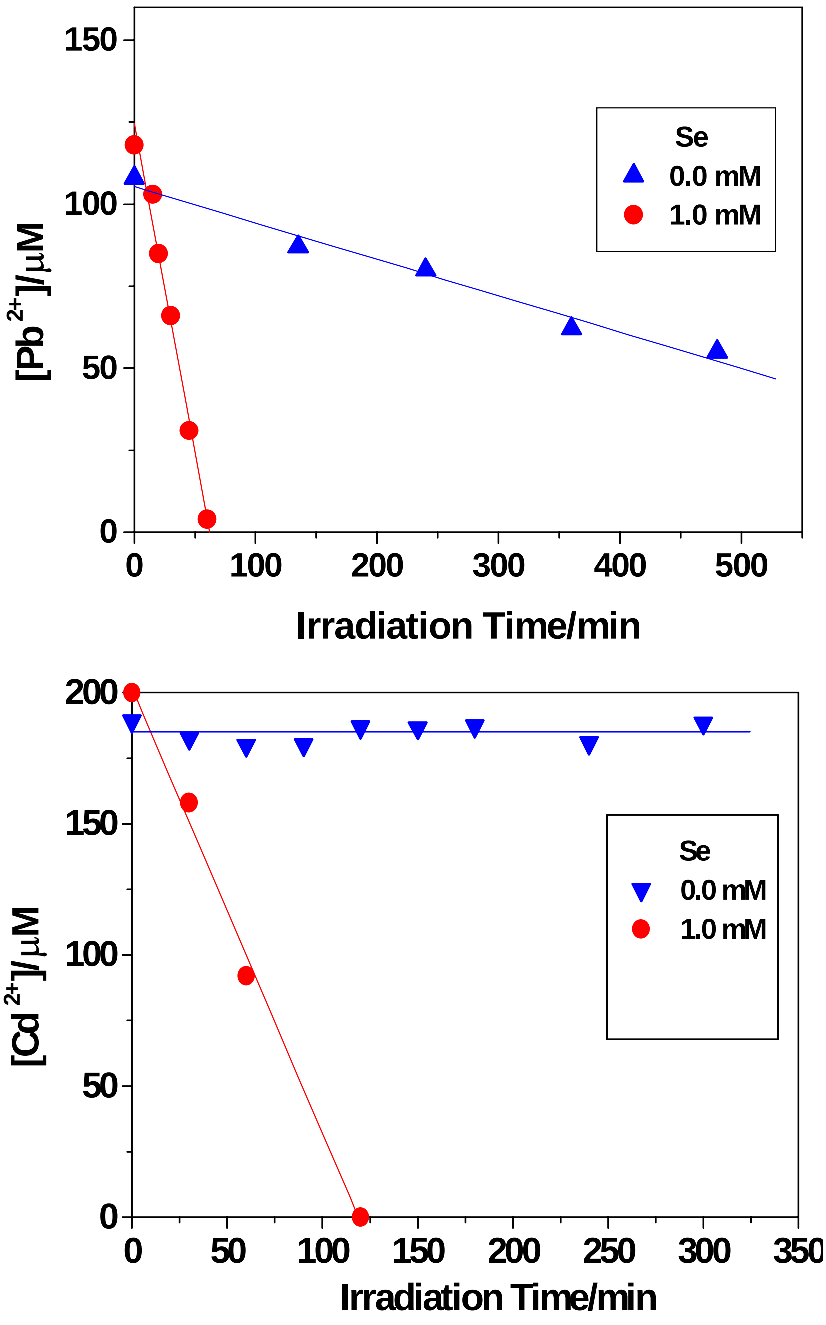

Figure 3.5: (a) Photocatalytic reduction of 200 μM Pb(II) in N_2-purged TiO_2 suspensions (2 g/L TiO_2 dose) under UV irradiation. In the 1.0 mM Se case, the TiO_2 suspension containing 1.0 mM Se(IV) species was pre-irradiated for 30 min before it was dosed with 200 μM Pb(II) species. (b) As in frame (a) but for the photocatalytic reduction of 200 μM Cd(II) species. See experimental section for details. The lines are least-squares fits of the data points.

The above two examples comprising of the Cd-Se and Pb-Se systems (and elaborated further by equations 3.11 and 3.12) represent good test cases of situations where the thermodynamic predictions and the observed kinetics trends are entirely in accord with one another. Note that the faster photoreduction in the Pb-Se case (Figure 3.5b) is consistent with the larger driving force for the $Pb^{2+}/PbSe$ redox case relative to the $Cd^{2+}/CdSe$ (Figure 3.5a) counterpart.

$$Se + M^{2+} + 2e^{-} \xrightarrow[h\nu]{TiO_2} MSe_{(TiO2)} \text{ (M = Cd, Pb)} \qquad (3.11)$$

$$M^{2+} + 2e^{-} \xrightarrow[h\nu]{TiO_2} M_{(TiO2)} \text{ (unfavorable)} \qquad (3.12)$$

The "TiO_2" (or "Se") subscripts within parentheses in equations. 3.11 and 3.12 (and in the other equations below) denote the parent phase where the participating species are located. What about the mechanism of MSe formation on the TiO_2 surface? Either an "ionic" (equations 3.13,3.14, and 3.17) or "atomic" (equations 3.15-3.17) pathway can be envisioned:

<u>Ionic</u>

$$Se_{(TiO2)} + 2e^{-}_{(TiO2\text{ or }Se)} \longrightarrow Se^{2-}_{(TiO2)} \qquad (3.13)$$

$$M^{2+}_{(aq)} + Se^{2-}_{(TiO2)} \longrightarrow MSe_{(TiO2)} \qquad (3.14)$$

<u>Atomic</u>

$$M^{2+}_{(aq)} + 2e^{-}_{(TiO2)} \longrightarrow M_{(TiO2)} \qquad (3.15)$$

$$M_{(TiO2)} + Se_{(TiO2)} \longrightarrow MSe_{(TiO2)} \qquad (3.16)$$

Overall

$$M^{2+}_{(aq)} + Se_{(TiO2)} + 2e^{-} \longrightarrow MSe_{(TiO2)} \qquad (3.17)$$

Chronopotentiometry (CP) experiments[104] were designed to address this aspect and are presented next.

3.2.2 Chronopotentiometry Probes of Se Deposition and MSe Formation on the TiO₂ Surface

In these experiments, the potential of the TiO_2 film substrate (versus a suitable reference electrode) is monitored in the dark and when the excitation light is turned on. Charge accumulation and transfer processes at the TiO_2 film/solution interface subsequently influence the temporal evolution of the TiO_2 film potential as elaborated elsewhere.[104] Figure 3.6 contains representative data; CP profiles during Se(IV) photoreduction and in a control run where the Se(IV) species were omitted from the supporting electrolyte (0.05 M Na_2SO_4), are compared and contrasted. In the control run, the potential moves in the negative direction when light is turned on. This is consistent with the accumulation of photogenerated electrons on the TiO_2 surface, i.e., the interface undergoes charging much like in a capacitor.[104] Subsequently, these electrons are trapped in surface sites and the potential relaxes back to a stable plateau around -0.1 V. Note that there are no intentionally added redox species in the electrolyte to scavenge the photogenerated electrons in this case. Protons are present in the electrolyte, albeit at very low concentrations; however, the TiO_2 surface is not intrinsically catalytic toward proton reduction.[14, 15]

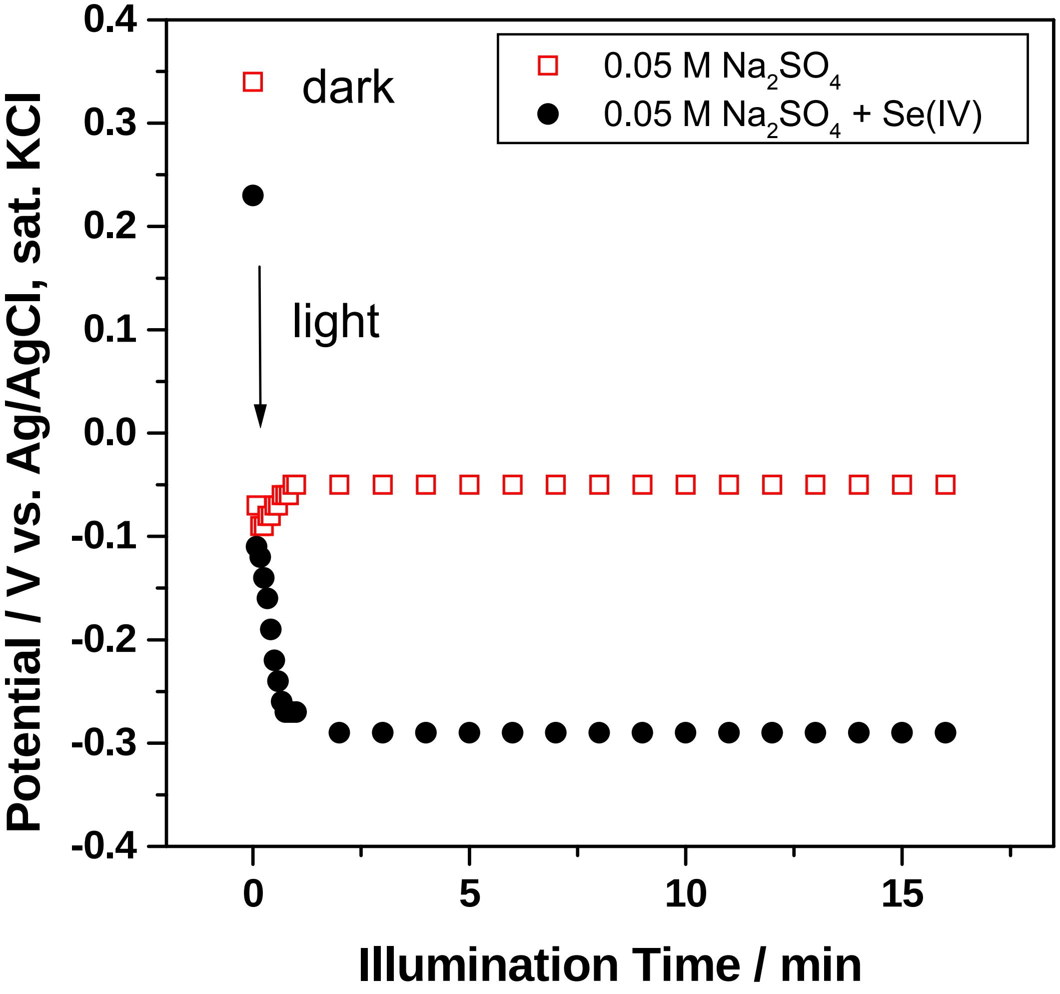

Figure 3.6: Chronopotentiometric (CP) profiles for a UV-irradiated TiO_2 film electrode in contact with 0.05 M Na_2SO_4 supporting electrolyte with and without added Se(IV) (at 200 μM level) species.

When Se(IV) species are present in the electrolyte, the TiO_2 film potential is pinned at ~ -0.30 V (Figure 3.6). Interestingly, this potential is located in the range of the $Se^{0/2-}$ redox potential (Figure 3.4). This is strong support for the ionic mechanism (see equation 3.13 above). Further support is furnished by the linear sweep photovoltammetry data to be presented below. That Se(IV) reduction proceeds beyond the initial $4e^-$ step (leading to elemental Se) is also suggested by the work of another group.[111] These authors have invoked a p-n junction model for the TiO_2/Se interface that explicitly considers the p-type semiconductor nature of Se and the consequent ease of its further photoreduction (to Se^{2-}).[111]

Figure 3.7 contains further CP data on the Cd-Se system. Two of the CP profiles are reproduced here from Figure 3.6 for direct comparison. Also shown are two control runs where the 0.05 M Na_2SO_4 supporting electrolyte was dosed with Cd(II) species. These data are virtually superimposable on the blank run reaffirming the lack of redox activity of Cd(II) species with the UV-irradiated TiO_2 surface (c.f., Figure 3.5a). On the other hand, when the Cd(II) species are dosed into the electrolyte in contact with a Se-modified TiO_2 surface, the CP profile is markedly different (inverted triangles, Figure 3.6). The potential is still pinned in the negative regime but there is a small, but reproducible positive shift of the plateau potential relative to the Se(IV) case (c.f., the two sets of data marked by normal and inverted triangles in Figure 3.7). This positive shift is a direct, experimental manifestation of the "underpotential" effect discussed earlier related to the ability of Cd(II) species to exchange charge with the Se-modified TiO_2 surface.

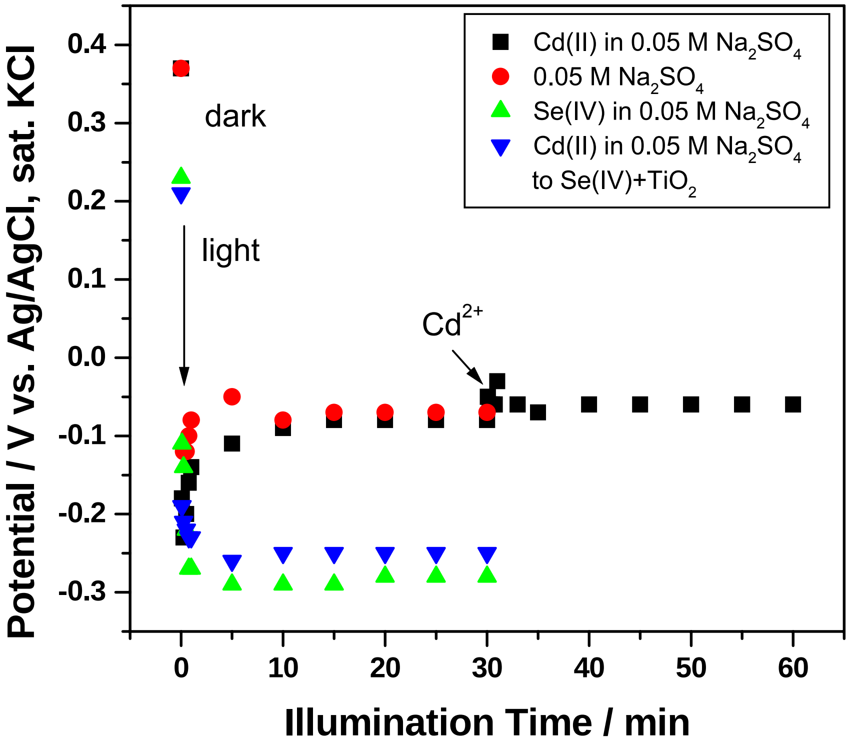

Figure 3.7: CP profiles for experiments involving Cd(II) species. The two sets of data from Figure 3.6 (triangles and circles) are reproduced here for direct comparison. Additionally, a control run for Cd(II) species in 0.05 M Na_2SO_4 is shown (squares). In another control run, Cd(II) species were dosed (at 200 μM level) into the 0.05 M Na_2SO_4 electrolyte after 30 min of irradiation (indicated by the arrow in Figure 3.7). In the fifth experiment, Cd(II) species were added (at 200 μM level) at the inception of the run and the TiO_2 film was pre-modified with Se (see text).

Figure 3.8 contains CP profiles for the Pb-Se system. The supporting electrolyte was switched from Na_2SO_4 to NaCl because of the limited solubility of Pb^{2+} ions in the former case. The data represented by open circles and closed squares upto 30 min are for the control cases where the photogenerated electrons in TiO_2 are simply trapped by the surface sites. Consider the CP profile represented by the open circles first. When Pb(II) species are dosed in, the potential immediately shifts in the positive direction and attains a new plateau around ~0.05 V. Recall that Pb^{2+} ions are capable of exchanging charge (i.e., being photoreduced) by UV-irradiated TiO_2 (c.f., Figure 3.5b).

On the other hand, when Se(IV) species are dosed in at 30 min (filled squares, Figure 3.8), the potential shifts in the negative direction as before (c.f., Figures 3.6 and 3.7). Now when Pb^{2+} ions are also additionally dosed in after 60 min, the TiO_2 film potential undergoes a marked positive shift signaling Pb^{2+} reduction and Pb-Se compound formation. Note that the extent of this shift far exceeds the case where Se species are absent at the TiO_2/electrolyte interface. The shift is also much more pronounced relative to the Cd-Se system (c.f., Figures 3.7 and 3.8). All these trends are consistent with the relative thermodynamic driving forces (Figure 3.4) and the faster kinetics in the Pb-Se system relative to the Cd-Se counterpart (c.f., bottom sets of data in Figures 3.5a and b).

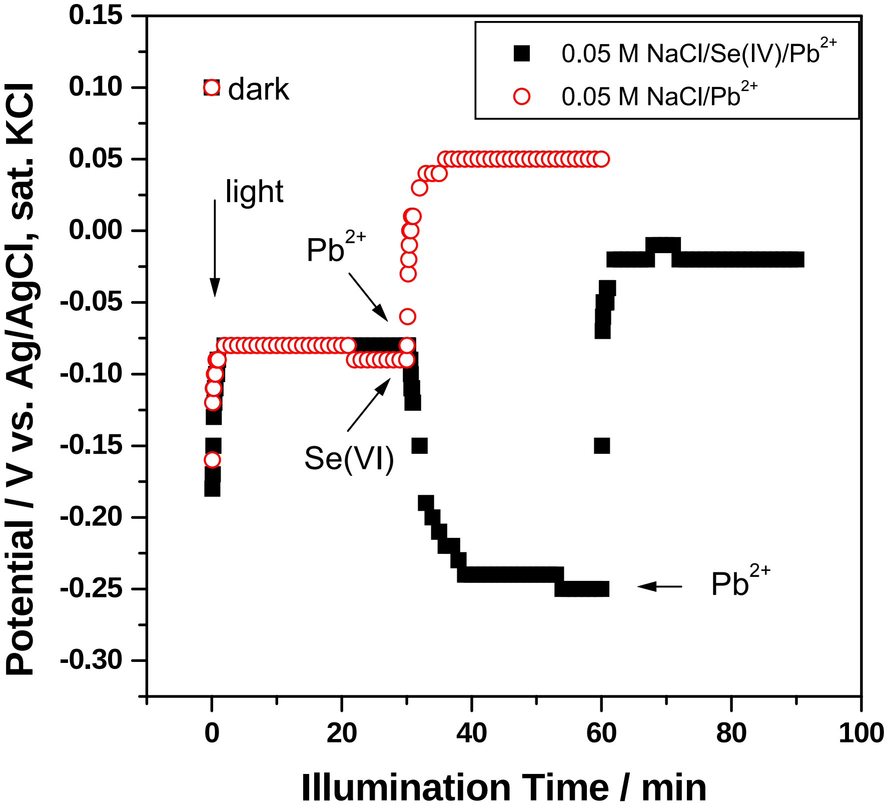

Figure 3.8: As in Figure 3.7 but for Pb(II) species. The supporting electrolyte was 0.05 M NaCl instead of 0.05 M Na_2SO_4. The data upto 30 min are from two identical runs and illustrate the degree of reproducibility in the CP profiles. At 30 min (open circles), Pb(II) species were dosed in (at 200 μM level). Similarly, in the other experiment (data denoted by closed squares), Se(IV) species were dosed in at 30 min (at 200 μM level) and Pb^{2+} species at 60 min (at 200 μM level).

3.2.3 Linear Sweep Photovoltammetry Using Visible Light Excitation of Se- and CdSe- Modified TiO_2 Electrodes

In linear sweep photovoltammetry, interrupted photoexcitation of a (semiconductor) electrode is employed during a slow (e.g., 2 mV/s) potential sweep.[109,112,113] Thus the current-potential profile can be mapped in the same experiment for a given electrode material both in the dark and under electrode illumination. N-type semiconductors exhibit photo-enhancement of current in the anodic direction while the opposite trend (photocathodic current flow) holds for p-type semiconductors. Figure 3.9 contains linear sweep photovoltammogram (LPV) traces for a Se-modified TiO_2 film (Figure 3.9a) and a CdSe/TiO_2 film counterpart (Figure 3.9b). Cartoons of the electrode morphologies in the two cases are also depicted in these figures. Visible light photoexcitation was employed so that the contribution from the underlying TiO_2 substrate could be minimized. (Recall that the optical bandgap of Se and CdSe are much smaller than that of TiO_2, Ref. 113).

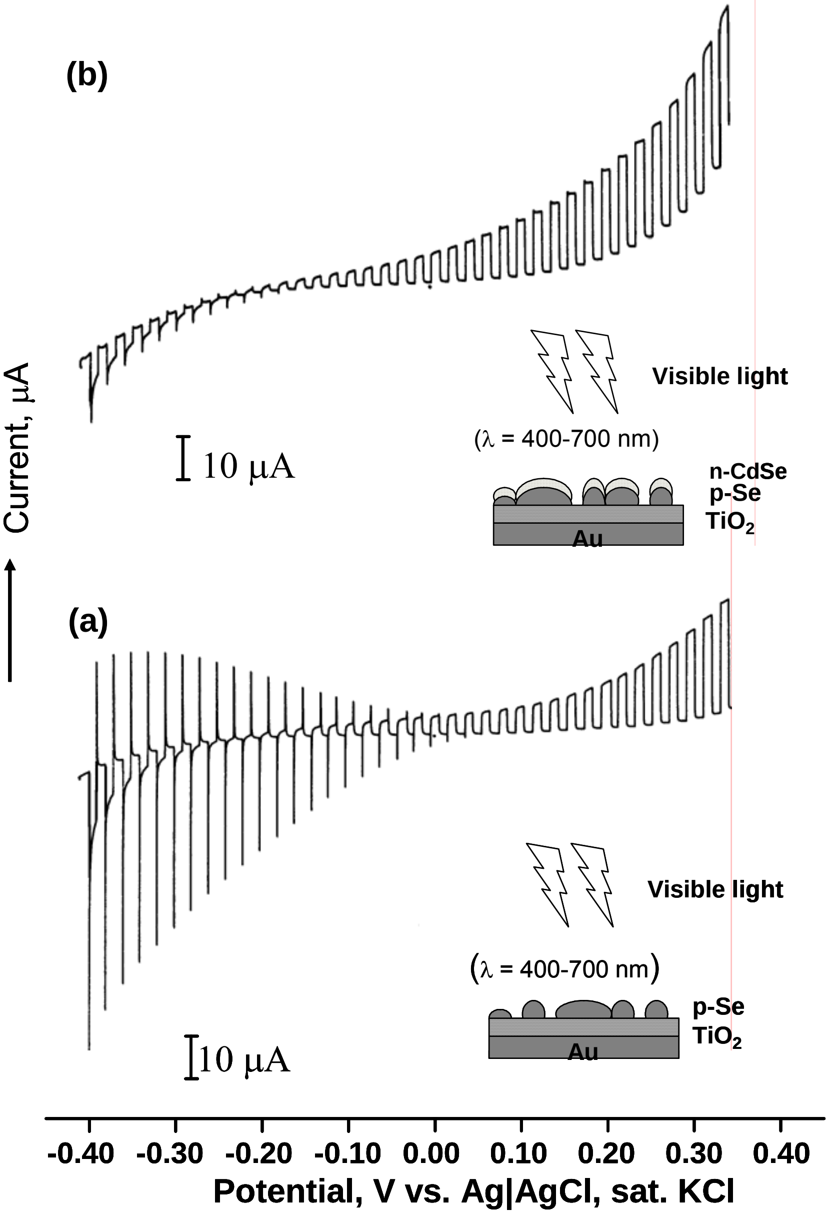

Figure 3.9: Linear sweep photovoltammograms in 0.5 M Na_2SO_4 for (a) Se-modified TiO_2 film and (b) CdSe- and Se- modified TiO_2 film (see text). The potential scan rate was 2 mV/s and the geometric area of the film was 0.8 cm^2. Visible light irradiation was employed unlike in the experiments in Figures 3.5-3.8 above.

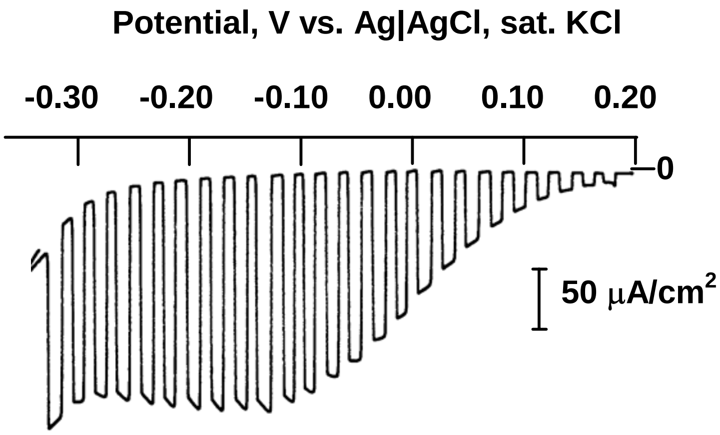

Figure 3.10: Photovoltammogram for an electrodeposited Se^0 film in 0.5 M H_2SO_4. The Se film was grown on a gold surface by polarizing for 15 min at -0.7 V (vs. Ag|AgCl) in a solution containing 10 mM SeO_2 in 0.1 M Na_2SO_4. Other conditions are as in Figure 3.9.

When the potential is swept in the positive direction from a negative value (~ -0.40 V) (see Figure 3.9a), the p-type Se sites on the TiO_2 surface (separate microscopy data reveal that the Se phase does not form a continuous layer on the TiO_2 surface) are under reverse bias. Thus after photoexcitation of electron-hole pairs in Se, the electrons are driven by the electric field to the solution interface. There these carriers can participate in photocathodic processes, namely, the reduction of Se itself (c.f., Figure 3.6), protons, or even adventitious dissolved O_2 in the contacting electrolyte. The spikes seen especially in Figure 3.9a are diagnostic of facile carrier recombination. That the Se layer formed from the reduction of Se(IV) species acts as a p-type semiconductor is demonstrated by the LPV data in Figure 3.10. The photocathodic enhancement of current flow as the potential is swept negative past the flatband potential at ~0.2 V (reverse bias regime for a p-type semiconductor), Figure

3.10, is diagnostic of p-type semiconductor behavior.[109] Past a potential of ~ -0.10 V in the other direction (see Figure 3.9a), the imposed potential manifests as a reverse bias across the (underlying) TiO_2 regions. This results in photoanodic current flow resulting from the movement of photogenerated holes in TiO_2 across the interface and their participation in either the oxidation of hydroxyl groups on the oxide surface or of bulk water molecules.

As elaborated elsewhere,[114] a Se/TiO_2 p-n junction[111] can be electrically modeled in terms of two diodes connected in series. The onset potential for photocurrent flow is then pinned at an "offset potential" that is defined by the flatband potentials of n-TiO_2 and p-Se respectively, -0.45 V and +0.20 V, i.e., at -0.25 V. [These flatband potentials may be estimated from the onset potentials in the photovoltammograms for n-TiO_2 and p-Se films respectively]. Interestingly, note that this potential, -0.25 V, is very close to the plateau potential attained in the CP experiments, c.f., Figure 3.6. This offset potential is also very close to the location in the LPV profiles where the cathodic and anodic components balance one another, c.f., Figure 3.9.

Most significantly, on a p-Se film on gold substrates (Figure 3.10), the photopotential attained is not negative enough to drive the $Se^0 \rightarrow Se^{2-}$ cathodic process, and thus MSe formation is precluded on an irradiated p-Se/Au electrode at open circuit.[114] These findings furnish additional evidence in support of the ionic mechanism for MSe compound formation on the irradiated TiO_2 surface.

When the Se sites are partially converted to CdSe, two trends in the LPV profiles are striking (Figure 3.9b). First, the photocathodic envelope is much diminished in amplitude (relative to that in Figure 3.9a) because of the conversion of many of the surface p-type Se sites to n-CdSe. Second, the photoanodic portion is somewhat amplified because now both n-CdSe and n-TiO_2 respond to visible photoexcitation unlike the case in Figure 3.9a where only n-TiO_2 is present.

Bipolar LPV profiles (i.e., photovoltammograms exhibiting photocathodic and photoanodic behavior in the same trace) such as those in Figure 3.9 are not commonplace in the semiconductor electrochemistry literature.[115,116] This interesting behavior is possible in the composite semiconductor structures such as those considered in Figure 3.9 because the n-type and p-type semiconductor regions can be separately accessed by the electrolyte. In fact, in the structure in Figure 3.6b, one p-type semiconductor (Se) is in electronic contact with two n-type semiconductor (TiO_2 and CdSe) components reminiscent of an n-p-n (transistor-like) configuration.

3.2.4 Ex Situ Characterization of Se- and CdSe- Modified TiO_2 Surfaces

Figure 3.11 contains representative electron probe microanalysis (EPMA) elemental maps for Cd (Figure 3.11a) and Se (Figure 3.11b) for a CdSe/TiO_2 film with the morphology schematized as an insert in Figure 3.9b; i.e., the film has a CdSe/Se/TiO_2 configuration.

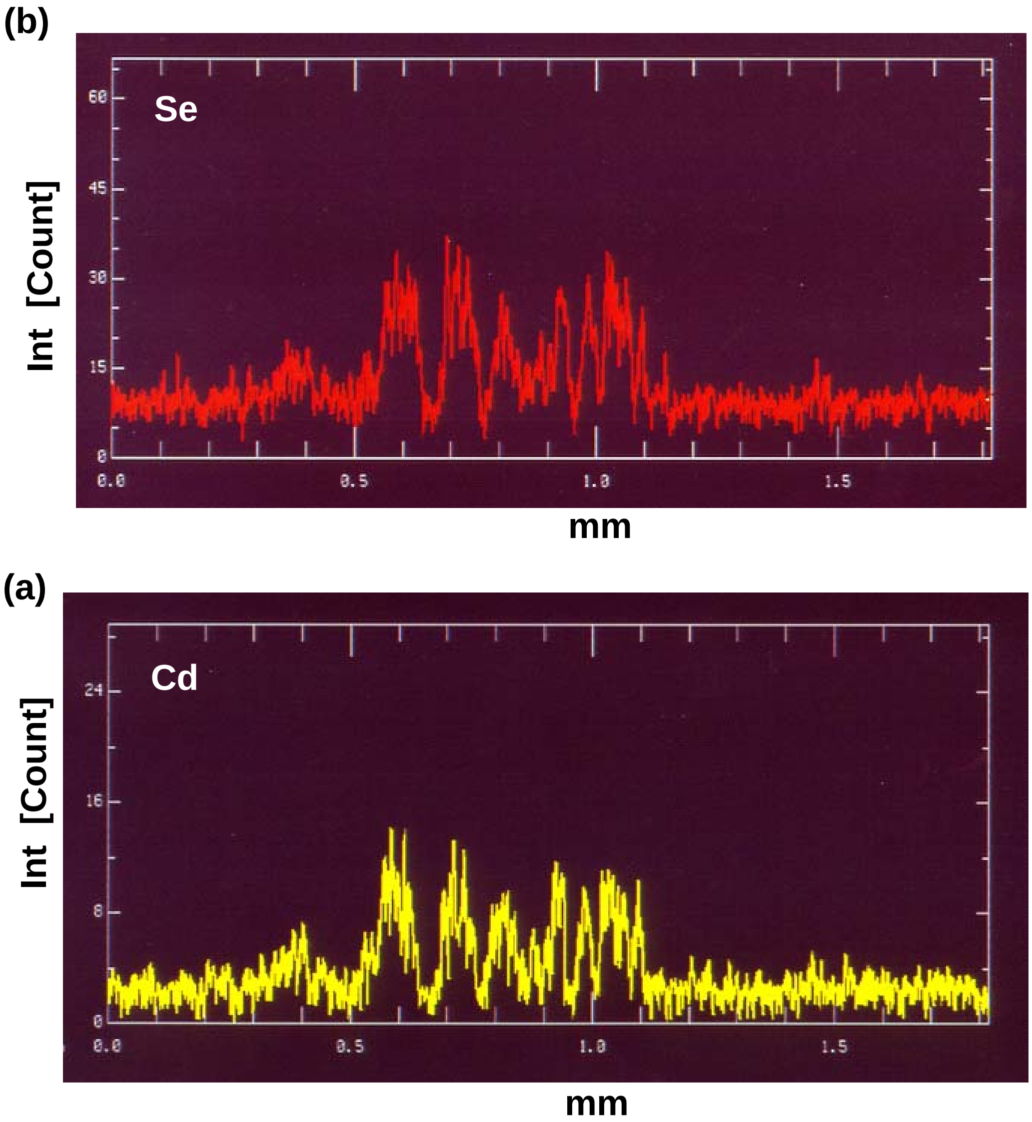

Figure 3.11: Representative EPMA elemental map for a sample as in Figures 3.9b and 3.10. A mask was used to delineate the areas on the TiO_2 surface for Se and CdSe deposition (see text). The analytical electron beam was then rastered across these selected spots, one example each of which, is shown in the profiles in Figure 3.11. (Courtesy : Prof. R. Shiratsuchi, Kyushu Institute of Technology Japan)

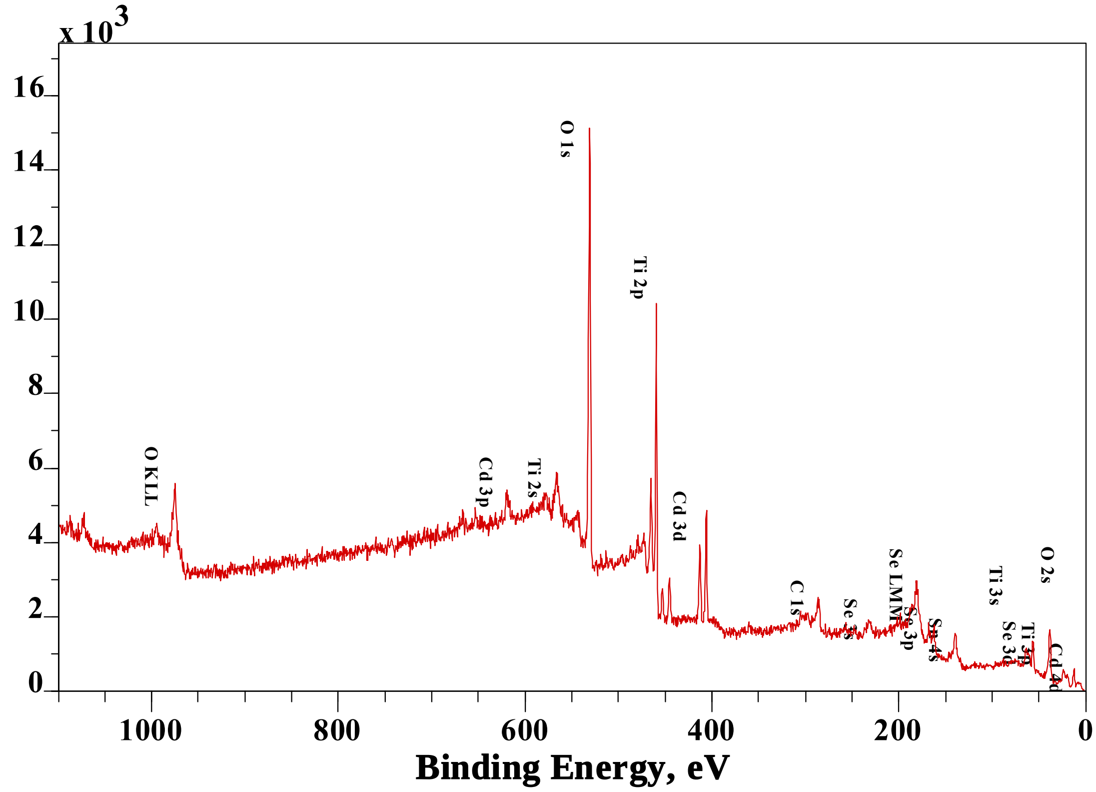

Figure 3.12: Survey XPS scan for a sample as in Figure 3.9b.

A custom-made mask containing 0.7 mm diameter holes was used on top of the TiO_2 surface to delineate the regions for Se and CdSe deposition. Significantly, the spatial distribution of the two elements on the parent TiO_2 is highly correlated, the Cd signals mimicking their Se counterparts in Figure 3.11. This is yet another strong piece of evidence for the underpotential deposition model considered earlier; namely, that Cd deposition is induced by the Se "template".

Figure 3.12 contains a survey XPS spectrum of a sample very similar to that considered above in Figures 3.9b and 3.11. Aside from the (expected) TiO_2 signals, peaks assignable to both Cd and Se are clearly seen. High-resolution XPS data provide further support for the chemical composition of both the MSe/TiO_2 composites. The PbSe/TiO_2 sample gave a Pb $4f_{7/2}$ binding energy value of 138.2 eV compared with 138.3 eV for an authentic sample of PbSe.[117] The Se 3d binding energy value in PbSe/TiO_2 was 54.3 eV versus 53.9 eV for the authentic sample of PbSe. Values of 405.3 eV for Cd $3d_{5/2}$ and 55.2 eV for Se 3d were obtained for CdSe/TiO_2 compared to 405.7 eV and 54.9 eV respectively for an authentic sample of CdSe.[117] For comparison, the 3d binding energy in elemental Se is 55.5 eV for an authentic sample of Se.[11]

3.3 Occlusion Electrosynthesis of WO_3-TiO_2 Composite Films

As elaborated elsewhere, occlusion electrodeposition is a versatile method for preparing composite films where targeted particles (Degussa P 25 TiO_2 in the present study) can be dispersed in a matrix such as WO_3.[60,118.119] The matrix component is electrosynthesized and in the process of its growth, assimilates the suspended particles

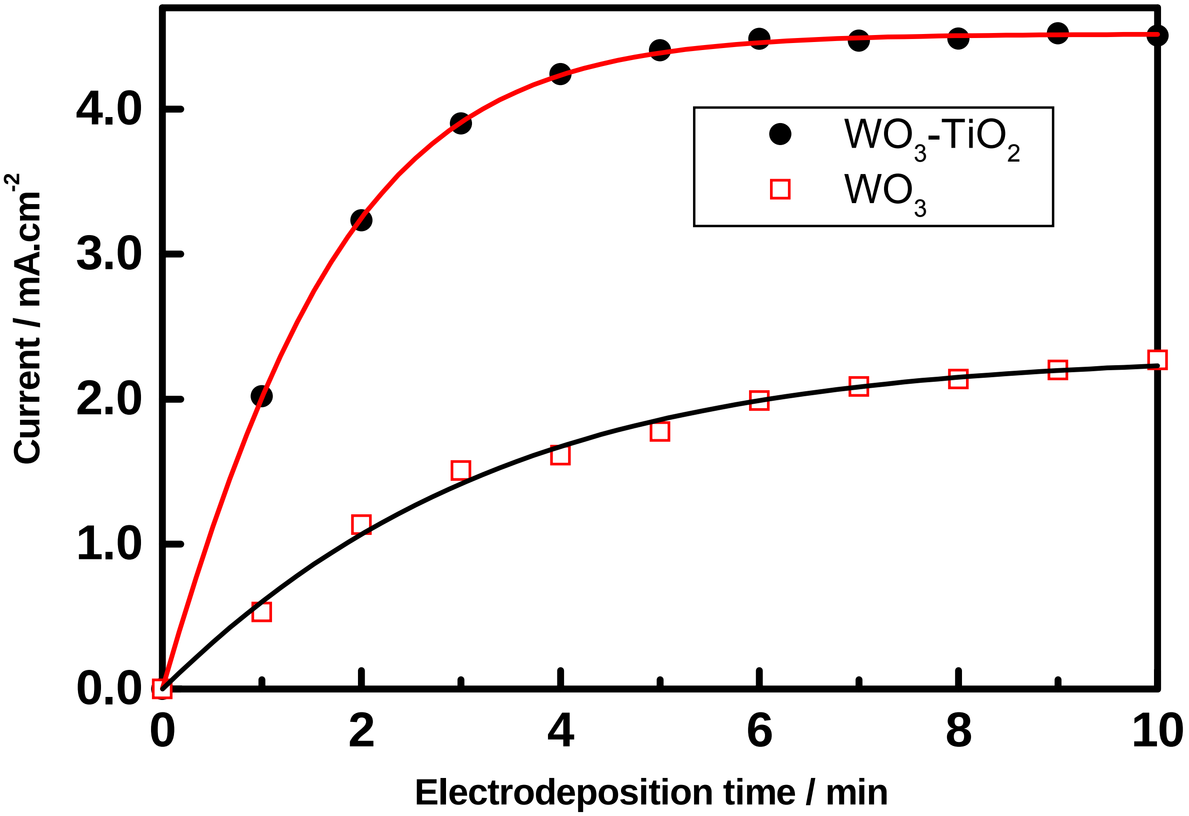

Figure 3.13**:** Effect of TiO_2 particle dose in the deposition bath on the current–time profiles: TiO_2 dose = 0 (—□—) and 0.64 mg/mL (—●—).

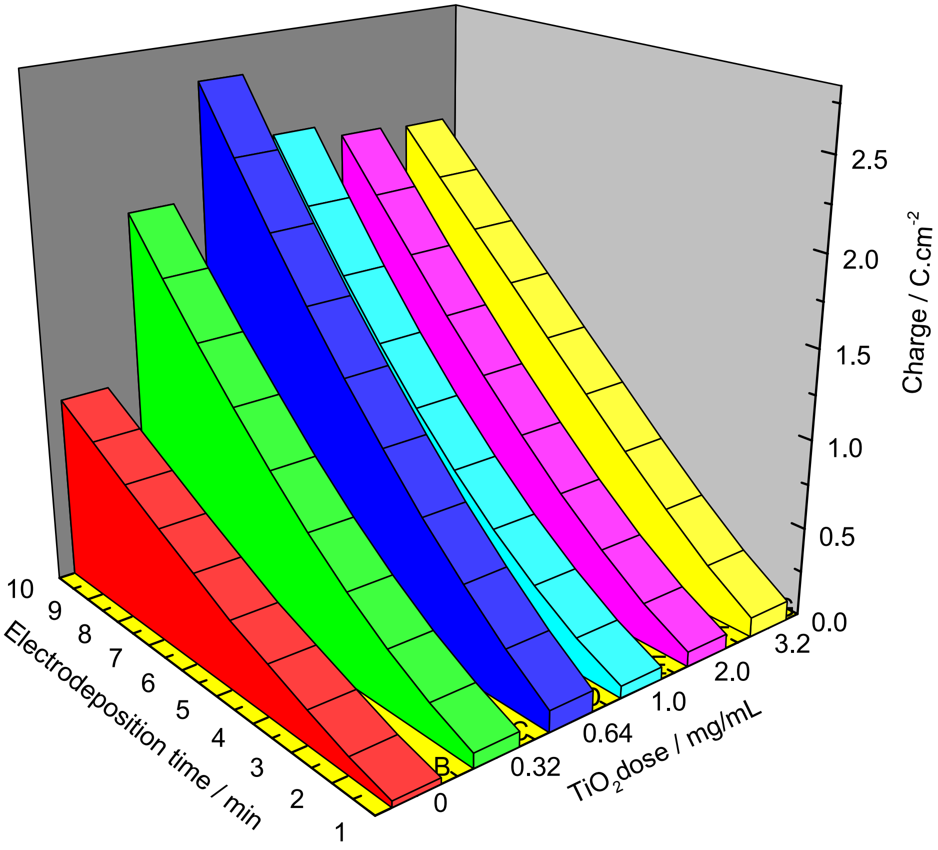

Figure 3.14: 3-D plot of the WO_3 deposition charge as a function of time for TiO_2 particle doses varying between 0.32 and 3.2 mg/mL.

in the deposition bath. The deposition process, and thus the measured electrodeposition charge, corresponds to the reaction:[53,120]

$$2W_2O_{11}^{2-} \ + \ 8H^+ \ \ 4e^- \longrightarrow 4WO_3 \ + \ 3O_2 \ + \ 4H_2O \qquad (3.18)$$

Figures 3.13 and 3.14 contain data which show how the deposition current (Figure 3.13) or the charge (Figure 3.14) is dependent on the two variables, namely, time and the particle dose in the bath. High particle doses clearly impede film growth, and a dose of 0.64 mg/mL appears to be optimal (Figure 3.14). Therefore the data below pertain mostly to composite films generated from a 0.64 mg/mL dosed bath. These films have a WO_3:TiO_2 surface composition of 89:11 (atom percent) as assayed by X-ray photoelectron spectroscopy (XPS).

3.3.1 Calcination and Raman Spectroscopic Monitoring of the Anatase-to-Rutile Conversion

X-ray diffraction has been deployed in many of the previous studies for monitoring the effect of calcination of TiO_2.[121, 122, 123] Other techniques include measurement of the surface area, electron microscopy, and photoconductance.[123, 124, 125] Among optical spectroscopy candidates, infra-red spectroscopy (specifically FT-IR) has proved to be useful for mapping the state of surface hydroxylation of the oxide as a function of the calcination temperature.[122] The extent of conversion of anatase to rutile when the TiO_2 samples were pre-calcined at various temperatures in the 450-800 ^{0}C range was studied by our group using laser Raman spectroscopy.[126] Figure 3.15 contains the data; Figure 3.15a shows the Raman spectra and Figure 3.15b maps the % conversion

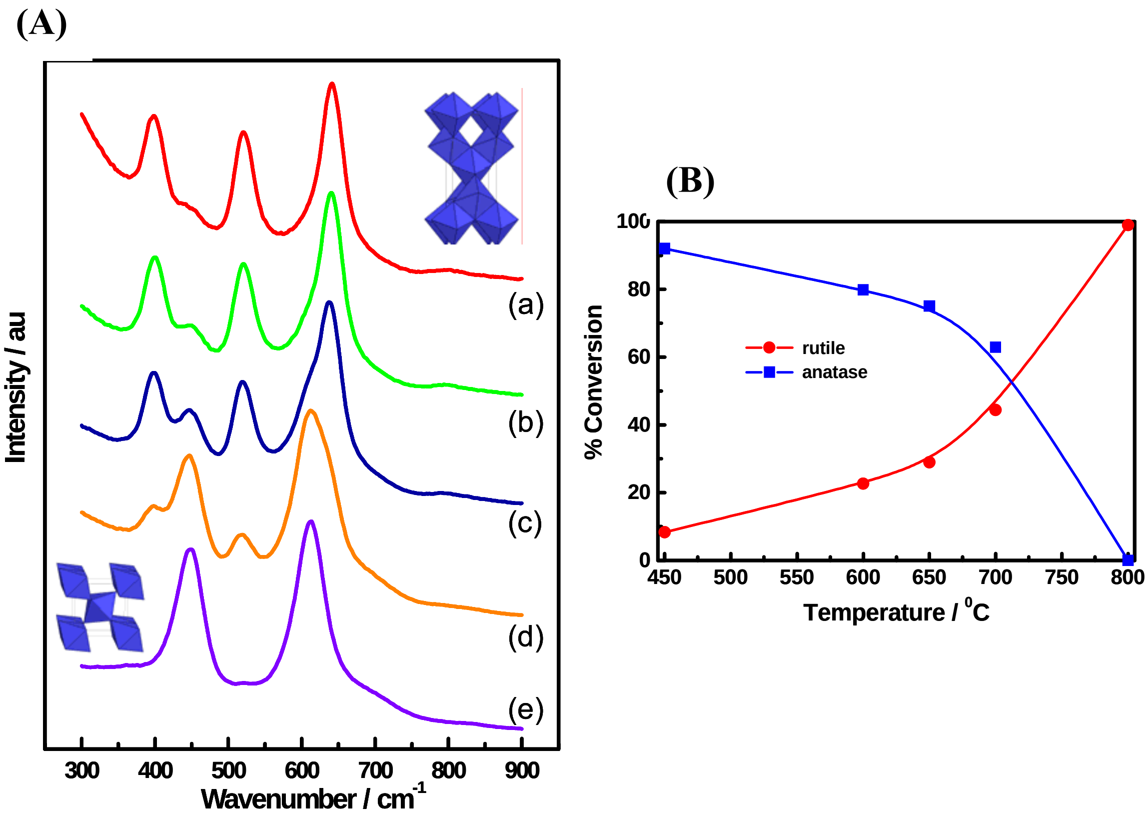

Figure 3.15: (A) Raman spectra of P 25 TiO_2 particles after being subjected to pre-calcination at 450 ^{0}C (a), 600 ^{0}C (b), 650 ^{0}C (c), 700 ^{0}C (d), and 800 ^{0}C (e). Schematic crystallographic structures of anatase (top right) and rutile (bottom left) are also shown. (B) Temperature dependence of the % composition (anatase and rutile) as obtained by deconvolution of the corresponding Raman bands for each structure and measuring their area. (Courtesy: Prof. Norma R. de Tacconi, University of Texas at Arlington)

(anatase→ rutile) as a function of the calcination temperature. The latter parameter was obtained from deconvolution of the characteristic Raman bands for each phase: 385, 512, and 645 cm^{-1} for anatase and 447 and 612 cm^{-1} for rutile respectively.[127,128] In essential agreement with previous studies,[123,129] the conversion to rutile becomes significant at temperatures higher than ~ 700 ^{0}C and at 800 ^{0}C, all of the anatase is converted to the rutile phase (Figure 3.15b).

3.3.2 Photoelectrochemical Behavior

Figure 3.16 contains photovoltammograms for an electrosynthesized WO_3 film (Figure 3.16a) and a similar composite film containing occluded TiO_2 particles (Figure 3.16b). These photovoltammetry scans were obtained using a slow potential sweep (2 mV/s) in conjunction with interrupted irradiation of the semiconductor film. The data pertain to 0.5 M Na_2SO_4 supporting electrolyte. The following trends are worthy of note: (a) the dark currents are negligible in both cases in Figure 3.16 over the potential range from ~ -0.3 V to ~ 1.4 V. (b) Both types of samples show the "normal" S-shaped voltammogram morphology. (c) The anodic photocurrents are higher for the composite film than for its WO_3 parent (c.f., Figures 3.16a and b). (d) The photocurrent onset potential is more negative for the composite film than for WO_3 (c.f., Figures 3.16a and b).

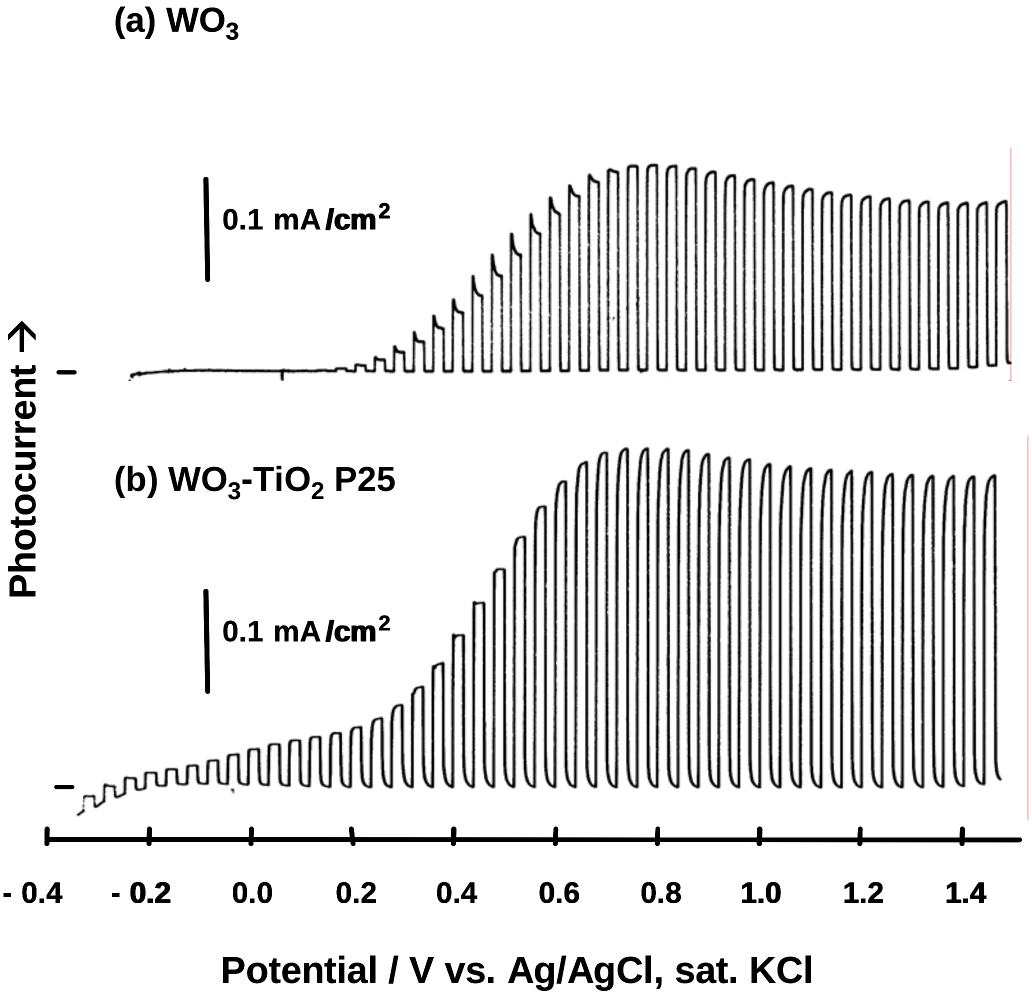

Figure 3.16: Effect of the occluded TiO_2 particles on the photoelectrochemical behavior of a WO_3 film, (a) without, and (b) with 11% of P 25 TiO_2 (pre-calcined at 450 °C). A deposition time of 10 min was used for both films. Photovoltammograms were obtained at 2 mV/s using 0.1 Hz chopped irradiation from the full output of a 75 W Xe lamp and in 0.5 M Na_2SO_4.

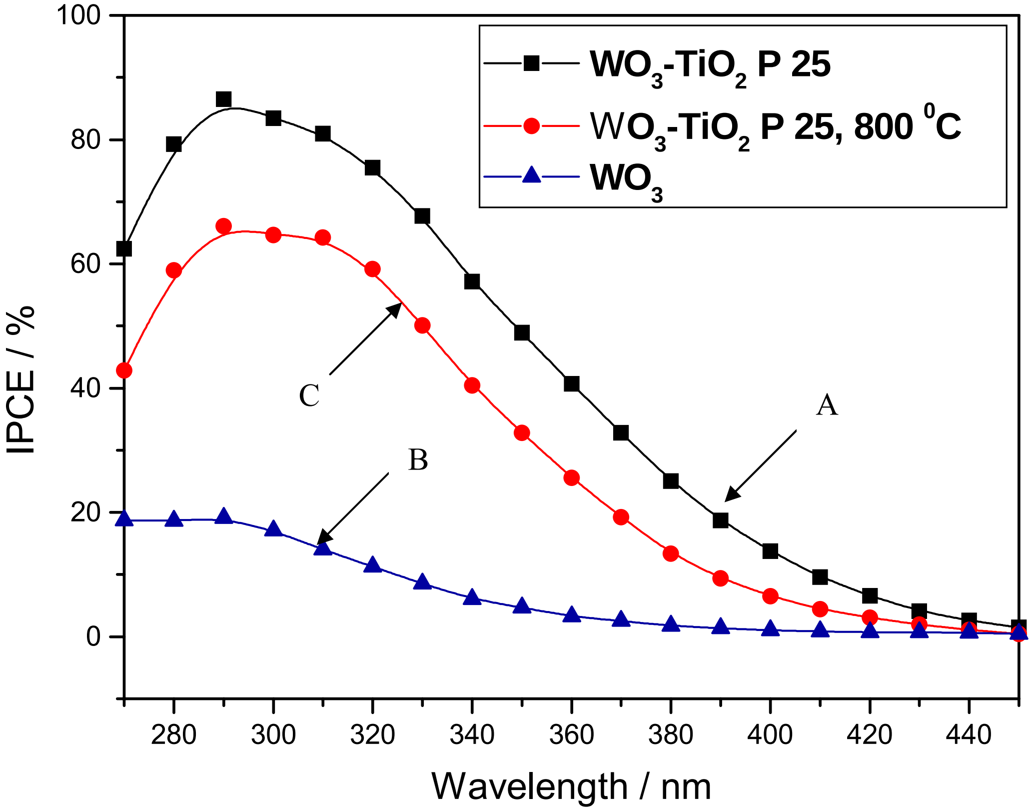

Figure 3.17: Photoaction spectra of WO_3-TiO_2 composite films containing particles pre-calcined at 450 °C and 800 °C. Electrolyte: 0.5 M Na_2SO_4 + 0.1 M HCOONa. Both films were electrodeposited during 10 min from a bath containing 1.0 mg/mL (a) and 2.0 mg/mL (b) of TiO_2. The photoaction spectrum 2.0 for a WO_3 matrix without TiO_2 particles is also 3.0 included for comparison.

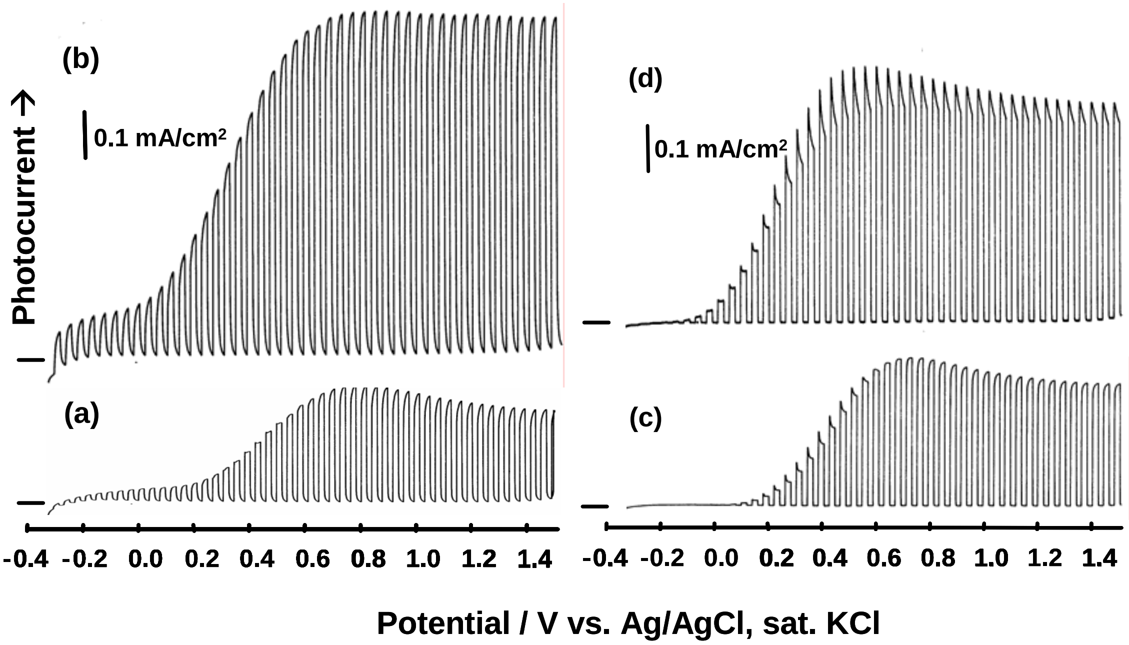

Figure 3.18: Photovoltammograms for WO_3-TiO_2 composite films with the TiO_2 particles pre-calcined at 450 °C ((a) and (b)) and at 800 °C ((c) and (d)) in 0.5 M Na_2SO_4 ((a) and (c)) and in 0.5 M Na_2SO_4 + 0.1 M HCOONa ((b) and (d)). Both films were prepared using a TiO_2 dose of 0.64 mg/mL in the WO_3 electrodeposition bath. Scan and irradiation details as in Figure 3.16.

That the composite films are superior in photoelectrochemical activity to the WO_3 counterpart is also borne out by the photoaction spectra in Figure 3.17. These data unlike those in Figure 3.16 pertain to the supporting electrolyte containing also an electron donor, namely, formate. Thus the photogenerated holes in the composite films show significantly better kinetics for oxidizing both water (Figure 3.16) and an organic compound (Figure 3.17 [A,B]) relative to their performance in a neat WO_3 matrix.

Another interesting aspect of the photoelectrochemical behavior concerns the selectivity of the composite films toward oxidation of water and organic compounds and how that changes with their calcination history. Figure 3.18 contains photovoltammograms for both types of electron donors for a film pre-calcined at 450 ^{0}C (Figure 3.18a,b) and at 800 ^{0}C (Figure 3.18c,d). Interestingly enough, the rutile particles perform better for photooxidizing water than their anatase counterparts; the reverse trend holds for formate photooxidation. This trend can be quantified by comparing a photocurrent enhancement factor F[119, 130] for the two films. This factor is defined at a given potential (e.g., + 0.7 V) by the ratio of the photocurrents for formate oxidation and water photooxidation respectively[119, 130] i.e.:

$$F = \frac{i_{ph}\,(H_2O + HCOONa)}{i_{ph}\,(H_2O)} \qquad (3.19)$$

Thus F is ~ 3 for the composite film containing anatase and is only ~ 1-2 for the composite film containing rutile (Table 3.4). Note that a lower value of F translates to better selectivity for oxidizing water and vice versa.

Figure 3.17 compares the photoaction spectra for two composite films (now with WO_3 as the matrix) with the P 25 TiO_2 particles pre-calcined at 450 ^{0}C (A) and 800 ^{0}C (C) respectively. As mentioned earlier, these data pertain to 0.5 M Na_2SO_4 containing the formate electron donor. In general, a diminution of the photoresponse is seen when the anatase particles are converted to rutile. Table 3.4 compares the incident photon to electron conversion efficiency (IPCE) values for the various samples:

$$F = j_{ph} / q\phi \qquad (3.20)$$

In equation 3.20, j_{ph} is the photocurrent density, q is the electronic charge, and ϕ is the incident photon flux on the cell.

A closer examination of the profiles in Figure 3.18 reveals that the photocurrent onset potential shifts to more positive values when the occluded particles are pre-calcined at 800 ^{0}C versus their counterparts at 450 ^{0}C (c.f., frames a, b with c, d in Figure 3.18). This is consistent with the notion that the photogenerated electrons have a higher energy in the anatase host than in the rutile phase (i.e., the flat-band potential is more negative for anatase than for the rutile TiO_2 phase).[131]

Table 3.4: Comparison of IPCE values[a] and photocurrent enhancement factors (F) for various samples[b]

Film	IPCE % [c] (H_2O)	IPCE % (HCOONa)	F [d]
WO_3	11	18	< 2
WO_3-TiO_2 P 25 (450 ^{0}C)	24	83	3-4
WO_3-TiO_2 P 25 (650 ^{0}C)	31	72	~ 3
WO_3-TiO_2 P 25 (800 ^{0}C)	48	65	1-2

[a] Values presented for IPCE are "peak" values occurring in the 300-320 nm wavelength range and are shown both for the photooxidation of water (second column) and formate species (third column).

[b] Data from Figures 3.17, 3.18 and 3.19

[c] See equation 3.20 in text.

[d] See equation 3.19 in text.

Figure 3.19 contains 3-D plots showing how the photocurrent (at a fixed potential, say 0.7 V) depends on both the TiO_2 particle dose in the deposition bath and on the electrodeposition charge. Data are shown for 450 ^{0}C (Fig. 3.19a), 650 ^{0}C (Figure 3.19b), and 800 ^{0}C (Figure 3.19c) pre-calcination temperatures. The data on the x-y plane, of course, are counterparts of Figure 3.13 but now for all three pre-calcination temperatures. Interestingly, the deposition charge is lower in the 800 ^{0}C case (Figure 3.19c) relative to the other two lower pre-calcination temperatures. (Figures 3.19a and b). This is undoubtedly a manifestation of the bulkier rutile particles that result from the anatase → rutile transformation.[132]

The highest photocurrents for the oxidation of water or formate are observed in the 0.6 – 1.0 mg/mL TiO_2 dose range for the 450 ^{0}C pre-calcination case (Figure 3.19a). This maximum shifts to a higher particle dose range (~ 3.0 mg/mL) when the particles in the composite film are pre-calcined at 800 ^{0}C (Figure 3.19c). Interestingly, the 650 ^{0}C (Figure 3.19c) pre-calcination case exhibits a bi-modal profile consistent with the TiO_2 particles having mixed anatase/rutile phase distribution (c.f., Figure 3.15).

XPS analyses reveal that the TiO_2 content of the WO_3-TiO_2 composite film also depends on the initial particle dose in the bath. Thus the 0.64 mg/mL dose results in a TiO_2 content of 11 atom % (Ti) while the 3.2 mg/mL dose affords a composite film with only 6-7 atom % (Ti). The trends in Figure 3.19 can be summarized as follows: (a) The TiO_2 particle dose for best PEC performance depends on the particular TiO_2 phase, being higher for rutile than for anatase. (b) The deposition charge is always higher in the presence of TiO_2 particles in the bath (see also Figure 3.14) but this charge increment diminishes as the particles are pre-calcined at higher temperatures (than ~ 450 ^{0}C). The composite films have improved ability to photooxidize water as the occluded particles are progressively converted to rutile; the reverse trend applies for photooxidation of an organic compound (e.g., sodium formate).

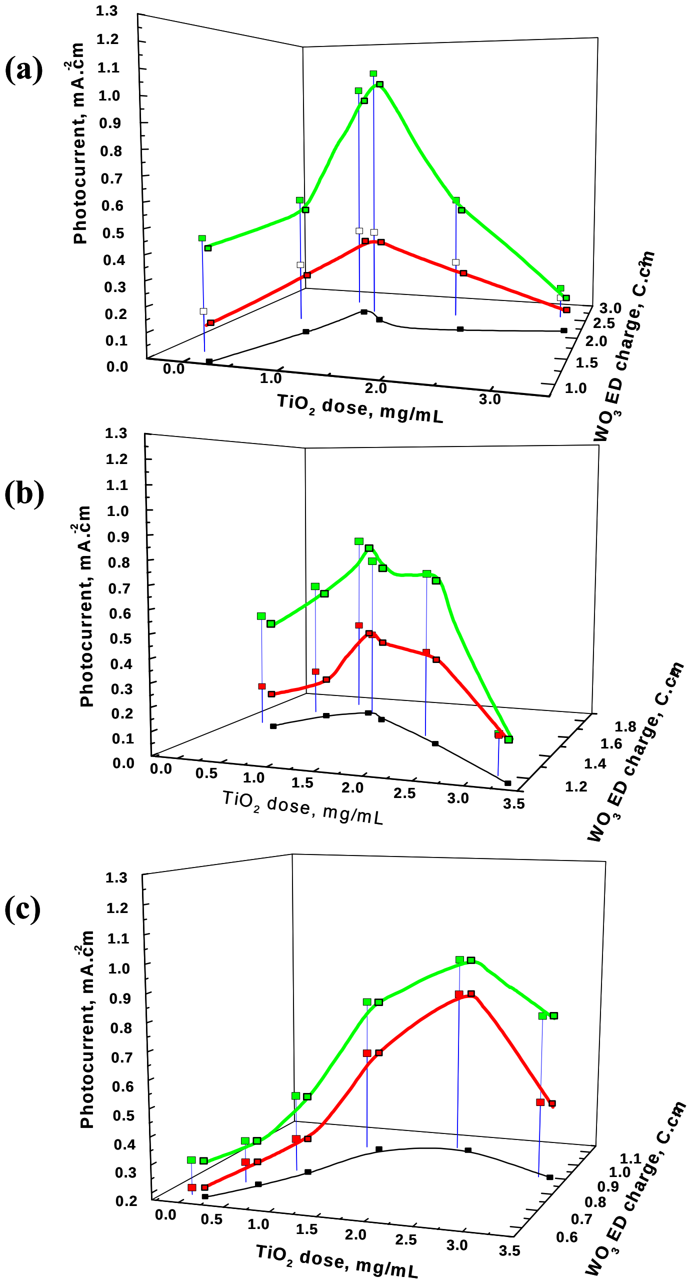

Figure 3.19: Photocurrent 3-D plots as a function of film preparation variables: WO_3 electrodeposition charge and TiO_2 particle dose. Electrolytes: 0.5 M Na_2SO_4 (red curves) and 0.5 M Na_2SO_4 + 0.1 M HCOONa (green curves). Plots (a), (b), and (c) are for pre-calcination temperatures of 450 °C, 650 °C, and 800 °C respectively. The photocurrent values were obtained from the photovoltammogram of each composite film at 0.7 V.

3.3.3 General Discussion

The above data hopefully illustrate that composite film architecture offers a versatile approach for probing the influence of prior history (e.g., thermal pre-treatment) on the photoelectrochemical behavior of the occluded semiconductor particles. We have specifically shown that depending on the calcination history (anatase vs. rutile), the composite film can be tuned for photooxidizing either water or organic additives. The finding that rutile performs better than anatase particles for photooxidation of water has literature precedence in studies on TiO_2 powders.[133, 134] Other than morphology and particle size related factors (recall that rutile particles are larger than their anatase parents, c.f., Ref. 132), this trend is mostly probably rooted in the titania surface-OH groups and their evolution with thermal history. It has been reported that the activity of TiO_2 for oxygen evolution is increased several-fold when these groups are removed by thermal treatment.[129] Surface peroxo species also play a key role in the electron-hole ($e^- - h^+$) recombination reaction[131, 135, 136] and these species are likely be more preponderant on a (hydroxylated) anatase surface than on rutile.

Another interesting trend emerging from this part of the study is that composite films containing occluded semiconductor particles do not manifest significantly different photoelectrochemical profiles than their microporous semiconductor film counterparts. This is seen in both the similar shapes of the photovoltammograms (e.g., Figure 3.16) in the two cases as well as in the photoaction spectral behavior. It is thus tempting to conclude that the matrix in our composite films serves mainly to remove the majority carriers photogenerated in a given particle. In an electrolyte-permeated microporous particle network on the other hand, the particle interconnects (beyond the percolation threshold) serve the function of shuttling the electrons (to the back contact). In both cases, hole transfer occurs across the semiconductor particle/electrolyte boundary. Therefore it is reasonable that the two types of films evoke similar photoelectrochemical responses. However, the better performance of the composite film architecture relative to the matrix alone (c.f., Figures 3.16a and b) rests with the role of the TiO_2/WO_3 junction in being able to better spatially separate the photogenerated e^- - h^+ pairs, thereby inhibiting their recombination. Our group have also observed similar enhanced performance for composite films comprising of occluded TiO_2 particles in an electrosynthesized titania matrix.[137, 138] Clearly, even in a chemically identical composite film situation, the particle/matrix contacts aid in vectorial e^- - h^+ pair separation and charge transport.

Finally, it must be noted that electron injection from TiO_2 to WO_3 is favored by the lower-lying conduction band in the latter. Undoubtedly this is a beneficial feature in the WO_3-TiO_2 composite films. Precedence for this favorable influence of WO_3 is also found in previous studies on WO_3-TiO_2 composites prepared by other methods.[34, 41] It is particularly noteworthy that a relatively small fraction of TiO_2 (in the overall composite film matrix) translates to a rather dramatic improvement in its photoresponse (see for example Figure 3.17). This is undoudtedly due to the presence of WO_3-TiO_2 particle contacts within the composite and the attendant possibility of vectorial electron transfer from TiO_2 to the WO_3 matrix component.

3.4 Pulsed Electrodeposition of WO_3-TiO_2 Composite Films

Figure 3.20 contains representative scanning electron micrographs of WO_3-TiO_2 (A) and WO_3-TiO_2 (B) film samples contrasting the vastly different grain morphology in the two cases and of the TiO_2 and WO_3 components themselves. Thus TiO_2 deposits are much more fine-grained than their WO_3 counterparts. Both types of films are rather compact with WO_3-TiO_2 (A) being much thicker than WO_3-TiO_2 (B). In WO_3-TiO_2 (A), spherical agglomerates of varying size from 100 nm to ca. 5 μm are present in a network structure of the two components. At variance, WO_3-TiO_2 (B) consists of much smaller spherical particles ranging in size from 100 nm to 500 nm. The thicker films formed from the mixed bath can be rationalized by the enhanced deposition rate of the two components at the negative end of the pulse waveform. In both cases, there is intimate electronic contact between the TiO_2 and WO_3 components within the film microstructure.

The side perspectives from SEM in Figure 3.21 contrast composite WO_3-TiO_2 (A) (Figure 3.21a) and WO_3-TiO_2 (B) (Figure 3.32b) film morphologies. The layering resulting from the 5-repeat cycle sequential deposition (see Experimental) is clearly seen in Figure 3.21b and this layered morphology is absent for the sample from pulsed deposition from a mixed bath (c.f., Figure 3.21a). It is worth noting that the layers are nanoporous and thus deposition of TiO_2 occurs within the WO_3 matrix in each layer.

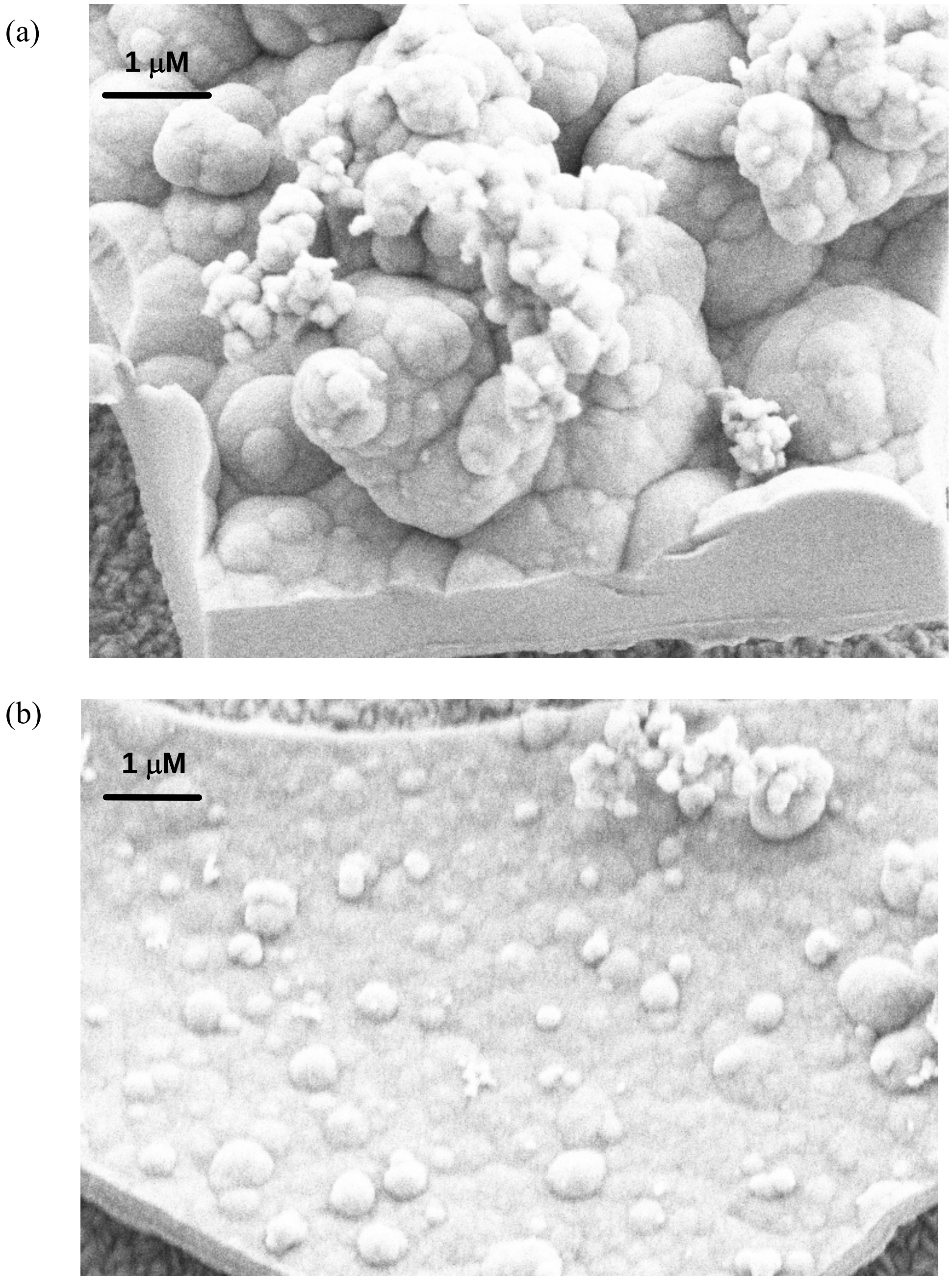

Figure 3.20: Scanning electron micrograph of (a) WO_3-TiO_2 (A) and (b) WO_3-TiO_2 (B) composite film samples. The small grains are TiO_2 decorating the much larger WO_3 grains.

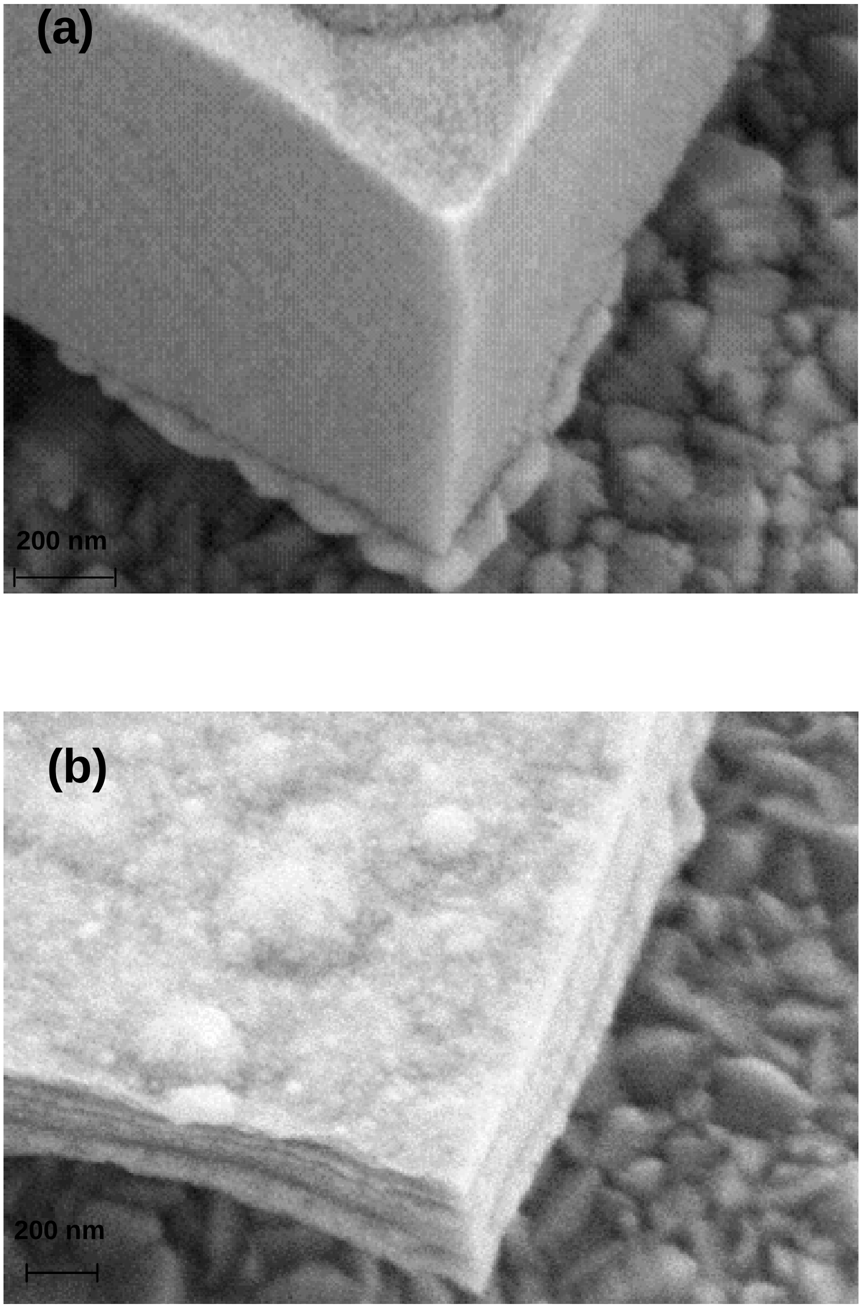

Figure 3.21: Side perspectives of (a) WO_3-TiO_2 (A) and (b) WO_3-TiO_2 (B) composite film samples obtained from tilting the SEM sample stage by 20^0.

Interestingly enough, the WO_2-TiO_2 (B) films contain a higher proportion of TiO_2 than their WO_3-TiO_2 (A) composite film counterparts. For example, XPS elemental assays afford a W: Ti atom percent ratio of 86:14 for WO_3-TiO_2 (A) and 78:22 for WO_3-TiO_2 (B) respectively. XPS spectrum of WO_3-TiO_2 (A) and WO_3-TiO_2 (B) films is shown in Figure 3.22. This trend is entirely in accord with the fact that WO_3 deposition interferes with TiO_2 deposition in the mixed bath case. By separating the bath chemistry in the sequential deposition strategy, this interference from WO_3 deposition is avoided.

Figure 3.23 contains three sets of linear sweep photovoltammograms for WO_3 (Figure 3.23A), WO_3-TiO_2 (A) (Figure 3.23B), and WO_3-TiO_2 (B) (Figure 3.23C). In each frame, the scans are compared with and without formate addition to the Na_2SO_4 supporting electrolyte. The photocurrent enhancement on formate addition occurs for reasons elaborated elsewhere.[126] Suffice here to note that formate is a more facile scavenger of the photogenerated holes in the oxide semiconductor film than either adsorbed hydroxyl groups or water molecules (see Section 3.3 above). Clearly WO_3-TiO_2 (B) films show the best photoelectrochemical response amongst the three types of films considered. It is also worth noting that composite WO_3-TiO_2 (A) films outperform WO_3 as discussed in our companion papers.[33, 36]

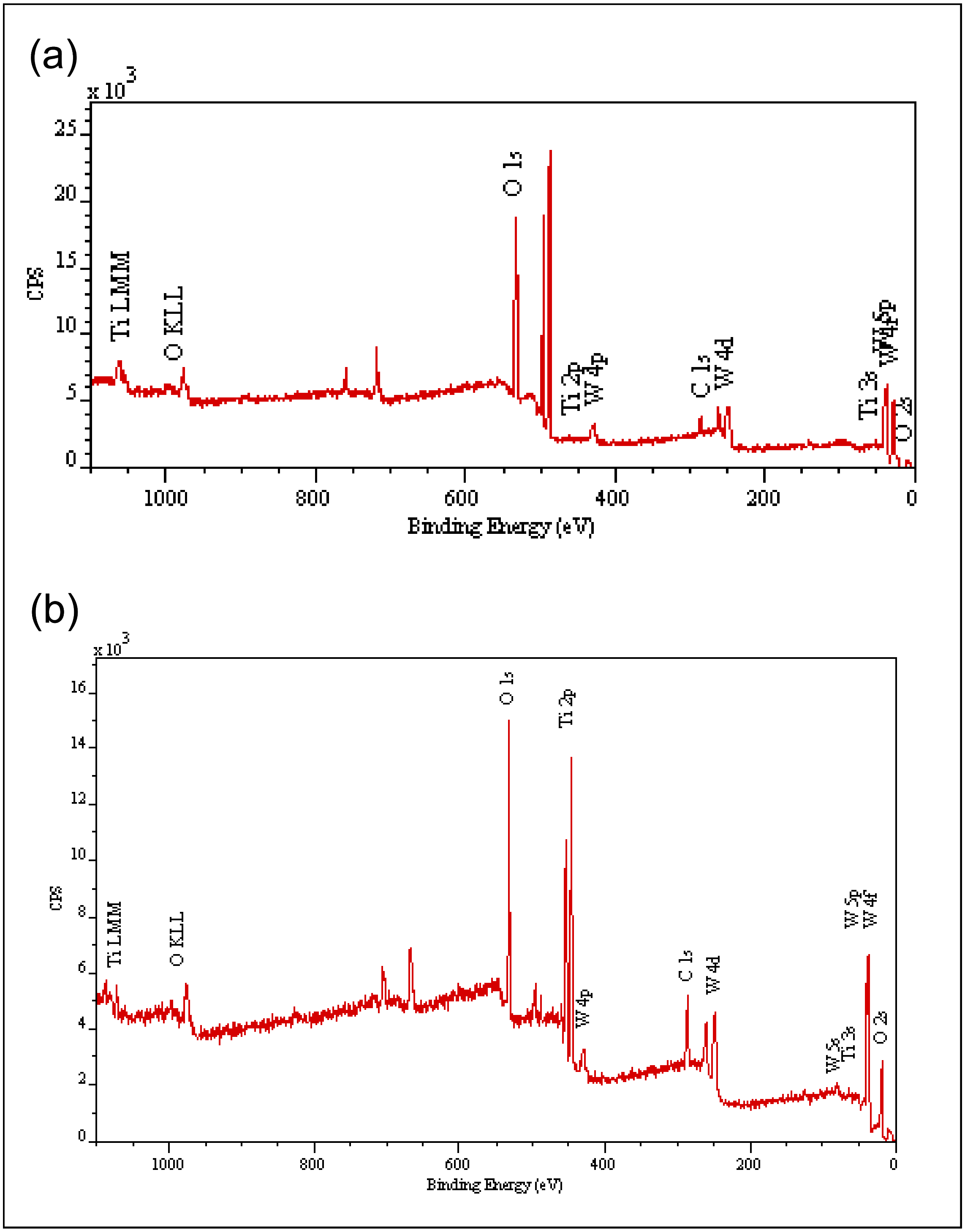

Figure 3.22: Survey XPS scans for a sample of (a) WO_3-TiO_2 (A) (b) WO_3-TiO_2 (B).

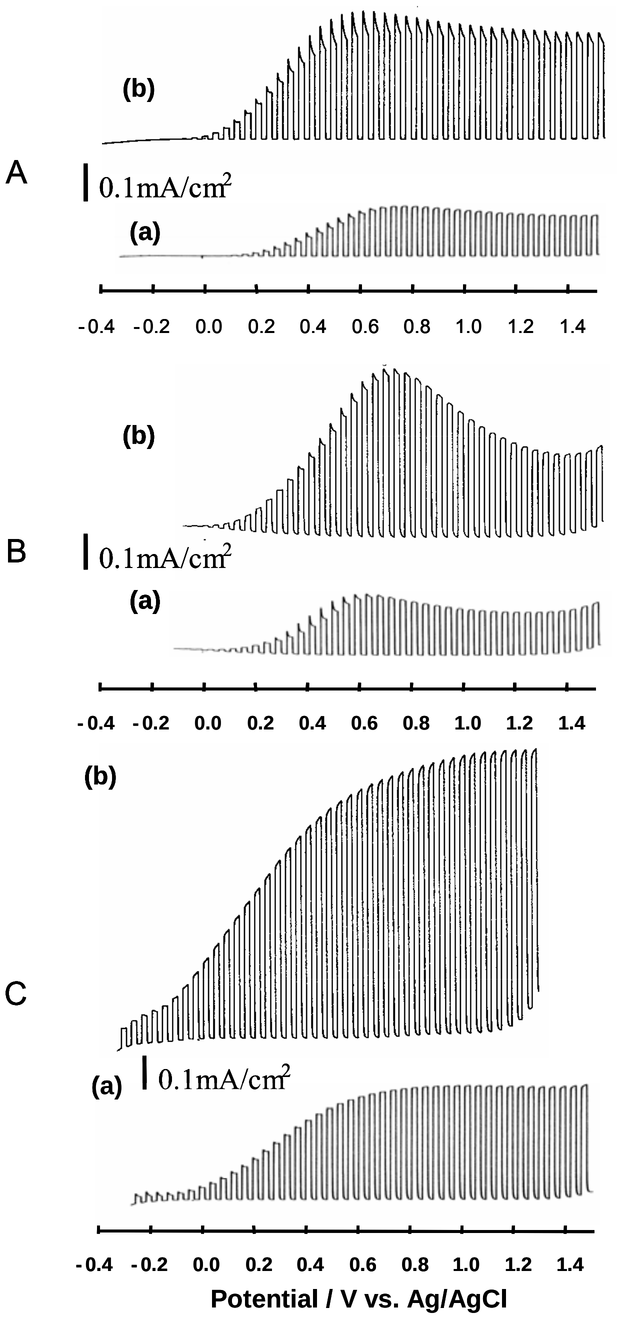

Figure 3.23: Photocurrent-potential profiles with chopped irradiation (chopping frequency = 0.2 Hz) in (a) 0.5 M Na_2SO_4 and (b) 0.5 M Na_2SO_4 + 0.1 M HCOONa for (A) electrodeposited WO_3, (B) composite WO_3-TiO_2 (A) and (C) composite WO_3-TiO_2 (B) films respectively. The potential scan rate was 2 mV/s.

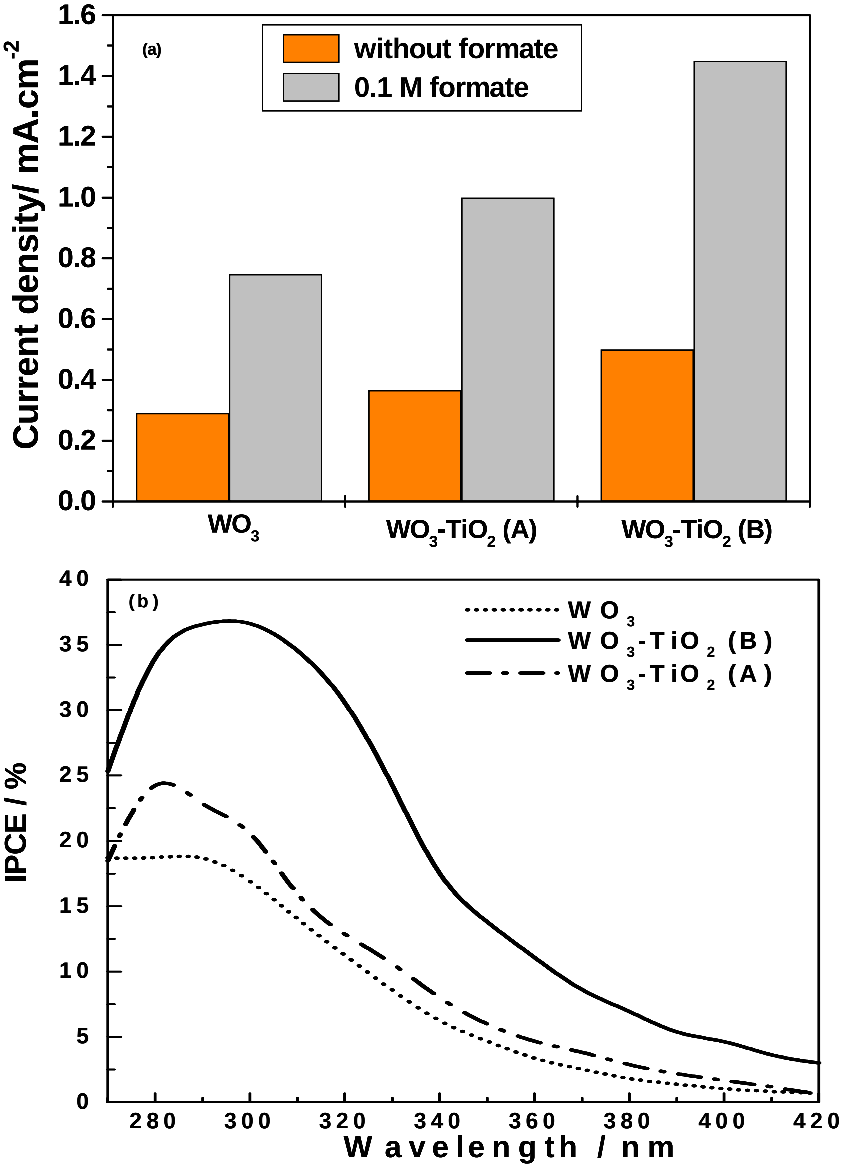

Figure 3.24: (a) Histogram plots of photocurrent densities of WO_3 and WO_3-TiO_2 composite films taken from the photovoltammograms in Figure 3.23 at a fixed potential of 0.8 V. (b) Comparison of photoaction spectra of WO_3 and WO_3-TiO_2 composite films in 0.5 M Na_2SO_4. Spectra acquired at a bias potential of 0.8 V.

These trends are amplified in the histogram plots in Figure 3.24a as well as in the photoaction spectra contained in Figure 3.24b. The layered morphology of the WO_3-TiO_2 (B) films (as exemplified by the SEM data in Fig. 3.21b) clearly aids vectorial electron transfer and minimizes electron-hole recombination within the film. In this regard, the better performance of both types of composite films, namely WO_3-TiO_2 (A) and WO_3-TiO_2 (B), relative to WO_3 (as seen in both Figures 3.23 and 3.24) underlines the beneficial effect of electronic junctions between the WO_3 and TiO_2 components in terms of spatially separating the photogenerated e^- - h^+ pairs. This feature has been discussed both by us[33, 36] and by other authors.[34, 35]

It is worth noting here that the band edges in WO_3 and TiO_2 are aligned such that the photogenerated electrons in TiO_2 can move into the WO_3 phase while the photogenerated holes move in the opposite direction resulting in vectorial charge transfer.[34, 35, 36] A tentative explanation for the peculiar peak-shaped response seen in the photovoltammograms in Figure 3.22B rests with the very different extent of light absorption by WO_3 and TiO_2. Thus the light penetrates into WO_3 to the extent of ca. 1.3 μm at 340 nm[126] while the penetration depth is much shallower for TiO_2. Therefore WO_3-TiO_2 (A) films initially show a higher contribution of photocurrent from TiO_2 particles located in the outer regions of the composite film. As the potential is driven more positive, the photocurrent mainly originates from the WO_3 component because of its higher light penetration depth. These results in a peaked response (see also Ref. 126).

3.5 Visible Light-Driven Hydrogen Production Using p-Cu_2O Photocathode

The relative energy level positions for p-Cu_2O are compared and contrasted with the n-TiO_2 prototype in relation to the hydrogen evolution rection and oxygen evolution reaction redox levels (Figure 1.15). While, the driving force for hydrogen evolution reaction is much higher for p-Cu_2O relative to n-TiO_2 (higher-lying conduction band edge), the valence band edge position of p-Cu_2O is such that the photogenerated holes simply do not have enough energy to oxidize water.

Our p-Cu_2O based photoelectrochemical cell is schematically shown in Figure 2.3. It can be immediately recognized that this photocatalytic approach mimics the strategy shown in Figure 1.13b. In this case, instead of actually photo splitting water, sacrificial electron donors are added to the solution such that the hydrogen evolution reaction and oxygen evolution reaction steps are separately optimized and studied. It must be borne in mind that now the overall photoreaction becomes thermodynamically “down-hill” and is more appropriately termed: “photocatalytic”.

3.5.1 Strategies for Optimizing the p-Cu_2O-Based Photoelectrochemical Cell

(a) Using sacrificial electron donors in anode compartment:

A variety of electron donors (reducing agents) were screened using cyclic voltammetry, as shown in Figure 3.25. The best electron donor should have the most positive oxidation potential; E_{ox}. According to Figure 3.25 and Table 3.5, hydroquinone

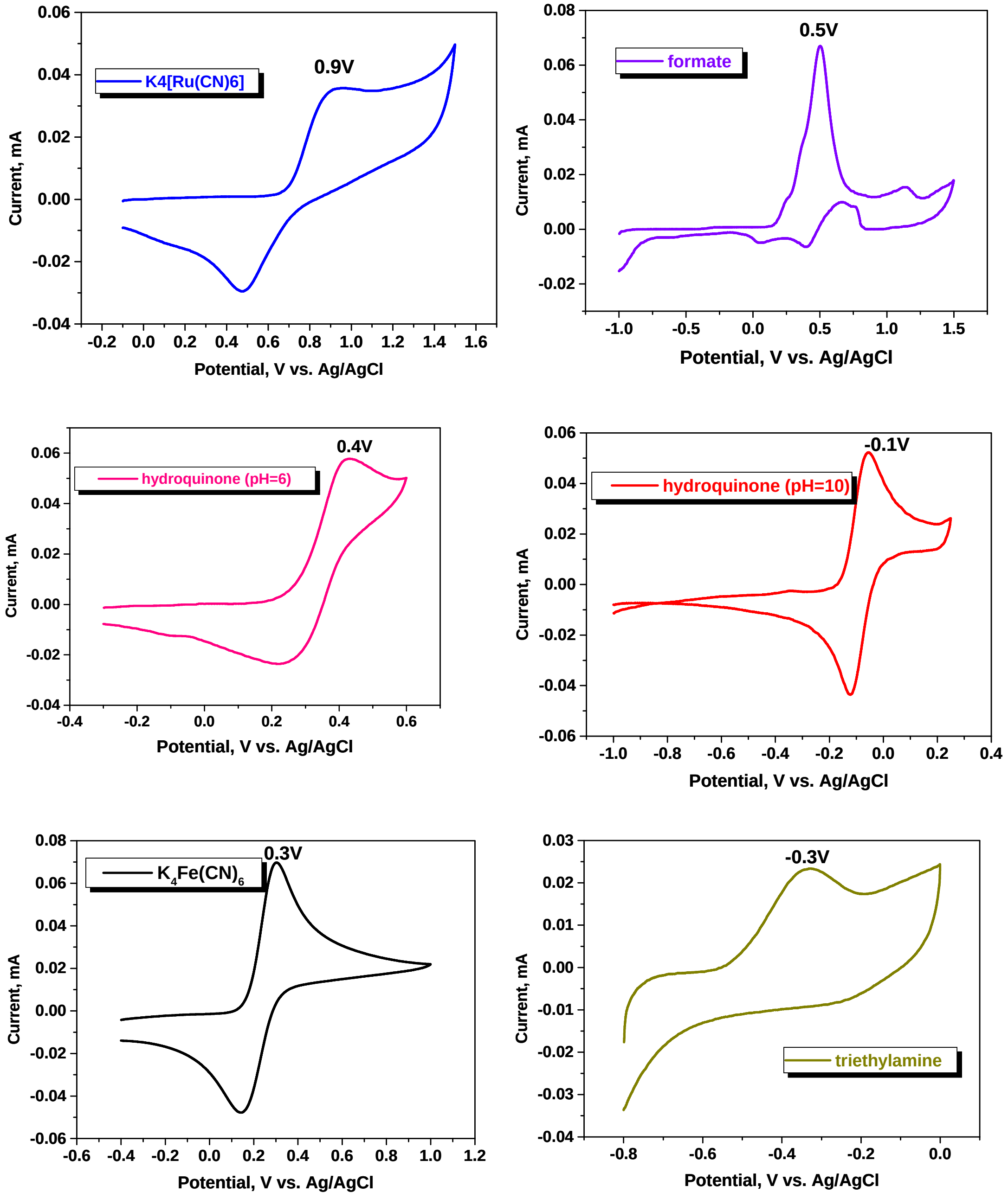

Figure 3.25: Cyclic voltammograms of various electron donor candidates.

Table 3.5: Oxidation potentials (E_{ox}) of various electron donors as determined by cyclic voltammetry

Electron donor	$\mathbf{E_{ox}}$
$K_4[Ru(CN)_6]$	0.9 V
formate	0.5 V
$K_4[\ Fe(CN)_6]$	0.3 V
hydroquinone (pH=6)	0.4 V
hydroquinone (pH=10)	-0.1 V
triethylamine	-0.3 V

at pH 10 and triethylamine appear to be good electron donors; however, the redox reaction of triethylamine is irreversible (see bottom right-band frame in Figure 3.25).

(b) Modification of p-Cu_2O surface with Ni/NiO:

The p-Cu_2O surface was modified with a Ni/NiO layer using photodeposition as described in the Experimental Section. The presence of an ultrathin Ni layer on the p-Cu_2O surface protects it from surface photocorrosion (see equations 1.12 and 1.13). Also the Ni layer will drain the electrons more effectively from the CB of p-Cu_2O minimizing the electron recombination.

$$\text{p-}Cu_2O + 2h\nu \longrightarrow 2h^+ + 2e^- \tag{3.21}$$

$$Ni^{2+} + 2e^- \longrightarrow Ni \tag{3.22}$$

The conduction band electrons in p-Cu_2O are able to reduce Ni^{2+} to Ni (Figure 1.18). By comparing the absorption spectra of p-Cu_2O and $NiSO_4$ aqueous solution (Figure 3.26) it is clear that the spectral region of interest (450 nm to 580 nm) for photocatalytic Ni deposition (equations 3.21 and 3.22) does not overlap with the aqueous Ni^{2+} absorption spectrum. The presence of Ni on the p-Cu_2O surface is clearly shown by XPS (Figure 3.27).

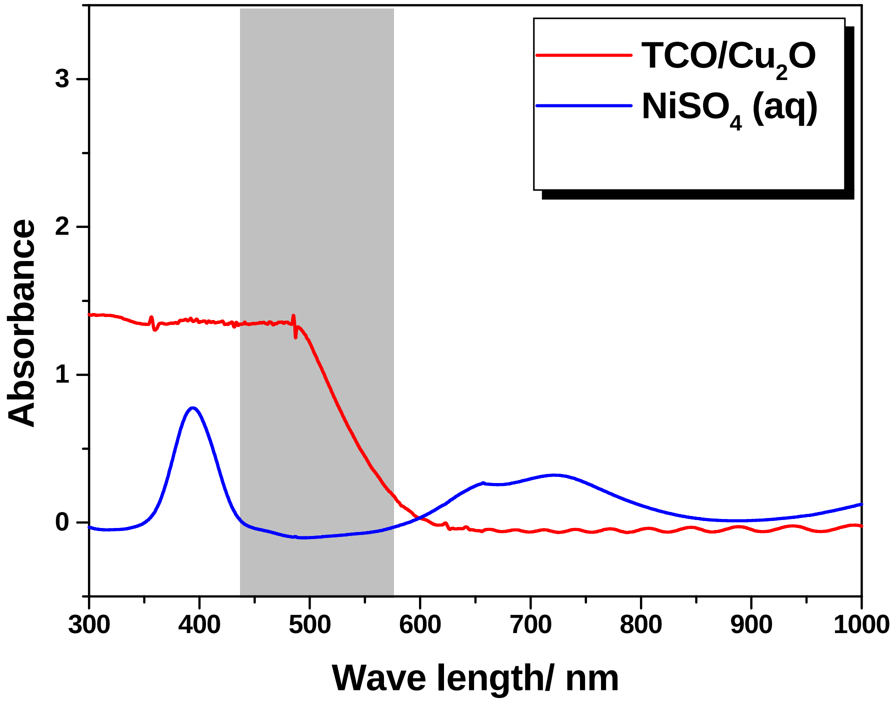

Figure 3.26: UV-visible spectrum of TCO/Cu_2O electrode (—) and 0.01 M $NiSO_4$ solution (—).

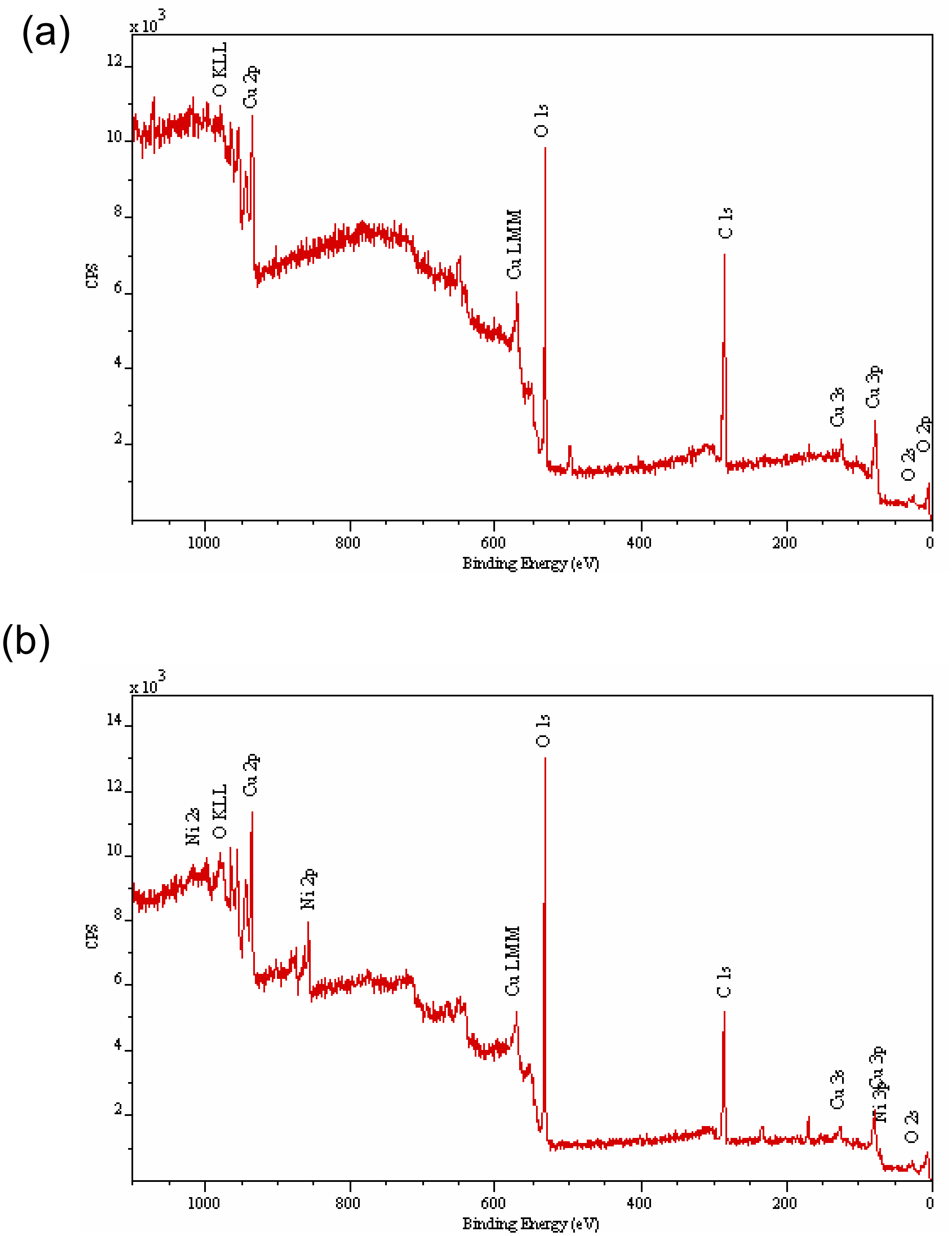

Figure 3.27: Survey XPS scans for a sample of: (a) TCO/p-Cu_2O (b) TCO/p-Cu_2O/Ni.

By combining both these strategies, we optimized the performance for the above photoelectrochemical cell shown in Figure 2.3. The results are shown as bar graphs in Figure 3.28a. It is worth noting that going from bare p-Cu_2O in 12 M NaOH to p-Cu_2O/Ni in hydroquinone at pH 10 gave an enhancement of short-circuit photocurrent by two orders of magnitude.

(c) Effect of electron scavenger in the cathode compartment:

Figure 2.28b compares the short-circuit photocurrent with and without methyl viologen (MV^{2+}) in the cathode compartment. An enhancement of the photocurrent is seen when MV^{2+} is present in the cathode compartment; MV^{2+} is known to be a facile electron acceptor. [139,140]

Figure 3.29 shows the evolution of the methyl viologen radical cation ($MV^{+\cdot}$) spectral signature with time in the solution layer adjacent to the p-Cu_2O surface. These spectra were acquired in situ (see Experimental Section) at a potential of -0.30 V. The absorbance due to $MV^{+\cdot}$ (at 605 nm) steadily systematically increases with time and attains a plateau (Figure 3.29b). Simultaneously, a visible blue coloration of the solution layer adjacent to the p-Cu_2O surface could be seen.

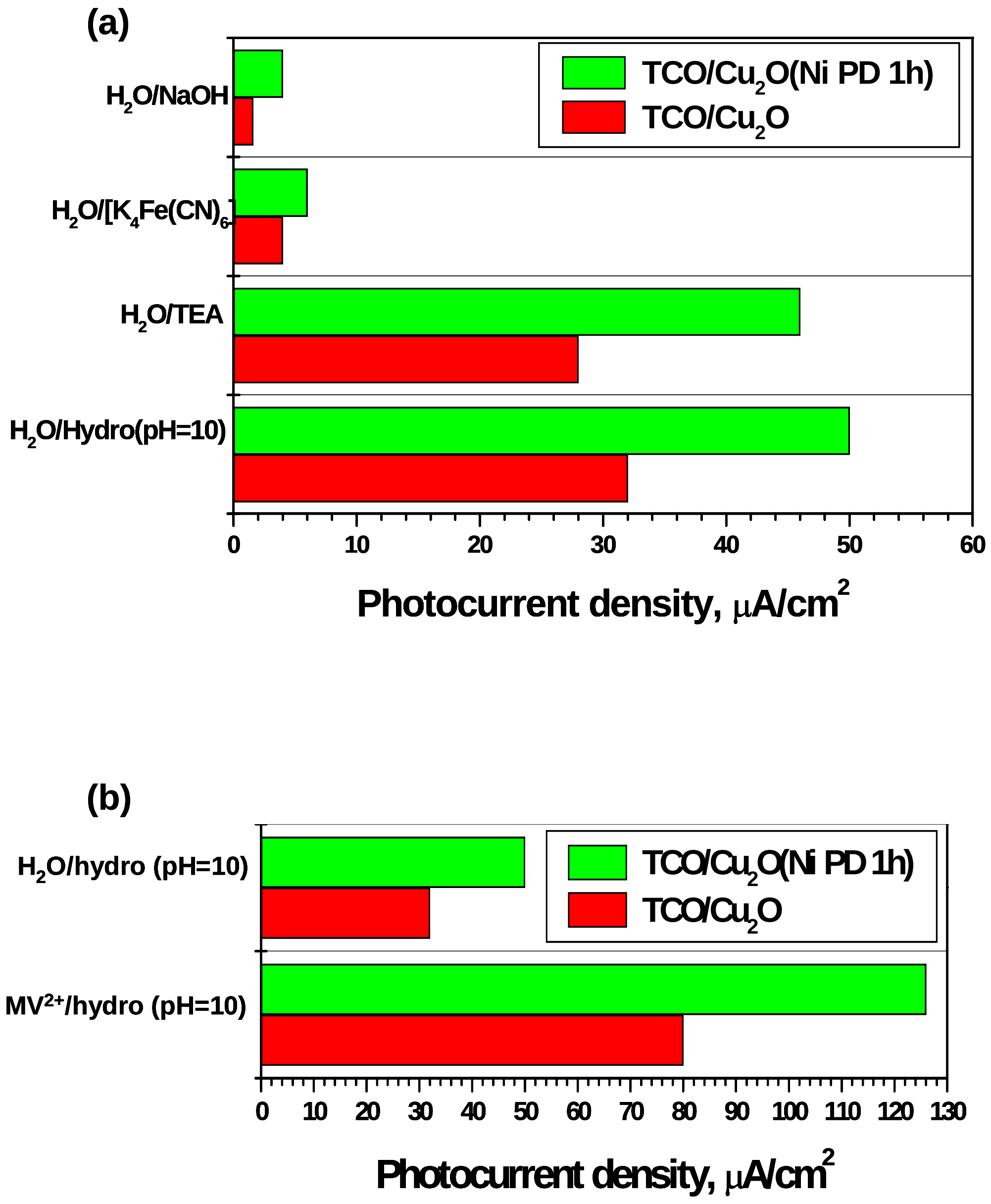

Figure 3.28: Comparison of short circuit photocurrent of PEC cell containing (a) various sacrificial electron donors in the anode compartment with bare p-Cu_2O photoelectrode and p-Cu_2O photoelectrode surface modified with Ni/NiO (b) with and without MV^{2+} in the cathode compartment.

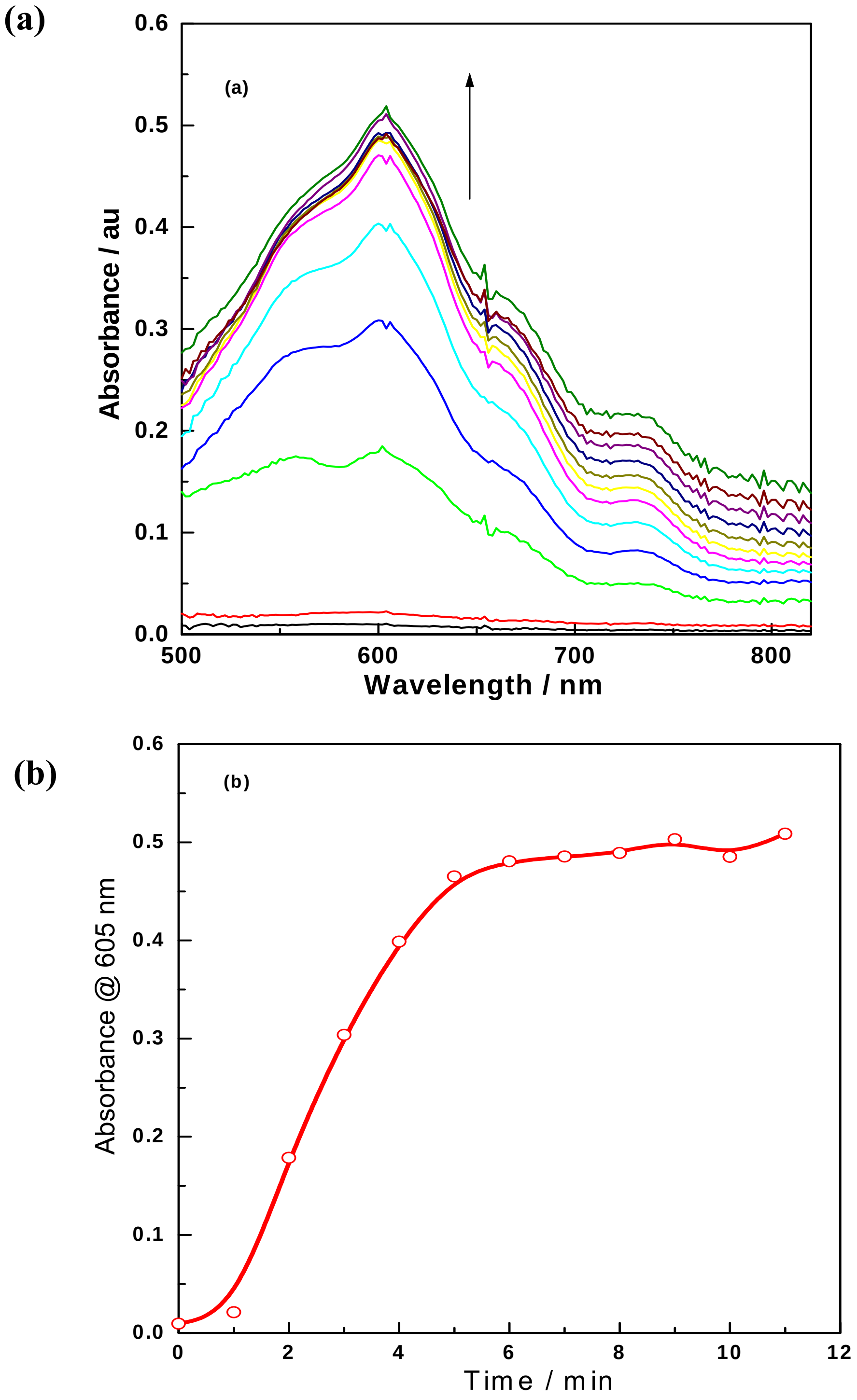

Figure 3.29: (a) Evolution of $MV^{\cdot+}$ (λ_{max}= 605 nm) by irradiation of p-Cu_2O film in 0.5 M Na_2SO_4 containing 40 mM MV^{2+} (b) Variation of absorbance at 605 nm vs. irradiation time.

Figure 3.31 shows the transient photocurrent measured in the cell in the presence of MV^{2+} in the cathode compartment. Following irradiation, the photocurrent increased to 550 μA and then showed a fast decrease to 80 μA. After 100 seconds, the solution was stirred and the photocurrent immediately increased and reached the value of 550 μA (the spike value), and remained stable for a long period of irradiation. The changes in the photocurrent values seen in Figure 3.31 signal mass transport limitations associated with the diffusion of MV^{2+} species to the p-Cu_2O surface. The data in Figure 3.32 elaborate these mass transport effects.

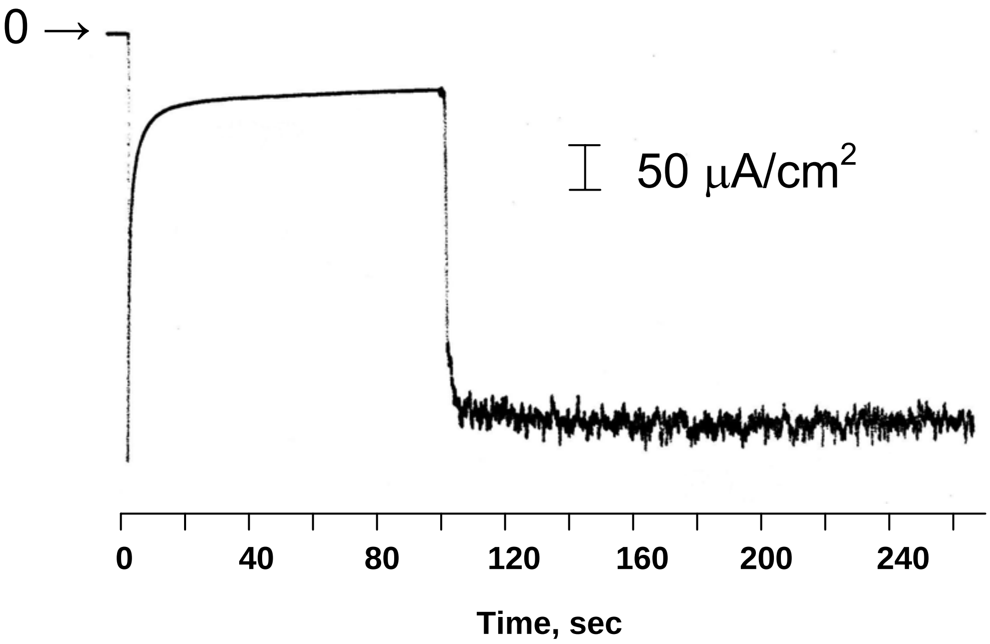

Figure 3.31: Transient photocurrent of p-Cu_2O photoelectrochemical cell for a 0.5 M Na_2SO_4 solution containing 40 mM MV^{2+} at an applied potential of -0.30 V.

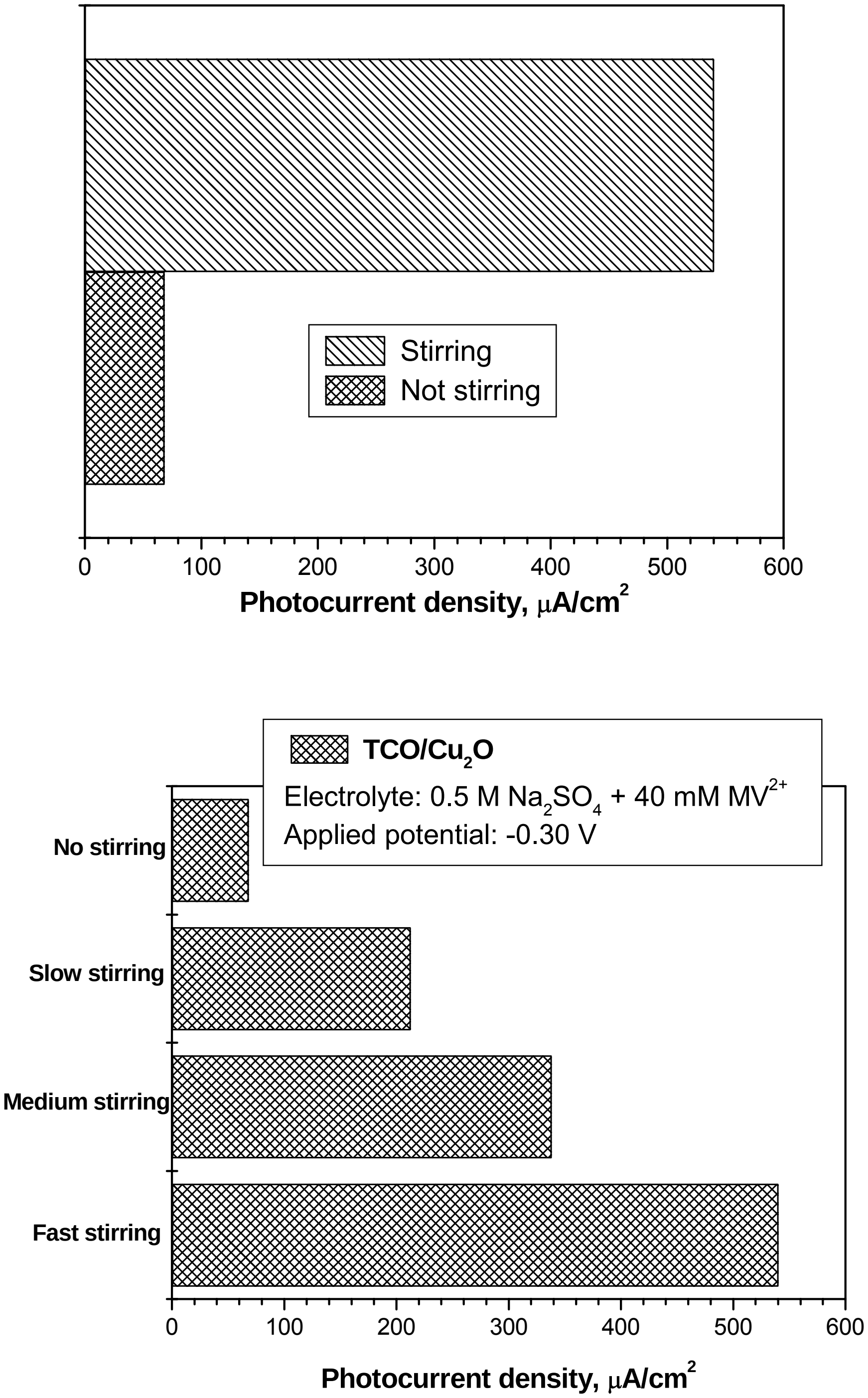

Figure 3.32: Phocurrent dependence on stirring rate.

Finally, the p-Cu_2O surface was modified with Cu_2O nanoparticles using the occlusion electrodeposition procedure (Experimental Section). Even though not dramatic, a slight improvement in the short-circuit photocurrents was observed (Figure 3.33). This improvement is attributable to an increase in surface area on chemical modification with the Cu_2O nanoparticles.

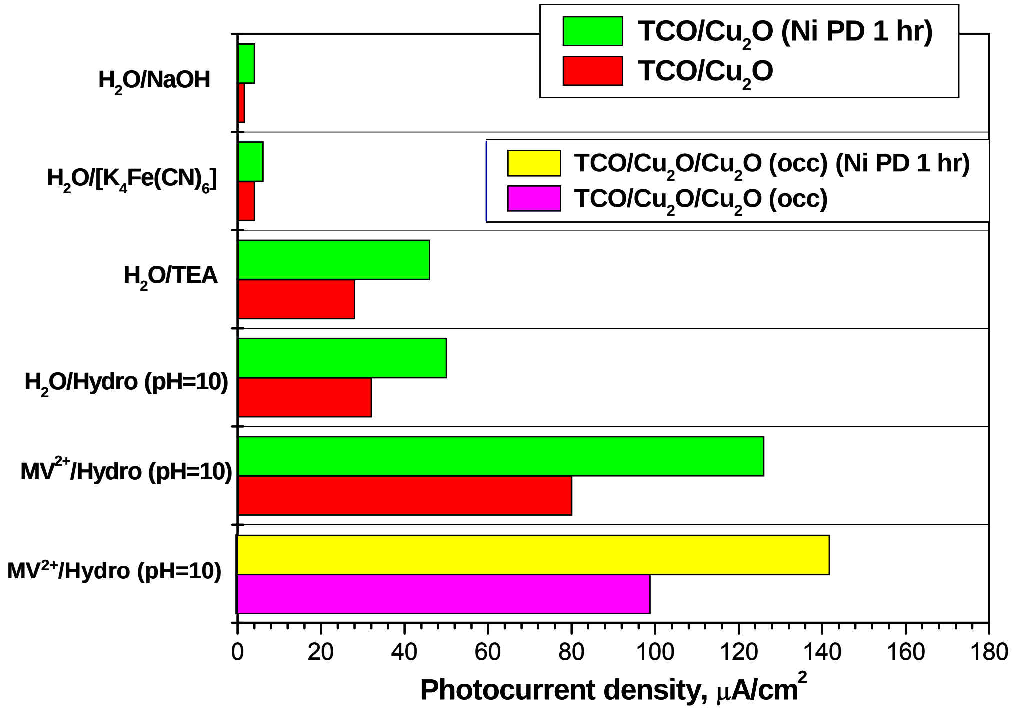

Figure 3.33: Comparison of short-circuit photocurrents in the p-Cu_2O-based PEC cell with and without occluded Cu_2O nanoparticles.

CHAPTER 4

SUMMARY AND CONCLUDING REMARKS

Trends in the reactivity of four metal ions [Cd^{2+}, Zn^{2+}, Mn^{2+}, and Tl^{+}] to undergo free radical-mediated heterogeneous photocatalytic reduction in UV-irradiated TiO_2 suspensions, have been presented in this dissertation study. These metal ions either have more negative standard reduction potentials or lie very close to the TiO_2 conduction band edge such that the direct reduction route involving photogenerated electrons in TiO_2 can be neglected. The good correspondence of the present data with the reactivity trends for these same four metal ions in homogeneous media suggests that the dominant role of TiO_2 is as a source of the free radicals. Indeed, interfacial adsorption does not appear to be an overriding factor, at least under the experimental conditions utilized in this study.

A simple kinetics scheme was developed and experimentally tested for the first time for the free radical-mediated (indirect) reduction route. Thus a detailed set of experiments were performed on the Tl(I) system for testing against the kinetics model and the predictions from this model were shown to be in excellent agreement with experimental data.

The crucial aspect with the photoassisted deposition of MSe on the TiO_2 surface is that the free energy of compound formation (ΔG_{MSe}) effectively shifts the redox potentials in the $Cd^{2+/0}$ and $Pb^{2+/0}$ cases in the positive direction. This shift is somewhat larger in the PbSe case relative to CdSe because of the more favorable ΔG_{MSe} value, -264.5 kJ/mol for PbSe vs. -136.4 kJ/mol for CdSe, Refs. 21, 22. Experimental data are in accord with these expectations. The chronopotentiometric studies furnish further mechanistic information on this new photoelectrosynthesis process. Note that this process has an environmental relevance (e.g., for removing toxic Cd and Pb species from water) in addition to a synthetic application.

The part of the dissertation study on WO_3-TiO_2 nanocomposite or layered films serves to illustrate that composite film architecture is a versatile framework for probing the influence of prior history (e.g., thermal pre-treatment) on the photoelectrochemical behavior of the occluded semiconductor particles. This study specifically shows that depending on the calcination history (anatase vs. rutile), the composite film can be tuned for photooxidizing either water or organic additives. Another interesting trend emerging from this part of the study is that composite films containing occluded semiconductor particles do not manifest significantly different photoelectrochemical profiles than their microporous semiconductor film counterparts.

Previous studies in our laboratory[33, 36] have shown pulsed electrodeposition to be a useful technique for preparing composite WO_3-TiO_2 films from a mixed aqueous bath containing the tungsten and titanium precursor species. The present dissertation study describes another variant of the cathodic electrodeposition strategy that relies on sequential deposition of WO_3 and TiO_2 from two separate baths containing the tungsten and titanium precursor species, respectively. This new approach produces composite

WO_3-TiO_2 films with superior photoresponse relative to counterparts obtained from a single bath.

The final aspect of this dissertation work deals with visible light generation of H_2 from water. A *galvanic* photoelectrochemical cell built from electrodeposited p-Cu_2O in the cathode compartment and a sacrificial electron donor in the anode compartment was tested and optimized. Further improvements in the charge transfer kinetics across the two electrode/electrolyte interfaces are needed to boost the short-circuit photocurrent densities to the several mA/cm^2 levels needed for practical H_2-generation devices. Concurrent measurement of the amount of photogenerated H_2 can also be accomplished then. Finally, one strategy to add value to this process is to use an environmental pollutant (e.g.,toxic dye) as an electron donor in the anode compartment. Thus, a pollutant would be destroyed and H_2 concurrently generated in the same solar device.

REFERENCES

1. Kraeutler, B.; Bard, A. J. *J. Am. Chem. Soc.* **1978,** *100*, 4317.

2. Funt, B. L.; Tan, S-R. *J. Poly. Sci.: Polym. Chem. Ed.* **1984,** *22*, 605.

3. Okano, M.; Kikuchi, E.; Itoh, K.; Fujishima, A. *J. Electrochem. Soc.* **1988,** *135*, 1641.

4. Yildiz, A.; Sobczynski, A.; Bard, A.J.; Campion, A.; Fox, M.A.; Mallouk, T.E.; Webber, S.E.; White, J.M. *Langmuir* **1989,** *5*, 148.

5. Fox, M.A.; Worthen, K. L. *Chem. Mater.* **1991,** *3*, 253.

6. Yoneyama, H.; Kawai, K.; Kuwabata, S. *J. Electrochem. Soc.* **1988,** *135,* 1699.

7. Cunningham, J.; Zainal, H. *J. Phys. Chem.* **1972,** *76*, 2362.

8. Baba, R.; Konda, R.; Fujishima, A.; Honda, K. *Chem. Lett.* **1986,** 1307.

9. Forouzan, F.; Richards, T. C.; Bard, A. J. *J. Phys. Chem.* **1996,** *100*, 18123 .

10. (a) Lin, W-Y.; Rajeshwar, K. *J. Electrochem. Soc.* **1997,** *144*, 2751. (b) Chenthamarakshan, C. R.; Yang, H.; Savage, C. R.; Rajeshwar, K. *Res. Chem. Intermed.* **1999,** *25*, 861. (c) Yang, H.; Lin, W-Y.; Rajeshwar, K. *J. Photochem. Photobiol. A: Chem.* **1999,** *123*, 137. (d) Chenthamarakshan, C. R.; Rajeshwar, K. *Electrochem. Commun.* **2000,** *2*, 527. (e) Chenthamarakshan, C. R.; Yang, H.; Ming, Y.; Rajeshwar, K. *J. Electroanal. Chem.* **2000,** *494*, 79. (f) Ming, Y.; Chenthamarakshan, C. R.; Rajeshwar, K. *J. Photochem. Photobiol. A: Chem.*

2002,*147*, 199. (g) Kajitvichyanukul, P.; Chenthamarakshan, C. R.; Rajeshwar, K.; Qasim, S. R. *J. Electroanal. Chem.* **2002,** *519*, 25. (h)Rajeshwar, K.; Chenthamarakshan, C. R.; Ming, Y.; Sun, W. *J. Electroanal. Chem.* **2002,** *538-539*, 173.

11. (a) Chenthamarakshan, C. R.; Ming, Y.; Rajeshwar, K. *Chem. Mater.* **2000,** *12*, 3538. (b) Rajeshwar, K.; Chenthamarakshan, C. R.; de Tacconi, N. R. Paper No. 152, 204th Meeting of the Electrochemical Society, Orlando, Florida, October (2003).
12. Rajeshwar, K.; de Tacconi, N. R.; Chenthamarakshan, C. R. *Chem. Mater.* **2001,** *13*, 2765.
13. Hoffmann, M. R.; Martin, S. T.; W. Choi, W.; Bahnemann, D. W. *Chem. Rev.***1995**, *95*, 69.
14. Rajeshwar, K. *J. Appl. Electrochem.* **1995**, *25*, 1067.
15. Rajeshwar, K.; Ibanez, J. *Environmental Electrochemistry*; Academic Press: San Diego, 1997.
16. Blake, D. M. Bibliography of Work on the Heterogeneous Photocatalytic Removal of Hazardous Compounds from Water and Air. NREL/TP-570-26797, National Renewable Energy Laboratory, Golden, CO, 1999. Update No. 4 to October 2001, NREL/TP-510-31319.
17. Litter, M. I. *Appl. Catal. B. Environ.* **1999**, *23*, 89.
18. Linsebigler, A. L.; Lu, G.; Yates, Jr., J. T. *Chem. Rev.* **1995**, *95*, 735.

19. Fujishima, A.; Rao, T. N.; Tryk, D. A. *J. Photochem. Photobiol. C: Photochem. Rev.* **2000**, *1*, 1.
20. Diebold, U. *Surf. Sci. Reports* **2003**, *48*, 53.
21. Rajeshwar, K.; Chenthamarakshan, C. R.; Ming, Y.; Sun, W. *J. Electroanal. Chem.* **2002**, *538-539*, 173. See also references therein.
22. See for example: Koppenol, W. H.; Rush, J. D. *J. Phys. Chem.* **1987**, *91*, 4429.
23. Schwarz, H. A.; Dodson, R. W. *J. Phys. Chem.* **1989**, *93*, 409.
24. Fahmi, A.; Minot, C.; Silvi, B.; Causa, M. *Phys. Rev. B.* **1993**, *47*, 11717.
25. Kavan, L.; Gratzel, M.; Gilbert, S. E.; Klemenz, C.; Scheel, H. J. *J. Am. Chem. Soc.* **1996**, *118*, 6717.
26. Maruska, H. P.; Gosh, A. K. *Solar Energy*, **1978**, *20*, 443.
27. Aaron, W. *Chem. Mater.* **1993**, *5*, 280.
28. Finklea, H. O. *Journal of Chemical Education,* **1983**, *60*, 325.
29. Turner, J. A. *Journal of Chemical Education,* **1983**, *60*, 327.
30. Milnes, A. G.; Feucht, D. L. *Heterojunctions and Metal Semiconductor Junctions,* Academic Press, New York and London, **1973,** chapter 5, p. 139.
31. Palmisano, L.; Sclafani, A. in: Schiavello, M. (Ed.), *Heterogeneous photocatalysis*, John Wiley & Sons, **1997**, p. 111.
32. Rajeshwar, K.; de Tacconi, N. R. in: Wieckowski A. (Ed.), *Interfacial Electrochemistry: Theory, Experiment, and Applications*, Marcel Dekker, New York, **1999**, p. 721.

33. de Tacconi, N. R.; Chenthamarakshan, C. R.; Rajeshwar, K.; Pauporté, T.; Lincot, D. *Electrochem. Commun.* **2003**, *5*, 220.

34. Shiyanovskaya I.; Hepel, M. *J. Electrochem. Soc.* **1998**, *145*, 3981.

35. Shiyanovskaya I.; Hepel, M. *J. Electrochem. Soc.* **1999**, *146*, 243.

36. de Tacconi, N. R.; Chenthamarakshan, C. R.; Wouters, K. L.; MacDonnell, F. M.; Rajeshwar, K. *J. Electroanal. Chem.* **2004**, *566*, 249.

37. Song, K. Y.; Park, M. K.; Kwon, Y. T.; Lee, H. W.; Chung, W. J.; Lee, W. I. *Chem. Mater.* **2001,** *13,* 2349.

38. Meijers, S.; Gielgens, L. H.; Ponec,V. *J. Catal.* **1995**, *156*, 147.

39. Eibl, S.; Gates, B. C.; Knözinger, H. *Langmuir,* **2001,** *17,* 107.

40. Tatsuma, T.; Saitoh, S.; Ohko, Y.; Fujishima, A. *Chem. Mater.* **2001,** *13*, 2838.

41. Kang, T.-S.; Moon, S.-H.; Kim, K.-J. *J. Electrochem. Soc.* **2002,** *149*, E155.

42. Hashimoto, S.; Matsuoka, H. *J. Electrochem. Soc*. **1991,** *138,* 2403.

43. Bonhote, P.; Gogniat, E.; Grätzel, M.; Ashrit, P.V. *Thin Solid Film,* **1999**, *350*, 269.

44. Hauch, A.; Georg, A.; Baumgärtner, S.; Opara Krašovec, U. Orel, B. *Electrochim. Acta*, **2001**, *46,* 2131.

45. Hauch, A.; Georg, A.; Opara Krašovec, U. Orel, B. *J. Electrochem. Soc.* **2002,** *149,* H159.

46. Hauch, A.; Georg, A.; Opara Krašovec, U. Orel, B. *J. Electrochem. Soc.* **2002,** *149,* A1208.

47. Su, W.-B.; Wang, J.-F.; Chen, H.-C.; Wang, W.-X.; Zhang, G.-Z.; Li, C.-P.; J. *Appl. Phys.* **2002,** *92*, 4779.

48. Switzer, J.A. *Ann. Ceram. Bull.* **1987**, *66,* 1521.

49. Therese, G.H.A.; Kamath, P.V. *Chem. Mater*. **2000,** *12*, 1195.

50. Yamanaka, K. *Jpn. J. Appl. Phys.* **1987,** *26*, 1884.

51. Shen, P.K.; Syed-Bokhari, J.; Tseung, A.C.C.; *J. Electrochem. Soc*. **1991**, *138*, 2778.

52. Shen, P.K.; Tseung, A.C.C. *Mater. Chem*. **1992**, *2,* 1141.

53. Meulenkamp, E.A. *J. Electrochem. Soc.* **1997**, *144,* 1664.

54. Shiyanovskaya, I.; Hepel, M.; Tewksburry, E. *J. New Mater. Electrochem. Syst.* **2000**, *3*, 241.

55. Pauporté, T. *J. Electrochem. Soc.* **2002**, *149*, C539.

56. Natarajan, C.; Nogami, G. *J. Electrochem. Soc*. **1996,** *143*, 1547.

57. Kavan, L.; Regan, B. O'.; Kay, A.; Grätzel, M. *J. Electroanal. Chem*. **1993,** *346*, 291.

58. Zhitamirsky, I. *Nanostruct. Mater*. **1997,** *8,* 521.

59. Zhitamirsky, I. *J. Eur. Ceram. Soc.* **1999**, *19,* 2581.

60. Matsumoto, Y. *MRS Bull.* **2000**, September, 47.

61. (a) Golden, T. D.; Shumsky, M. G.; Zhou, Y.; VanderWerf, R. A.; Van Leeuwen, R. A.; Switzer, J. A. *Chem. Mater.* **1996**, *8*, 2499. (b) J. A. Switzer, C-J. Hung, E. Bohannan, W.; Shumsky, M. G.; Golden, T. D.; Van Aken, D. C. *Adv. Mater.* **1997,** *9*, 334. (c) Switzer, J. A.; Hung, C-J.; Huang, L-Y.; Miller, F. S.; Zhou, Y.;

Raub, E. R.; Schumsky, M. G.; Bohannan, E. W. *J. Mater. Res,* **1998**. *13*, 909. (d) Switzer, J. A.; Hung, C-J.; Huang, L-Y.; Switzer, E. R.; Kammler, D. R.; Golden, T. D.; Bohannan, E. W. *J. Am. Chem. Soc.* **1998,** *120*, 3530. (e) Switzer, J. A.; Maune, B. M.; Raub, E. R.; Bohannan, E. W. *J. Phys. Chem. B,* **1999**, *103*, 395. (f) Bohannan, E. W.; Huang, L-Y.; Miller, F. S.; Schumsky, M. G.; Switzer, J. A. *Langmuir,* **1999,** *15,* 813.

62. Chenthamarakshan,C. R.; de Tacconi, N. R.; Shiratsuchi, R.; Rajeshwar, K.; *J. Electroanal. Chem.* **2003,** *553*, 77.

63. (a) Peulon S.; Lincot, D. *Adv. Mater.* **1996**, *8*, 166. (b) Peulon S.; Lincot, D. *J. Electrochem. Soc.* **1998, *145***, 864. (c) Pauporté T.; Lincot, D. *J. Electroanal. Chem.* **2001,** *517*, 54. See also references therein. (d) Pauporté, T.; Yoshida, T.; Goux, A.; Lincot, D. *J. Electroanal. Chem.* **2002,** *534*, 55.

64. (a) Izaki M.; Omi, T. *Appl. Phys. Lett.* **1996**, *68*, 2439. (b) Izaki M.; Omi, T.; *J. Electrochem. Soc.* **1996,** *143,* L53. (c) Izaki M.; Omi, T. *J. Electrochem. Soc.* **1997,** *144*, 1949.

65. (a) Gu, Z. H.; Fahidy, T. Z.; Hornsey, R.; Nathan, A. *Can. J. Chem.* **1997,** *75,* 1437. (b) Gu Z. H.; Fahidy, T. Z.; *J. Electrochem. Soc.* **1999,** *146*, 156.

66. (a) Chenthamarakshan, C. R.; de Tacconi, N. R.; Xu, L.; Rajeshwar, K. *Journal of Chemical Education,* **2004**, *81*, 1790. (b) Ellis, A. B.; Geselbracht, M. J.; Jonson, B. J.; Lisensky, G. C.; Robinson, W. R. in: *Teaching General Chemistry: A Materials Science Companion*, American Chemical Society, Washington, DC **1993**, p 415.

67. Fujishima, A.; Honda, K. *Nature*, **1972**, *37*, 238.

68. Ohno, T.; Haga, D.; Fujihara, K.; Kaizaki, K.; Matsumura, M. *J. Photochem. Photobiol. A:Chem.* **1998**, *118*, 41.

69. Sayama, K.; Yashoda, R.; Kusama, H.; Okabe, K.; Abe, Y.; Arakawa, H. *Chem. Phys. Lett.* **1997**, *277*, 387.

70. Bamwenda, G. R.; Sayama, K.; Arakawa, H. *J. Photochem. Photobiol. A:Chem.* **1999**, *122*, 75.

71. Maruthamuthu, P.; Ashokkumar, M.; Gurunathan, K.; Subramanium, E.; Shastri, M. V. C. *Int. J. Hydrogen Energy*, **1989**, *14*, 525.

72. Aspnes, D. E.; Heller, A. *CJ. Phys. Chem.* **1983**, *87*, 4919.

73. Heller, A.; Shalom, A.; Bonner, W. A.; Miller, B. *J. Am. Chem. Soc.* **1982**, *104*, 6942.

74. Hara, M.; Kondo, T.; Komoda, M.; Ikeda, S.; Kondo, J. N.; Domen, K.; Shinohara, K.; Tanaka, A. *Chem. Commum*, **1998**, *3*, 357.

75. Ikeda, S.; Takata, T.; Kondo, T.; Hitoki, G.; Hara, M.; Kondo, J. N.; Domen, K.; Hosono, H.; Kawazoe, H.; Tanaka, A. *Chem. Commum*, **1998**, *20*, 2185.

76. de Jongh, P. E.; Vanmaekelbergh, D.; Kelly. K. K. *Chem. Commum*, **1999**, *12*, 1069.

77. de Jongh, P. E.; Vanmaekelbergh, D.; Kelly. K. K. *J. Electrochem. Soc.* **2000**, *147(2)*, 486.

78. Pollack, G. P.; Trivich, D. *J. Appl. Phys*. **1975**, *46*, 163.

79. Tench, D.; Warren, L. F. *J. Electrochem. Soc.* **1983**, *130*, 869.

80. Rakshani, A. E.; Verghese, J. *Sol. Energy Mater.* **1987**, *15*, 237.

81. de Jongh, P. E.; Vanmaekelbergh, D.; Kelly. K. K. *Chem. Mater.* **1999**, *11*, 3512.

82. Paseka, I. *Electrochim. Acta,* **1995**, *40(11)*, 1633.

83. Shervedani, R. K.; Lasia, A. *J. Electrochem. Soc.* **1997**, *144(2)*, 511.

84. Shervedani, R. K.; Lasia, A. *J. Electrochem. Soc.* **1998**, *145(7)*, 2219.

85. Böhme, O.; Leidich, F. U.; Salge, H. J.; Wendt, H. *Int. J. Hydrogen Energy*, **1994**, *19*, 349.

86. Rausch, S.; Wendt, H. *J. Electrochem. Soc.* **1996**, *143*, 2853.

87. El-Deab, M. S.; Seleh, M. M. *Int. J. Hydrogen Energy*, **2003**, *28*, 1199.

88. Panek, J.; Serek, A.; Budniok, A.; Rówinski, E.; Lagiewka, E. *Int. J. Hydrogen Energy*, **2003**, *28*, 169.

89. Tavares, A. C.; Trasatti, S. *Electrochim. Acta,* **2000**, *45*, 4195.

90. Daftsis, E.; Pagalos, N.; Jannakoudakis, A.; Jannakoudakis, P.; Theodoridou, E.; Rashkov, R.; Loukaytsheva, M.; Atanassov, N. *J. Electrochem. Soc.* **2003**, *150*, C787.

91. Hu, C-C.; Tsay, C-H.; Bai, A. *Electrochim. Acta,* **2003**, *48*, 907.

92. Meguro, S.; Sasati, T.; Katagiri, H.; Habazaki, H.; Kawashima, A.; Sakaki, T.; Asami, K.; Hashimoto, K. *J. Electrochem. Soc.* **2000**, *147(8)*, 3003.

93. Han, Q.; Liu, K.; Chen, J.; Li, X.; Wee, X. *Int. J. Hydrogen Energy*, **2004**, *29*, 243.

94. Chen, X.; Rajeshwar, K.; Timmons, R. B.; Chen, J.-J.; Chyan, O. M. R. *Chem. Mater*. **1996**, *8*, 1067.

95. Lin, W.-Y.; Rajeshwar, K. *J. Electrochem. Soc.* **1993**, *140*, 2477.

96. Abdullah, M.; Low, G. K.-C.; Mathews, R. W. *J. Phys. Chem.* **1990**, *94*, 6820.

97. Connor, P. A.; McQuillan, A. J. *Langmuir* **1999**, *15*, 2402.

98. Kajitvichyanukul, P.; Chenthamarakshan, C. R.; Rajeshwar, K.; Qasim, S. R. *Adsorp. Sci. Technol.* **2003**, *21*, 217. See also references therein.

99. Bickley, R. I.; Gonzalez-Carreno, T.; Lees, J. S.; Palmisano, L.; Tilley, R. J. D.; *J. Solid State Chem.* **1991**, *92*, 178.

100. Wang, Z.; Chen, X.; Liu, J.; Mo, M.; Yang, L.; Qian, Y. *Solid State Commun.* **2004**, *130*, 585.

101. von Sonntag, C.; Schuchmann, H.-P. *Carbohydrates*. Jonah, C. D.; Rao, B. S. M. (Eds.), Elsevier, Amsterdam, 2001.

102. Neta, P.; Grodkowski, J.; Ross, A. B. *J. Phys. Chem. Ref. Data* **1996**, *25*, 709.

103. Rajh, T.; Ostafin, A. E.; Micic, O. I.; Tiede, D. M.; Thurnauer, M. C. *J. Phys. Chem.* **1996**, *100*, 4538.

104. Sun, W.; Chenthamarakshan, C. R.; Rajeshwar, K. *J. Phys. Chem. B* **2002**, *106*, 11531.

105. Butler, J.; Henglein, A. *Radiat. Phys. Chem.* **1980**, *15*, 603.

106. Fojtik, A.; Czapzki, G.; Henglein, A. *J. Phys. Chem.* **1970**, *74*, 3204.

107. Kajitvichyanukul, P.; Chenthamarakshan, C. R.; Rajeshwar, K.; Qasim, S. R. *Adsorp. Sci. Technol.* **2003**, *21*, 217.

108. Morrison, S. R. *The Chemical Physics of Surfaces*; Plenum Press, New York and London, 1977.

109. Mishra, K. K.; Rajeshwar, K. *J. Electroanal. Chem.* **1989**, *273*, 169.

110. Data for the calculation of ΔG_f^0 for PbSe from: *CRC Handbook of Chemistry and Physics*, 1st Student Edition, CRC Press, Boca Raton, FL, 1988, pp. D35-D77.

111. Tan, T. T. Y.; Zaw, M.; Beydoun, D.; Amal, R. *J. Nanoparticle Res.* **2002**, *4*, 541.

112. Da Silva Pereira, M. I.; Peter, L. M. *J. Electroanal. Chem.* **1982**, *131*, 167.

113. Frese, Jr., K. W. *J. Appl. Phys.* **1982**, *53*, 1571.

114. de Tacconi, N. R.; Chenthamarakshan, C. R.; Tacconi, E. J.; Rajeshwar, K., *J. Phys. Chem. B,* **2005**, *109*, 11953.

115. Hodes, G.; Howell, I. D. J.; Peter, L. M. *J. Electrochem. Soc.* **1992**, *139*, 3136.

116. de Tacconi, N. R.; Carmona, J.; Rajeshwar, K. *J. Phys. Chem. B* **1997**, *101*, 10151.

117. Wagner C. D.; Riggs, W. M.; Davis, L. E.; Mulder, J. F.; Mattenberg, G. E. *Handbook of X-ray Photoelectron Spectroscopy*, Perkin-Elmer Corporation (Physical Electronics Division): Eden Prairie, MN, 1979. The authentic samples were PbSe (Aldrich, 99.999%), CdSe (Aldrich, 99.99%), and Se (Alfa Aesar, 99.999%) respectively.

118. Rajeshwar, K.; de Tacconi, N. R.; in: P. V. Kamat, D. Meisel (Eds.), *Semiconductor Nanoclusters-Physical, Chemical, and Catalytic Aspects,* Elsevier, Amsterdam, 1997, p. 321.

119. Zhou, M.; de Tacconi, N. R.; Rajeshwar, K., *J. Electroanal. Chem.* **1997,** *421* 111.

120. Meulenkamp, E. A., *J. Electrochem. Soc.* **1997,** *144,* 1664.

121. Abraham, J.; Davidson, R. S.; Morrison, C. L., *J. Photochem.* **1985,** *29,* 353.

122. Ding, Z.; Lu, G. Q.; Greenfield, P. F., *J. Phys. Chem. B.* **2000,** *104,* 4815.

123. Yu, J. C.; Lin. J.; Lo, D.; Lam, S. K., *Langmuir* **2000,** *16*, 7304.

124. Sclafani, A.; Palmisano, L.; Schiavello, M.; *J. Phys. Chem.* **1990**, *94,* 829.

125. Mills, A.; Morris, S., *J. Photochem. Photobiol. A: Chem*. **1993**, *71,* 285.

126. Somasundaram, S.; Tacconi, N.; Chenthamarakshan, C. R.; Rajeshwar, K.; de Tacconi, N. R.; *J. Electroanal. Chem.* **2005**, *577,* 167.

127. Porto, S. P. S.; Fleury, P. A.; Damen, T. C., *Phys. Rev.* **1967,** *154*, 522.

128. Su, Y.; Balmer, M. L.; Bunker, B. C., *J. Phys. Chem. B.* **2000**, *104,* 8160.

129. Oosawa, Y.; Grätzel, M., *J. Chem. Soc., Chem. Commun.* **1984**, 1629.

130. de Tacconi, N. R.; Wenren, H.; McChesney, D.; Rajeshwar, K., *Langmuir,* **1998,** *14*, 2933.

131. Augustynski, J.; in: A. Wieckowski (Ed.), *Interfacial Electrochemistry: Theory, Experiment, and Applications,* Marcel Dekker, Inc., New York, **1999,** p. 707.

132. Zhang, H.; Banfield, J. F., *Am. Minerol.* **1999,** *84,* 528.

133. Ohno, T.; Haga, D.; Fujihara, K.; Kaizaki, K.; Matsumura, M., *J. Phys. Chem. B.* **1997**, *101*, 6415.

134. Fujihara, K.; Ohno, T.; Matsumura, M., *J. Chem. Soc., Faraday Trans.* **1998,** *94,* 3705.

135. Ulmann, M.; de Tacconi, N. R.; Augustynski, J., *J. Phys. Chem.* **1986**, *90*, 6523.

136. Augustynski, J., *Electrochim. Acta* **1993**, *38*, 43.

137. Yamamoto, J.; Tan, A.; Shiratsuchi, R.; Hayase, S.; Chenthamarakshan, C. R.; Rajeshwar, K., *Adv. Mater.* **2003**, *15*, 1823.

138. Chenthamarakshan, C. R.; de Tacconi N. R.; Rajeshwar, K.; Shiratsuchi, R., *Electrochem. Commun.* **2002**, *4,* 871.

139. Kiwi, J.; Grätzel, M., *J. Am. Chem. Soc.* **1979**, *101:24*, 7214.

140. Selzer, Y.; Turyan, I.; Mandler, D., *J. Phys. Chem. B,* **1999**, *103*, 1509.

BIOGRAPHICAL INFORMATION

The author received her Doctor of Philosophy in Chemistry from The University of Texas at Arlington in August 2006. She earned her Master of Philosophy in Chemical Sciences from Postgraduate Institute of Science, University of Peradeniya, SriLanka in 2001, and her Bachelor of Science (Special Degree in Chemistry) from University of Jaffna, SriLanka in 1997.